SPATIALLY RESOLVED TEMPERATURE AND HEAT FLUX MEASUREMENTS FOR SLOW EVAPORATING DROPLETS HEATED BY A MICROFABRICATED HEATER ARRAY

A Dissertation

by

SOKWON PAIK

Submitted to the Office of Graduate Studies of
Texas A&M University
in partial fulfillment of the requirements for the degree of

DOCTOR OF PHILOSOPHY

May 2005

Major Subject: Mechanical Engineering

SPATIALLY RESOLVED TEMPERATURE AND HEAT FLUX MEASUREMENTS FOR SLOW EVAPORATING DROPLETS HEATED BY A MICROFABRICATED HEATER ARRAY

A Dissertation

by

SOKWON PAIK

Submitted to Texas A&M University
in partial fulfillment of the requirements
for the degree of

DOCTOR OF PHILOSOPHY

Approved as to style and content by:

Kenneth D. Kihm
(Chair of Committee)

Sai Lau
(Member)

James G. Boyd
(Member)

Ali Beskok
(Member)

Dennis O’Neal
(Head of Department)

May 2005

Major Subject: Mechanical Engineering

ABSTRACT

Spatially Resolved Temperature and Heat Flux Measurements for Slow Evaporating
Droplets Heated by a Microfabricated Heater Array.
(May 2005)

Sokwon Paik, B.S., Yonsei University, Korea;
M.S., Yonsei University, Korea
Chair of Advisory Committee: Dr. Kenneth D. Kihm

The evaporation phenomenon of a liquid droplet was investigated by using microfabricated heaters. All 32 microheaters were designed to have the same resistance. Gold microheaters worked both as temperature indicators and as heaters. The first experiment was performed under a constant voltage mode to investigate the temperature and heat flux variation of the heated surface by the evaporating droplet. The second experiment was performed under constant temperature mode to investigate the spatial and temporal heat flux variation of the constant temperature heater surface by the evaporating droplet heater. Droplet evaporation was recorded with a CCD camera. Experimental data showed temperature and heat flux variations inside and outside of the droplet with respect to time and radial position from the center of the droplet by tomographic deconvolution.

DEDICATION

To my parents

ACKNOWLEDGMENTS

I would first like to thank my advisor, Dr. Kenneth D. Kihm, who has been a mentor, advisor and counselor to me. He has shared his knowledge, experience, time and effort with me. I greatly appreciate all of his contributions to this document.

Special thanks also go to Dr. Sai Lau, Dr. James Boyd and Dr. Ali Beskok for their time and effort assisting me in the completion of this research. I also thank Dr. Shinpyo Lee for his effort and dedication to this research and for his role as a mentor.

Appreciation goes to all my friends in Dr. Kihm's laboratory for their friendship and assistance during the past years.

Special thanks to Dr. Sangwon Park for his time and his willingness to allow me to use his lab.

Special thanks go to Mr. Cheong Soo Seo. He advised me and supported me whenever I experienced any trouble. He is like an unofficial committee member to me. I owe many things to him. I really appreciate his support and help.

Special thanks go to my parents, Tongki Paik and Minja Kim. They supported me both mentally and physically and were always there for me. Without their love and support, I couldn't finish my research. I owe everything to them.

Most of all, my deepest appreciation goes to my wife, Yougyung Na. She is my best friend, mentor, advisor, counselor and everything to me. She inspired me and encouraged me whenever I felt exhausted.

TABLE OF CONTENTS

Page

CHAPTER Page

LIST OF FIGURES

FIGURE Page

FIGURE Page

FIGURE Page

FIGURE Page

FIGURE Page

LIST OF TABLES

TABLE Page

NOMENCLATURE

t	time [sec]
V	volume [mm^3]
h	droplet height [mm]
r_o	droplet radius [mm]
r	distance from the center of droplet [mm]
ρ_T	Resistivity of gold at temperature T
ρ_0	Resistivity of gold at temperature 20°C
T	temperature [°C]
R	resistance [ohm]
R_o	heater resistance at 20°C
d	heater thickness [mm]
w	heater width [µm]
L	heater length [µm]
A	heater tomographic sectional area

Greek symbols

α	Temperature-resistance coefficient
τ	evaporation time
θ	droplet contact angle

Subscripts

k	order of heater (k = 1,2, ···, 32)
i	order of tomographically deconvoluted area (i = 1,2, ···,16)
W	wiring line
H	microheater line

CHAPTER I

INTRODUCTION

1.1 General background

1.1.1 Background of microheater fabrication

Microfabrication techniques began with the emergence of the micro-integrated circuit(IC). In the early years, lithography for microfabrication was based on thin and thick film processes [1]. Even though microfabrication emerged from IC techniques, microelectromechanical systems (MEMS) are not solely for electrical engineers. Currently MEMS devices are widely used in electrical engineering, bioengineering, medical science and mechanical engineering.

Microfluidics was born with the development of MEMS in the mechanical engineering area. Without microfluidics, we could not use the inkjet printer which we use every day in our homes and offices. There are thousands of micronozzles at the print head of an inkjet printer. To enhance the performance and quality of the inkjet printer, research papers related to the inkjet print head, such as the one written by Lee et al. [2], have been published. Currently, this inkjet printing technique is widely used for bioengineering purposes [3].

The journal model is ASME Journal of Heat Transfer.

The evaporation phenomenon is widely seen in technologies such as the inkjet printer and fire extinction [4]. Also, every time you cook, or even when you breathe or when you sweat, evaporation takes place. But, this very common and familiar phenomenon is not well known.

1.1.2 Background of constant voltage experiment configuration

Droplet evaporation on a heated surface has a variety of important applications in diverse areas of engineering including electronics cooling and thermal management for high heat flux equipment used by the nuclear and electronic industries [5, 6]. Selected metallurgical industries such as the aerospace industry and LNG shipbuilding are highly interested in the droplet evaporation phenomena associated with aluminum welding deficiencies [7]. When sophisticated aluminum welding is performed, quality problems occur such as surface cracking and nonuniform mechanical properties due to the quenching of aluminum parts. Quenching involves exposing the high temperature part of a surface to a liquid quenchant such as condensed water droplets, resulting in a relatively large and rapid fall in the local temperature. Another closely related application of droplet evaporation is in printer technology [8] where the quality of inkjet printing crucially relies upon the rapid and uniform evaporation of ink droplets. While a number of studies have been performed to examine bubble evaporation characteristics, almost all of the previous studies have concentrated on macroscopic measurements.

Xiong and Yuen [9] used thermocouple probes to measure the hot plate bulk temperature and overall heat flux variations during droplet evaporation. They varied the hot plate temperature from the film evaporation at relatively low temperatures against the spheroidal vaporization for different test fluids including water and various hydrocarbon liquid fuels. They presented averaged data for the overall heat flux and bulk temperature.

Bernardin et al. [7] investigated the temperature dependence of the advancing contact angle for a water droplet on an aluminum polished heating surface using a single thermocouple probe embedded below the heated surface. This experiment presented the temperature information of the heated aluminum surface at a single spatial point that is approximately at the center of the droplet. Again, the study lacked spatially resolved thermal data necessary to properly characterize droplet evaporation accompanying microscale heat and mass transport.

Makino and Michiyoshi [10] examined the influence of water droplet evaporation on a heated metal surface by measuring the voltage variations of an electric probe. They used four types of materials and water droplets ranging from 2.54mm to 4.50mm in diameter. This paper provided some quantitative data to correlate voltage variations with droplet evaporation, but did not present meaningful temperature variation data or heat flux variation data associated with droplet evaporation.

Crafton and Black [11] measured the heat transfer and evaporation rates of both heptane and water droplets on heated metal surfaces. They showed the heat flux data of their experiments by assuming constant droplet evaporation, and with this evaporation rate they calculated heat flux. They assumed a constant temperature inside of the droplet and calculated only one heat flux datum per one droplet. No spatial or temporal heat flux information was given.

Klassen et al. [12] and di Marzo et al. [13] were the first to use an infrared thermography technique to attempt to measure the spatially and temporally resolved temperature distributions for a single evaporating droplet. The major drawback of the study, however, is that since infrared is excessively absorbed by water, no reliable data could be obtained for the surface area covered by the droplet. Useful temperature measurements were available only in the neighboring heated surface area outside the droplet contact surface.

Dawson and di Marzo [14] later studied evaporative cooling of multiple water droplets of 10μl ± 1μl injected onto a 180°C heated Macor tile using infrared thermography. Because of the aforementioned limitation of the IR thermography, measurements were only possible outside of the droplets.

Michiyoshi and Makino [15] used a dual beam synchroscope to measure the variation of the heater supply voltage during the evaporation of a single water droplet on various heated plates such as copper, brass, carbon steel and stainless steel. Based on their experimental observations, only qualitative temperature profiles were presented for the heater surface contacting the droplet. The results identify a sharp drop in temperature upon droplet contact and show a constant temperature drop for almost all of the remaining evaporation period until dry-off occured [16].

Using a control volume method, Chandra et al. [4] calculated the temperature history both inside and outside the droplet during droplet evaporation and then attempted to validate their predictions with the experimental data of Klassen and di Marzo [12]. However, the later publication by di Marzo et al. [13] manifested that their published data in Klassen and di Marzo [12] was unreliable as the limitation of the IR technique was overlooked.

To elucidate the mechanism of droplet evaporation with appropriately resolved measurement data, which is lacking in the previously published studies, we have fabricated a microscale heater array and achieved spatially and temporally resolved thermal data for evaporating droplets. Each heater works as a heater, as well as a temperature sensor, based upon the resistance-temperature relationship of a thin gold deposited heater layer. Direct measurements of the heater resistance variations associated with the temperature drop by the evaporating droplet allows determination of the instantaneous heat flux and surface temperature for each heater with microscale spatial resolution. The microfabricated heater array technique also alleviates the intrinsic problem of the IR detection technique associated with its absorption in water [13].

1.1.3 Background of constant temperature experiment configuration

Control is widely used in industry and real life. For example, car driving is a control because one who drives a car needs to control the car to the aimed destination. PI and PID control are common control methods in industry. Without control, we could not run our car, the factory, the railroad system, etc. Control could be performed from readily defined values, but in many cases the control system receives a signal from the environment and then controls any value the system needs to have. As an example, there are room temperature controllers for every house. If the room temperature increases beyond a set temperature, the air conditioner will then cool down the room temperature. If the room temperature decreases beyond a set temperature, the heater will heat up the room temperature.

For satellites, the attitude and orbit must be controlled frequently. Without these controls, satellites could escape from their designated orbits and could collide with other satellites. For communication satellites, if we could not control its attitude position, then we could not receive signals from the satellite, and a multi-million dollar satellite would turn into trash. A satellite's life depends upon the amount of fuel available to control its orbit or attitude. These satellite controls utilize feedback control. As shown in the above examples, feedback controls are widely used in industry and real life. Feedback control is defined as the process of measuring the control variable and then using the information to influence the value of the controlled variable [17].

There are some previous experiments that used feedback control circuits to control the temperature or voltage of a microheater. Rule and Kim [18] controlled all 96 heaters individually to have the same temperature for their pool boiling experiment using liquid FC-72. They measured the temporal heat flux variation of one heater and the spatial heat flux distribution by dividing the heaters into five groups according to their distance from the center of the heater array. Their spatial heat flux distributions don’t have any meaningful temporal information, and they showed heat flux distribution with the variation of heater temperature only. Chen and Chung [19] used Wheatstone bridge circuits to keep the temperature of a heater array constant. They used 96 individually controlled feedback circuits, but among them, only one heater was turned on while the others were off. Their heater unit was the same one used by Rule and Kim [18]. They measured the temporal heat flux of each boiling droplet, but they measured only one heat flux per each droplet. Thus, they did not provide any spatial heat flux variation for each droplet.

If a droplet boils on the heater surface, only some part of the heater remains wet and the other part becomes dry because of the bubbling. Thus, the Chen and Chung [19] experiment is different from our evaporation experiment. Kimura and Toshima [20] used temperature control circuits of a micro-air-bridge heater which uses the pn junction temperature sensor designed for the absolute humidity sensor. The temperature of the micro-air-bridge was measured via the pn junction diode temperature at reverse and forward bias-voltage. Chen et al. [21] used electronic circuits for temperature control. They showed the temporal heat flux variation from two separate heaters during boiling, but no spatial heat flux information was provided. They used only one heater for one droplet boiling experiment. Jung et al. [22] used a Wheatstone bridge to detect the resistance variation of the microline heater under a constant voltage heating condition. The magnitude of the DC voltage applied to the bridge was controlled manually and no feedback control was used.

Lee, Kim and Kiger [23] used 96 feedback controlled microheater arrays to observe single droplet cooling. They used heater temperatures of 65°C, 75°C, and 85°C, and they used a low boiling temperature liquid, PF-5060, with a saturation temperature of 56°C. They showed some temporal heat flow rate information, but they only have one temporal heat flow rate per one experiment.

Lee, Kiger and Kim [24] used 96 feedback controlled microheater arrays to observe heat transfer by droplet cooling. PF-5060 was used for liquid droplet. The droplet drifted on the heater surface as it dried out, so, even though they measured the heat flux information on all 96 microheaters, they could not resolve any tabularized or graphed spatial heat flux information. As a result, they could get only total heat flux by the droplet evaporation with their 96 microheater.

To overcome the afore mentioned problems, 32 microheater arrays were fabricated for our droplet evaporation experiment. Experiments were performed under constant temperature boundary conditions. Voltage signals were acquired from the feedback circuit and then converted into heat flux data at each specific droplet location and at each specific time for each heater. These data can be used to elucidate the mechanism of droplet evaporation.

CHAPTER II

DESIGN AND FABRICATION OF MICROHEATER ARRAY

2.1 Heater design

A microheater was designed and fabricated to investigate the physical characteristics of droplet evaporation. The microheater array design (Fig. 2.1 to Fig. 2.4) consists of three layers: (1) the heater line layer (Fig. 2.1), the connection wiring layer (Fig. 2.2), and the opening layer for the power line soldering (Fig. 2.3). Each of the identical 32 line heaters is 100μm wide with 100μm spacing, 0.5μm thick for the constant voltage experiment or 0.25μm thick for the constant temperature experiment, and 1.5cm long. Thus, the whole heater array occupies a rectangular heating area of $0.945\, cm^2$ (0.63cm x 1.5cm). Care was taken to ensure an identical resistance for all individual wiring layer lines connecting the heater line elements to the corresponding soldering electrodes by varying the wiring widths to compensate for their different lengths. The resistance ratio between the heater line and the wiring layer line is 7.5:1 for the constant voltage experiment and 10:1 for the constant temperature experiment. The wiring layer line is 2.884863 times larger than heater line. Based on this, heat flux between heater and wiring line is 21.636:1. Since power is proportional to resistance (Power = VI = I^2R and heater and wiring line have the same current so, power is proportional to resistance) and heat flux means power per unit area, if the heater is heated to 60°C then the wiring line is heated only 3°C ($\frac{1}{7.5} * \frac{1}{2.884863} * 60 \approx 3$). This wiring line temperature transition changes the resistance of the wiring line by the temperature resistance relation equation (2.1).

$$R_T = R_o(1 + \alpha(T - T_o)) \tag{2.1}$$

If one defines the heater resistance at 20°C as R_{oH}, the wiring line resistance at 20°C as R_{oW} , the heater resistance at 80°C(heated 60°C) as R_{TH}, and the wiring line resistance at 23°C(heated 3°C) as R_{TW} then the resistance change between the heater and the heated wiring line is

$$\frac{R_{TW} - R_{W0}}{R_{TH} - R_{0H}} \approx \frac{R_{W0}\alpha(3)}{R_{0H}\alpha(60)} = \frac{3}{7.5 * 60} = \frac{3}{7.5 * 60} = \frac{1}{150}$$

Thus, the wiring line resistance changes by 0.6% of heater line resistance change. This percentage means heater temperature variation could have a 0.6% error. So, for the case of a 80°C heater temperature (heated 60°C), the heater temperature error by ignoring due to the wiring resistance variation is about 0.4°C (60*0.6%) and for a 40°C heater temperature (heated 20°C), the heater temperature error is only about 0.1°C. Since this amount of error is less than the temperature-resistance relation linearization error, it is ignored in this experiment. The above calculations are for the constant voltage heater experiment. For the constant temperature experiment, the wiring line resistance variation was also ignored.

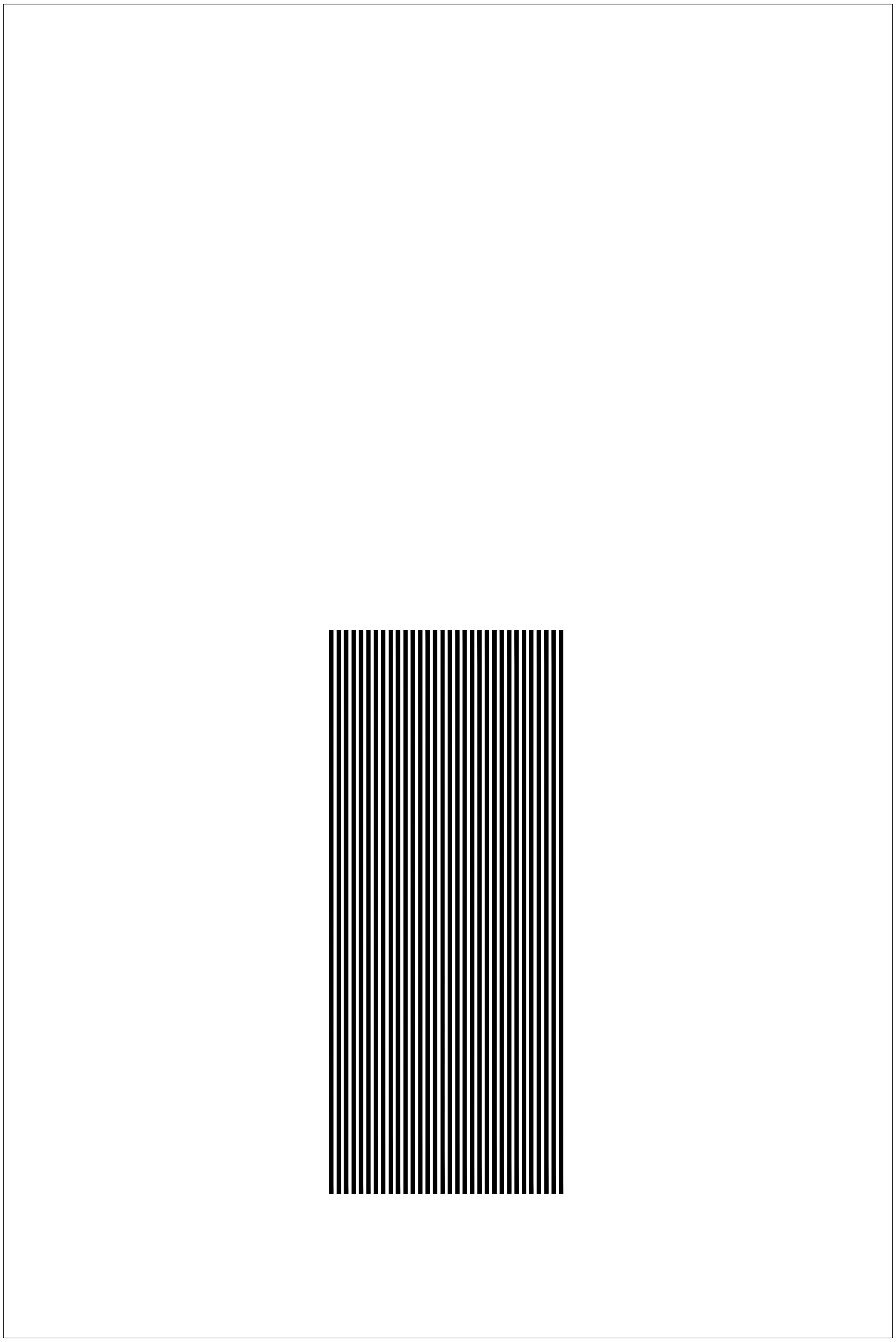

Fig. 2.1 Heater layer design

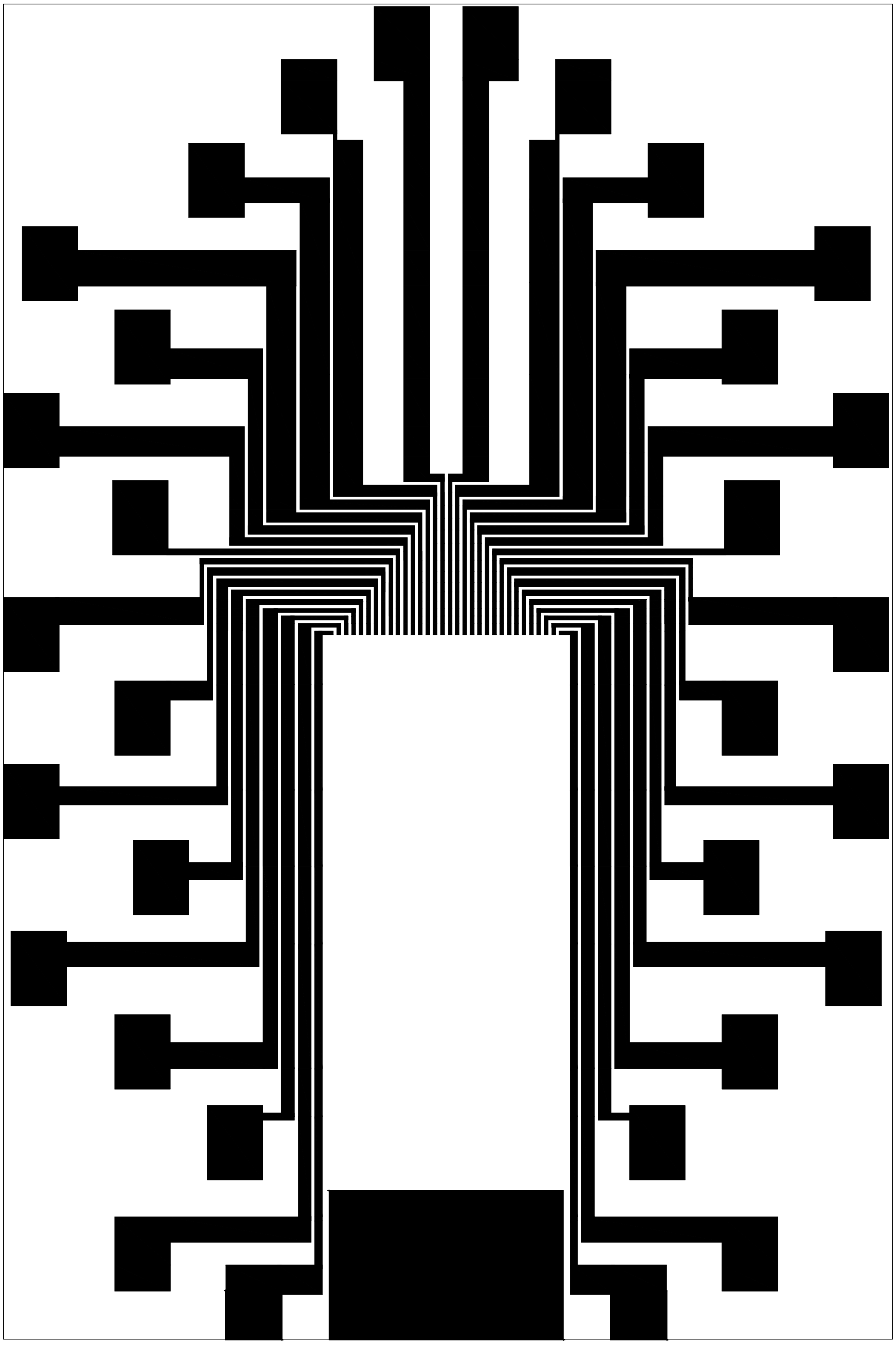

Fig. 2.2 Connection wiring layer design

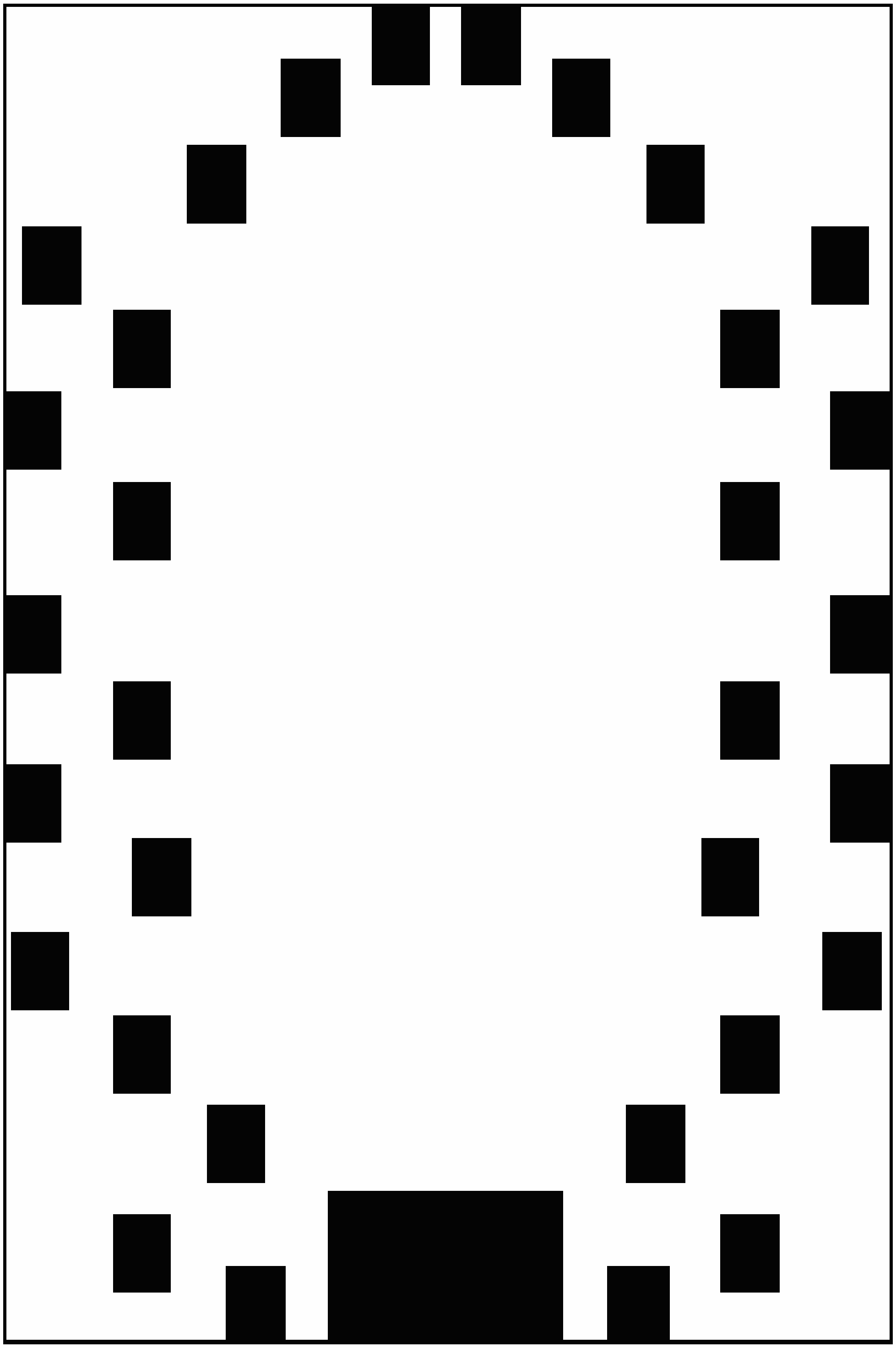

Fig. 2.3 Opening layer design

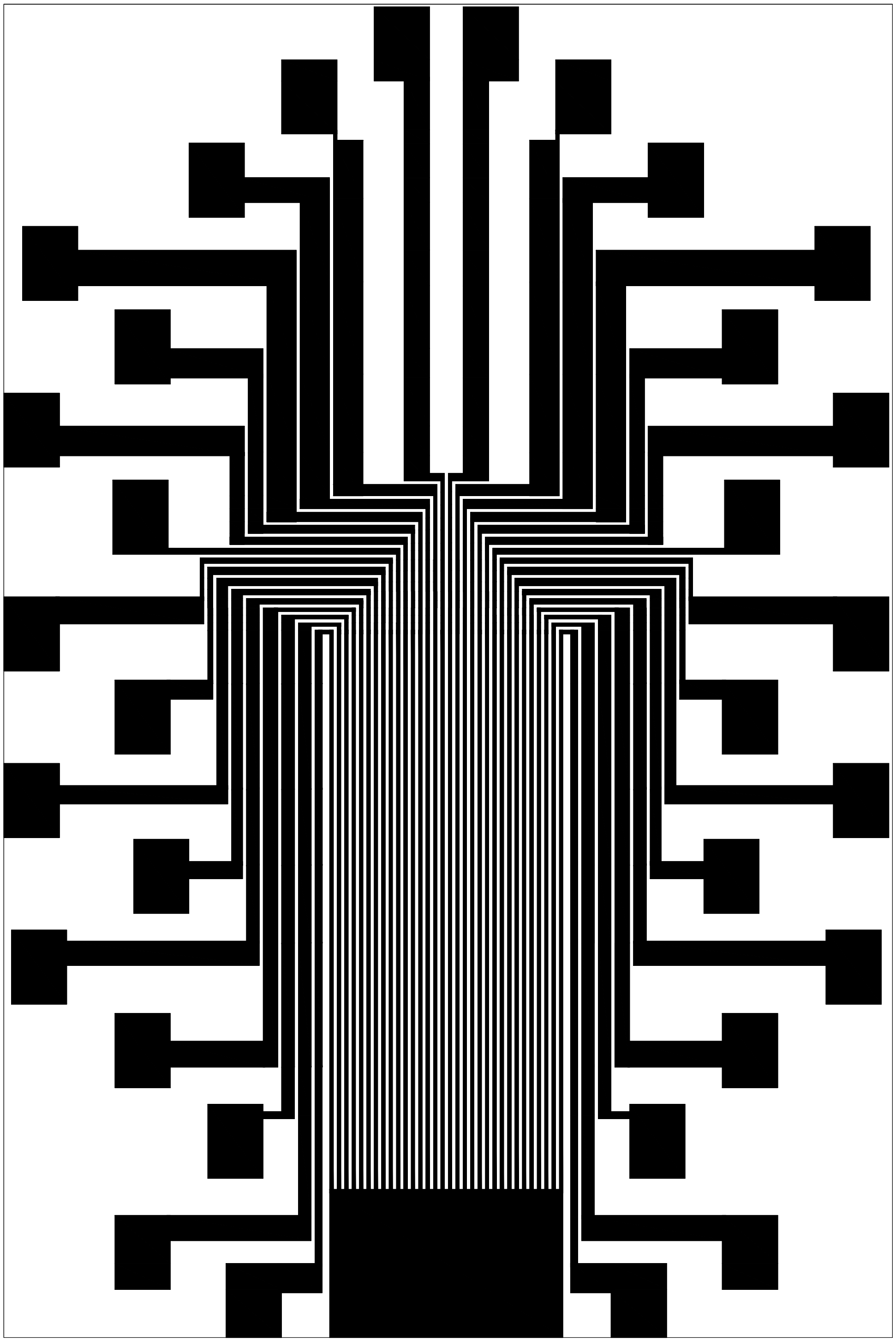

Fig. 2.4 Overview of whole heater design

2.2 Fabrication procedure

The microheater array was fabricated in a class 1000 clean room located at Texas A&M University except for the seed layer coating process. The whole microheater fabrication process can be divided into a (a) seed layer fabrication process (Figure on p.19) (b) heater layer fabrication process (Figure on p.26) (c) wiring layer fabrication process (Figure on p.33) (d) seed layer removal fabrication process (Figure on p.36), and (e) opening layer fabrication process (Figure on p.36). Detailed fabrication procedures are described in the following chapters. The constant temperature experiment heater fabrication procedures and the constant voltage experiment heater fabrication procedures are the same. Thus, only constant voltage experiment heater fabrication procedures are shown.

2.2.1 Sputtering seed layer coating procedure

A sputter coater was used to attach the gold seed layer on a glass substrate. Since gold cannot be directly attached to the soda-lime glass substrate, a 10-nm thick chromium bonding layer was coated to the substrate (Fig. 2.5a). Then the 50-nm thick gold seed layer was coated on the chromium layer (Fig. 2.5b).

These procedures were performed at the University of Texas at Dallas clean room with the help of Dr. Sangwon Park. The sputtering process provides a strong and even coating on the glass, and it is easy to control the coating thickness. The sputtering procedure is as follows:

2.2.1.1 Chrome sputter seed layer coating

1. Push the “Standby” button and wait 10 sec.
2. Push the “Vent” button and go back to the “Service Chase #1”
3. Open the nitrogen gas, wait 1 min. and close
4. Push the “Standby” button, open chamber and load Samples
5. Close the chamber and push the “Start” button
6. Wait 40 min. until pressure is lowered 10^{-6} Torr
7. To check the pressure, turn on the “Ion Gage” and turn off the “Ion Gage”
8. To check the gas flow condition, push the “Control Mode” and choose “Auto”
9. Turn on the Ar main switch and turn on “MFC Channel #1”
10. Make sure the chamber pressure is 25.00 mTorr
11. Check the water flow for the magnetic sputter power supply
12. Turn on the gun power and choose the target material as chrome
13. Change the key to “Program” (press “OFF” button to stop beep)
14. Set the sputtering time at 1 min; press the “Ramp” and hold then SET.PT then modify
15. Set the sputtering power at 500W; press the “Level” and hold then SET.PT then modify
16. To observe the process time, push “Actual” button to see minutes
17. Push “Output” on
18. Open the “Shutter” when heard the beeping
19. Once beeping signals the completion of sputtering, close the shutter and push

"Output" off

2.2.1.2 Gold sputter seed layer coating

1. Wait 5 min after the chrome sputter process for proper annealing
2. Turn on the gun power and choose the target material as gold
3. Change the key to "Program" (press "OFF" button to stop beep)
4. Set the sputtering time at 2 min 30sec; press the "Ramp" and hold then SET.PT then modify
5. Set the sputtering power at 300W; press the "Level" and hold then SET.PT then modify
6. To observe the process time, push "Actual" Button to see minutes
7. Push "Output" on
8. Open the "Shutter" when heard the beeping
9. Once beeping signals the completion of sputtering, close the shutter and push "Output" off
10. Wait 20 min after all layers processing
11. Change the key to "OFF" mode and turn off the gun power
12. Turn off the "MFC channel # 1" and turn off the Ar main switch
13. Change the setting to "OPEN UNDERRANGE" with the arrow key (enter)
14. Push the "Standby" button and wait 10 sec.
15. Push the "Vent" button and go back to the "Service Chase #1"
16. Open the nitrogen gas and Wait 1 min. and close

17. Push the “Standby” button, open chamber, and remove samples
18. Close the chamber and push the “Start” button

These procedures follow The University of Texas at Dallas Clean Room Sputter Machine Manual.

Before the seed layer fabrication procedure, all glass substrate should be cleaned by using pure isopropyl alcohol and acetone. It is recommended that you use acetone first and then use the isopropyl alcohol. After the acetone and isopropyl alcohol cleaning process, the glass substrate should be thoroughly rinsed with deionized water.

We can use a Piranha solution for the cleaning, but using this solution requires a long time to prepare and, moreover, is hard to control. With isopropyl alcohol and acetone, almost all of the impure substances on the substrate glass can be removed thoroughly. If this cleaning job is not thorough, the seed layer coating quality is degraded and this degradation will cause degradation or failure of microheater quality.

If we use deionized water to rinse the substrate, moisture remains on the substrate. So, we need to dry out this moisture before the seed layer coating. The dry out process was performed for 30 minutes in a 95°C oven.

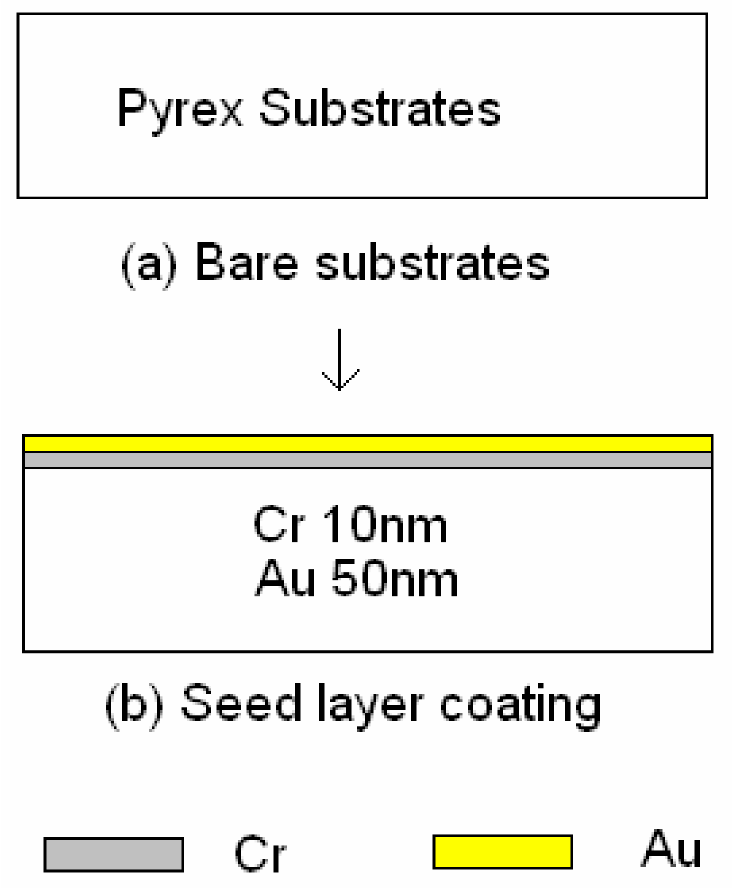

Fig. 2.5 Seed layer fabrication

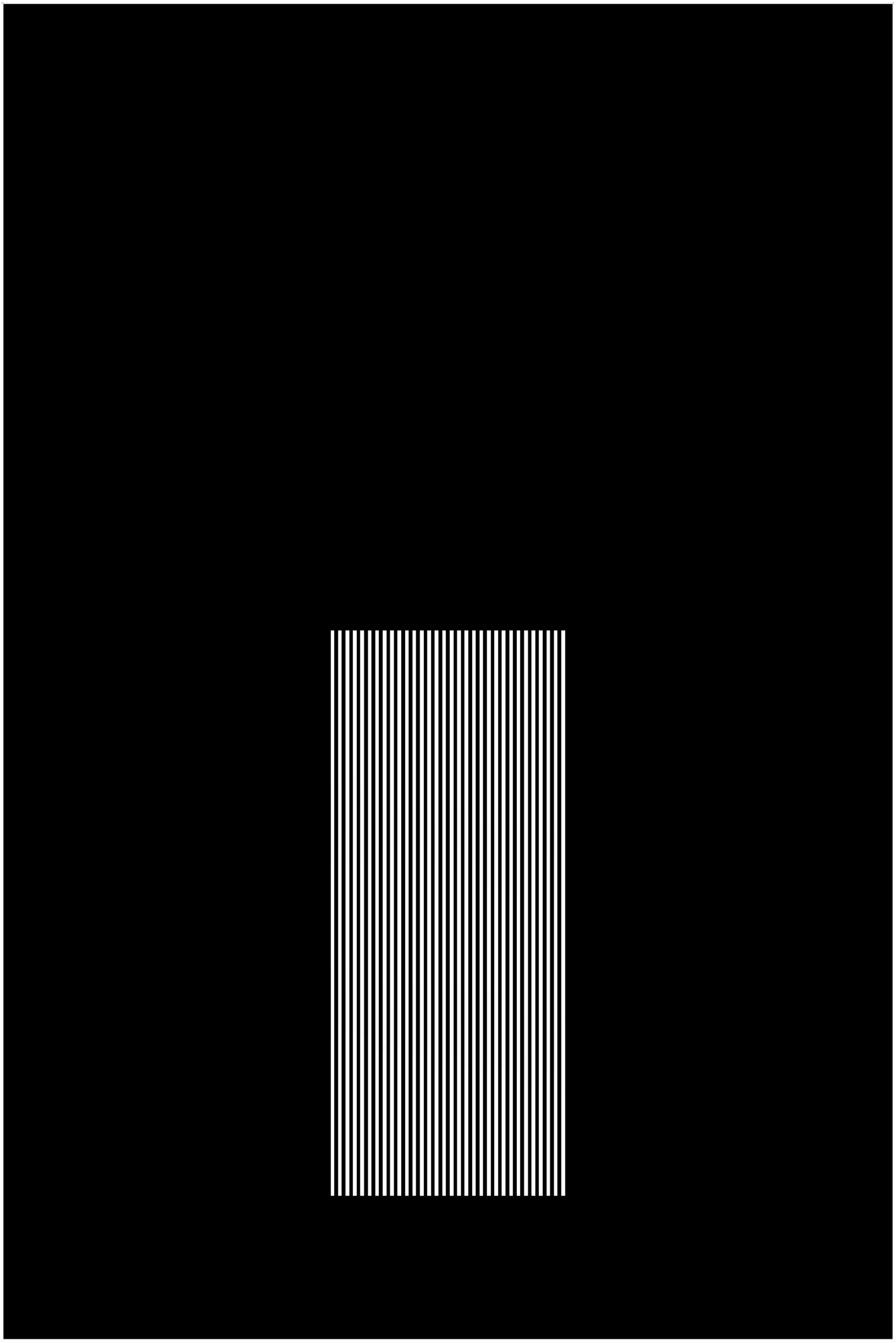

Fig. 2.6 Heater layer mask

2.2.2 Heater layer fabrication procedure

The heater layer is the layer for the microheater. This heater layer uses the design of Fig. 2.1. Instead of Fig. 2.1, Fig. 2.6 was used as the photo mask for fabrication of the heater layer. This mask design is for a positive photo resist. Thus, only the parts exposed to light dissolve in the developer. Fig. 2.1 could be used as a negative photo resist. This picture is only shown because the position of the heater lines is easier to see.

Glass masks are widely used for the photo mask. They are dependable and good for the design of devices with a few microline structures. As our design does not require very fine line quality, a film mask was used instead of a conventional glass mask for several reasons. For one, the turn-around time from ordering to receiving a glass mask is several weeks. Any design change would thus cause several weeks of down time. In addition, glass masks are exceptionally fragile as opposed to flexible film masks. Finally, glass masks are prohibitively expensive, requiring $3000 per heater design ($1000 for each heater layer mask, wiring layer mask and opening layer mask).

The photo mask was made at the Health Science Center Communications Production Department at Texas A&M University. Their process restrictions required that the heater design fit within 35mm film which is exactly 24mm (H) X 36mm (W).

With film mask, the first effort for a new microheater failed as shown in Fig. 2.7. With low resolution, microheater lines look good, but with high resolution pictures, it was found that microheater lines were plated sparsely and could not conduct the electricity. It was suspected this failure was due to dirty glass substrate before the seed layer coating, but it was found that the cause was dirty film mask. With a microscope, the film mask looked clean, as shown in Fig. 2.8. When using a magnified view to observe the film mask of the microheater, the white part should not have any dot or any contaminant in it to work. The white part looked contaminant free, so it was thought that this microheater was good, but this mask was used to obtain the lithography of Fig. 2.9(a) and Fig. 2.9(b), and then it was found that our photo resist pattern was not good.

Fig. 2.10(a) is the magnified pattern of the photo resist of the microheater after the UV exposure. The bright grey and whitish bar area is the area for the microheater. Gold will be electroplated on this area. As can be seen in the figure, the microheater area does not look clean. UV exposure time was varied to eliminate this phenomenon, but this did not solve the problem. The cure for this problem was RIE (Reactive Ion Etching). Fig. 2.10(b) is the picture of the photo resist pattern of Fig. 2.10(a) after 5 minutes of oxygen RIE under 100W. As can be seen, most of the remaining materials (Shipley 1818) cleared with the reaction of RIE. March Plasma Systems Reactive CS-1701 Ion Etcher was used for RIE. With 5 minutes of RIE, the remaining photo resist wasn’t thoroughly removed, so 3 more minutes of RIE was performed with the same power applied to the pattern of photo resist, which is on top of the glass substrates. So, with total 8 minutes of RIE, all remaining photo resist on the heater area was removed as can be seen Fig. 2.10(c).

Electroplating was used to deposit gold for the heater and wiring layer. Electroplating is easy to use, and provides strong coating and easy thickness control. The total deposition thickness h follows the equation below.

$$h = \frac{It}{AFz} \qquad (2.2)$$

where F: Faraday constant, (96,500 Coulombs)

z: valence of an ion

A: electro plating area

I: total current

t: deposition time

As can be seen in the above equation (2.2), the total amount of deposition is proportional to the total current and total deposition time.

Fig. 2.11 shows the electroplating diagram. In plating, platinum was used for the electrode. Technic Inc. Techni-Gold 25E Solution was used in the electroplating. An HP-6033A power supply was used in control current mode. As the thickness of gold plating depends only on the total deposition time and total current, the voltage input is meaningless in electroplating. It is the input current that controls the microheater thickness.

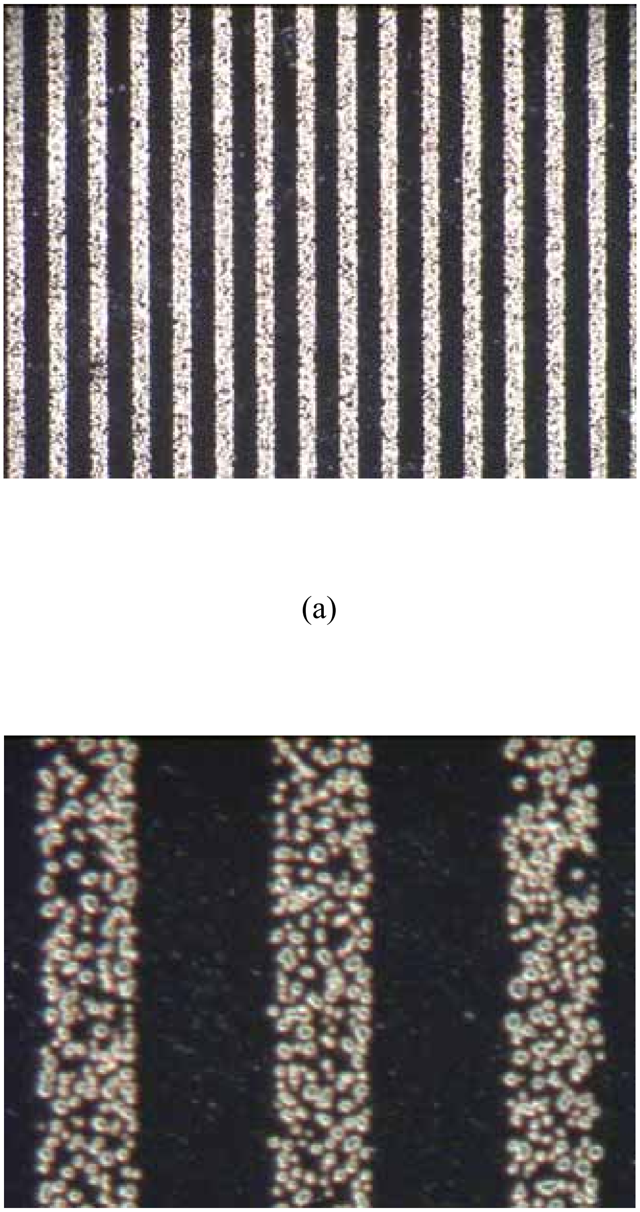

(a)

(b)

Fig. 2.7 Magnified view of failed to make microheater lines; (a) low magnification (100x) (b) High magnification (600x)

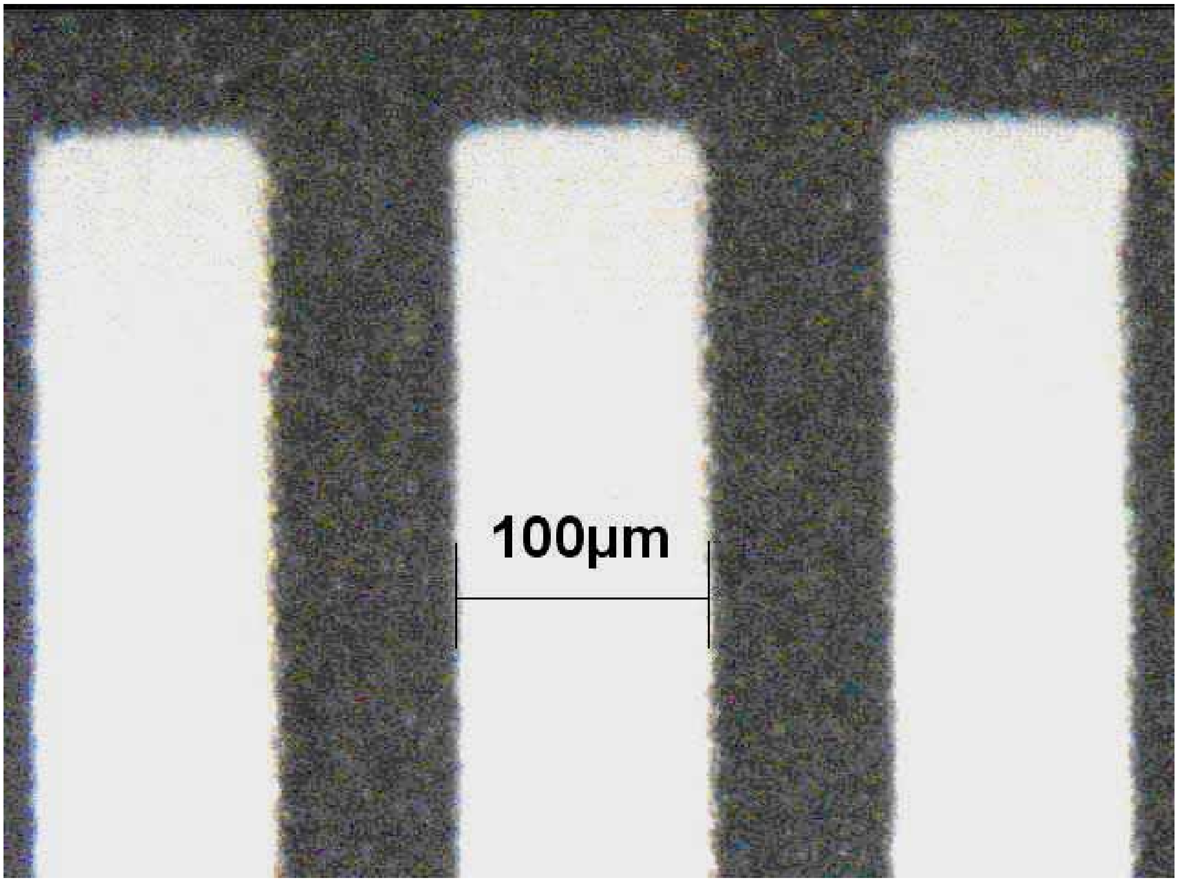

Fig. 2.8 Part of microheater layer mask

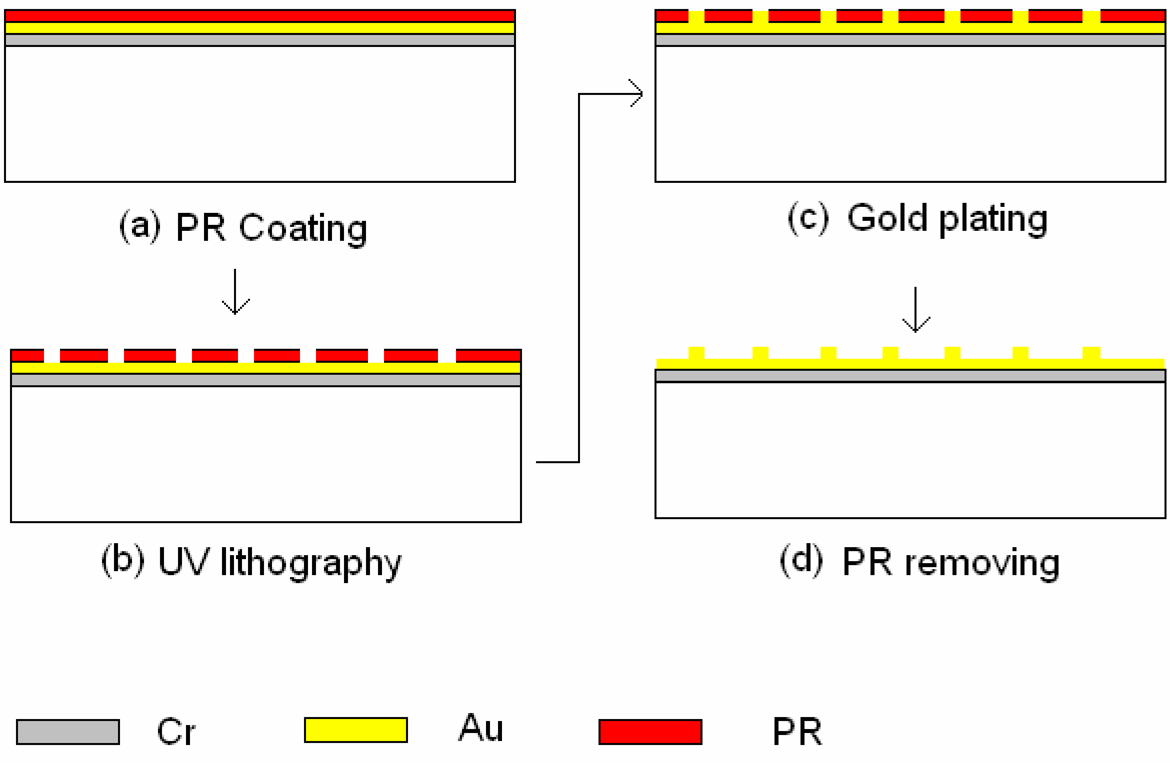

Fig. 2.9 Heater layer fabrication

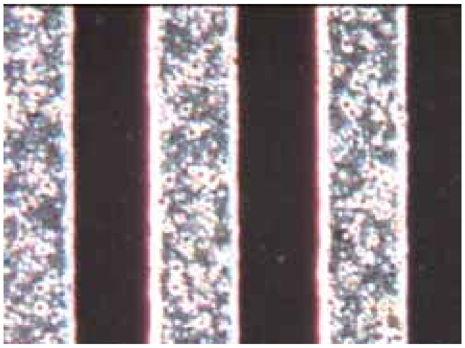

(a) Before RIE

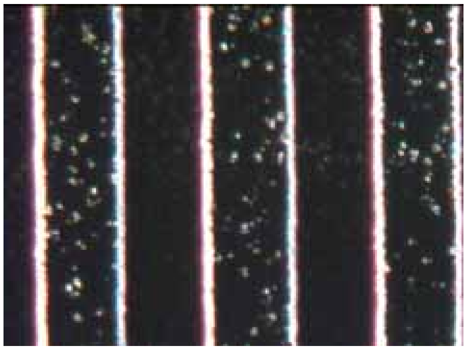

(b) RIE 5min

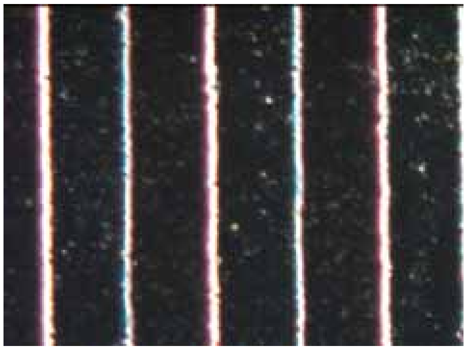

(c) RIE 8min

Fig. 2.10 Photo resist pattern of microheater layer after UV exposure

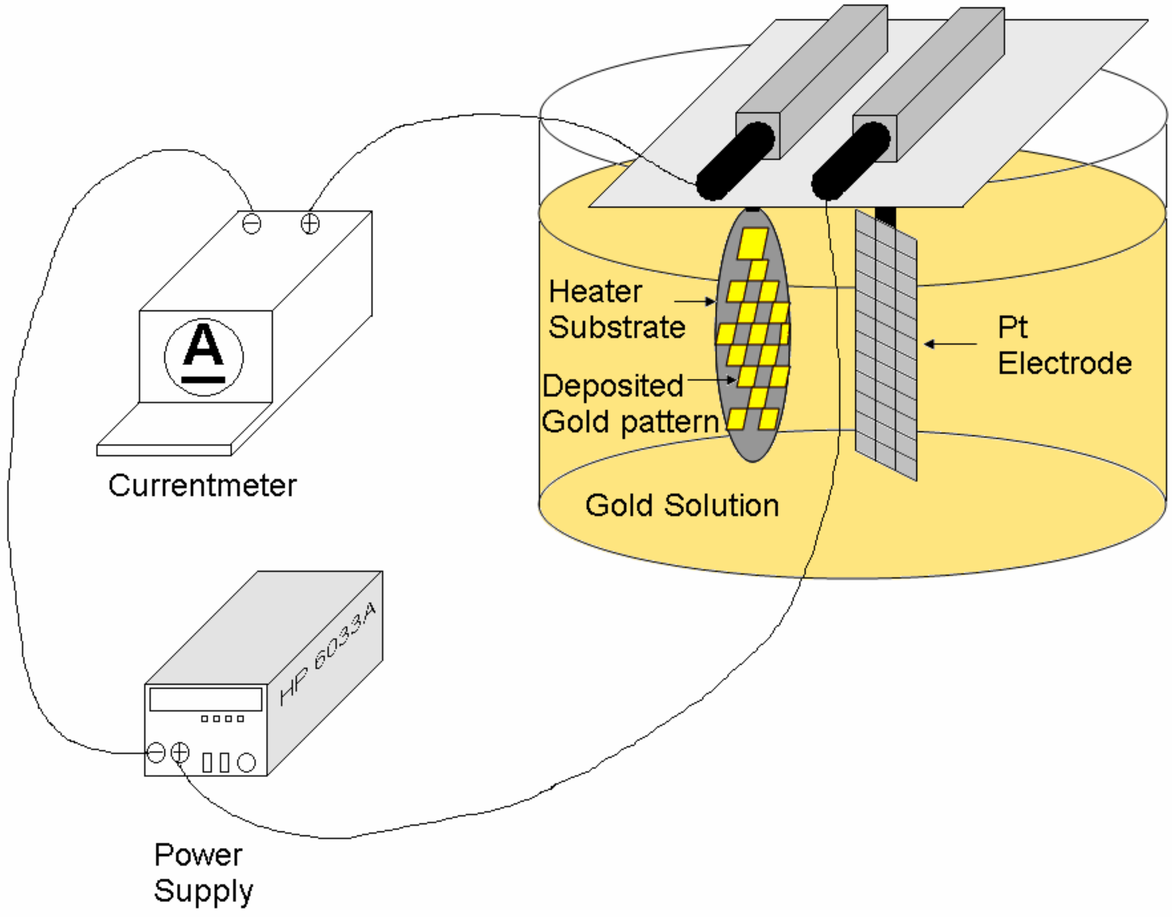

Fig. 2.11 Electroplating experiment setup

The following subsection details the microheater layer fabrication process.

2.2.2.1 Minute heater layer fabrication procedure

1. PR processing

    a. Wafer cleaning

    -Using the previously prepared seed layer wafer (Cr 100Å, Au 500Å)

    b. Oven temperature setting

    - 95°C

    c. Photoresist coating with S1818

    - 2000 rpm, 1 min

    - 2.3μm

    d. Soft baking

    - 95°C, 15min

    e. UV exposure

    - $18mW/cm^2$, 7 sec

    f. Developing

    - MF319, 2 min

    g. Hard baking

    - 95°C, 10min

    h. Plasma etching (RIE)

    - O_2 100-140 Torr 100W, 8 min

2. Electroplating

- a. Bath Preheating
    - 2 hours at 55°C
- b. Electroplating
    - 1mA, 18 min
    - 0.65 μm

2.2.3 Wiring layer fabrication procedure

On one end, the wiring layer connects each microheater to an individual electrode. One the other end, the wiring layer connects all of the microheater lines to a single common electrode. Fig. 2.2 is the design of the wiring layer, however, the photo mask for the wiring layer should be the inverse image of Fig. 2.2. The photo mask of the wiring layer is shown at Fig. 2.12. The fabrication procedures roughly follow the microheater layer fabrication procedures. They are shown in Fig. 2.13 as (a) PR coating (b) UV lithography (c) Gold plating and (d) PR removing. The following sub section explains the detailed fabrication procedures for the wiring layer.

2.2.3.1 Minute wiring layer fabrication procedures

1. PR processing
    - a. Photoresist coating with S1818
        - 2000 rpm, 1 min
        - 2.3µm
    - b. Soft baking
        - 95°C, 15min
    - c. UV exposure
        - $18mW/cm^2$, 7 sec
    - d. Developing
        - MF319, 2 min
    - e. Hard baking
        - 95°C, 10min
    - f. Plasma etching (RIE)
        - O_2 100-140 Torr 100W, 8 min

2. Electroplating
    - a. Electroplating
        - 2mA, 60 min
    - b. 1.65 µm

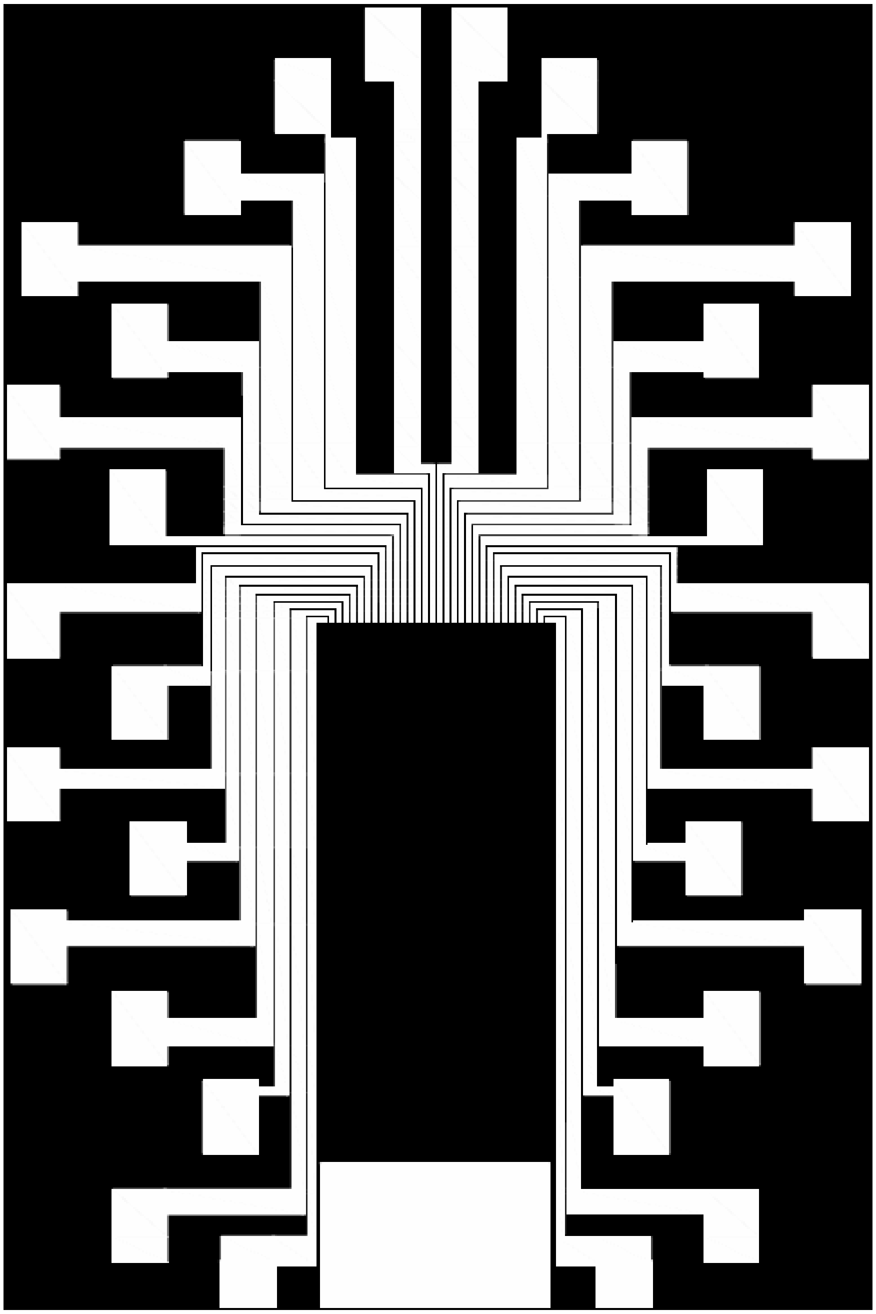

Fig. 2.12 Wiring layer mask

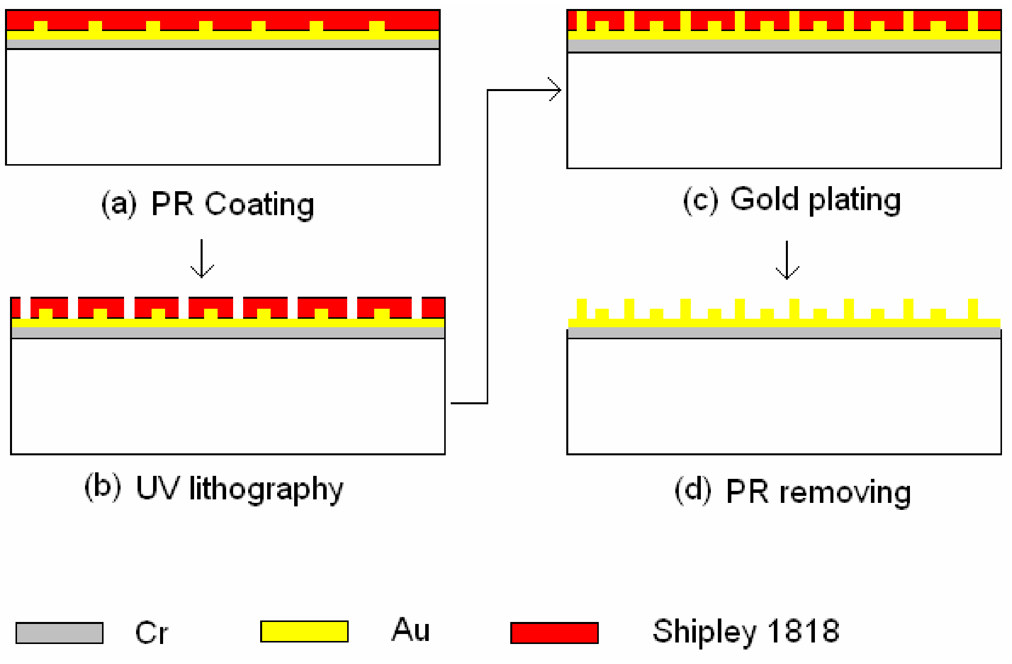

Fig. 2.13 Wiring layer fabrication procedure

2.2.4 Seed layer removal procedure

The wiring layer fabrication procedure connects all heater lines and wiring layer lines with the seed layer. The seed layer represents all of the heater substrate surface area (36mm x 24mm) and is coated with gold. So, to make the microheater and wiring line functional, the seed layer should be removed. Gold etchant was used to remove the gold seed layer, and chromium mask etchant was used to remove the chromium seed layer. These seed layer removal procedures are shown in Fig. 2.14 for the (a) gold seed layer removal and (b) chrome seed layer removal process. The chromium seed layer was deposited originally with pure chromium but, overtime, this chromium seed layer oxidizes into chromium oxide. Thus, the chromium seed layer could not be removed with chromium etchant. Even with chromium oxide etchant, the chromium seed layer was sometimes hard to remove. This is because the gold seed layer was not thoroughly removed first. Remaining gold seed layer blocked the chromium mask etchant from contact with the chromium seed layer. In the same way, if the substrate was not thoroughly cleaned, the gold seed layer was also difficult to remove. For the gold seed layer removal, one minute of oxygen RIE under 100W is recommended right before the gold seed layer removal process for more dependable seed layer removal. One minute of oxygen RIE under 100W is also recommended before chromium seed layer removal for more dependable removal. Detailed removal procedures are shown in the following chapter. As a result, a 1.5μm thick wiring layer and 0.5μm thick heater layer are finally realized.

2.2.4.1 Minute seed layer removal procedure

1. Au Etching
   a. Plasma etching (RIE)
      -O_2 100-140 Torr 100W, 1 min
   b. Au etching
      - 10 sec
   c. Visual inspection
   d. Wafer cleaning
   e. Wafer drying

2. Cr Etching
   a. Plasma etching (RIE)
      - O_2 100-140 Torr 100W, 1 min
   b. Cr etching
      - 6 sec
   c. Visual inspection
   d. Wafer cleaning
   e. Wafer drying

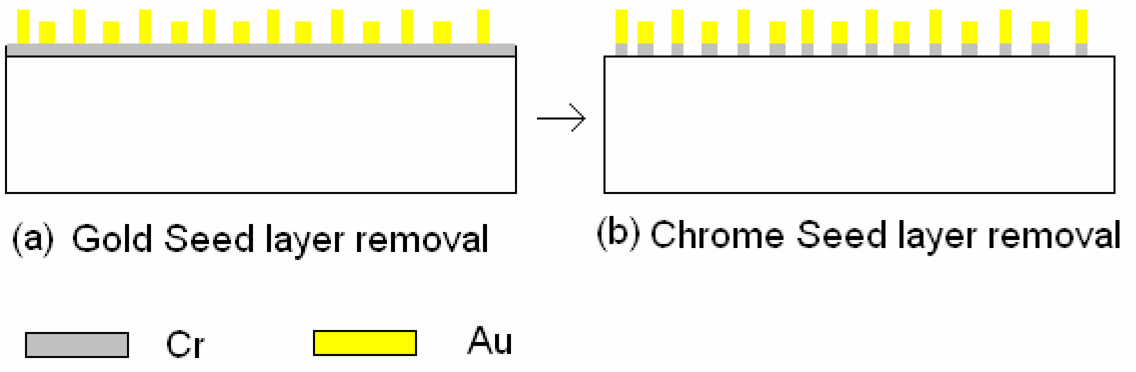

(a) Gold Seed layer removal

(b) Chrome Seed layer removal

Fig. 2.14 Seed layer removal fabrication procedure

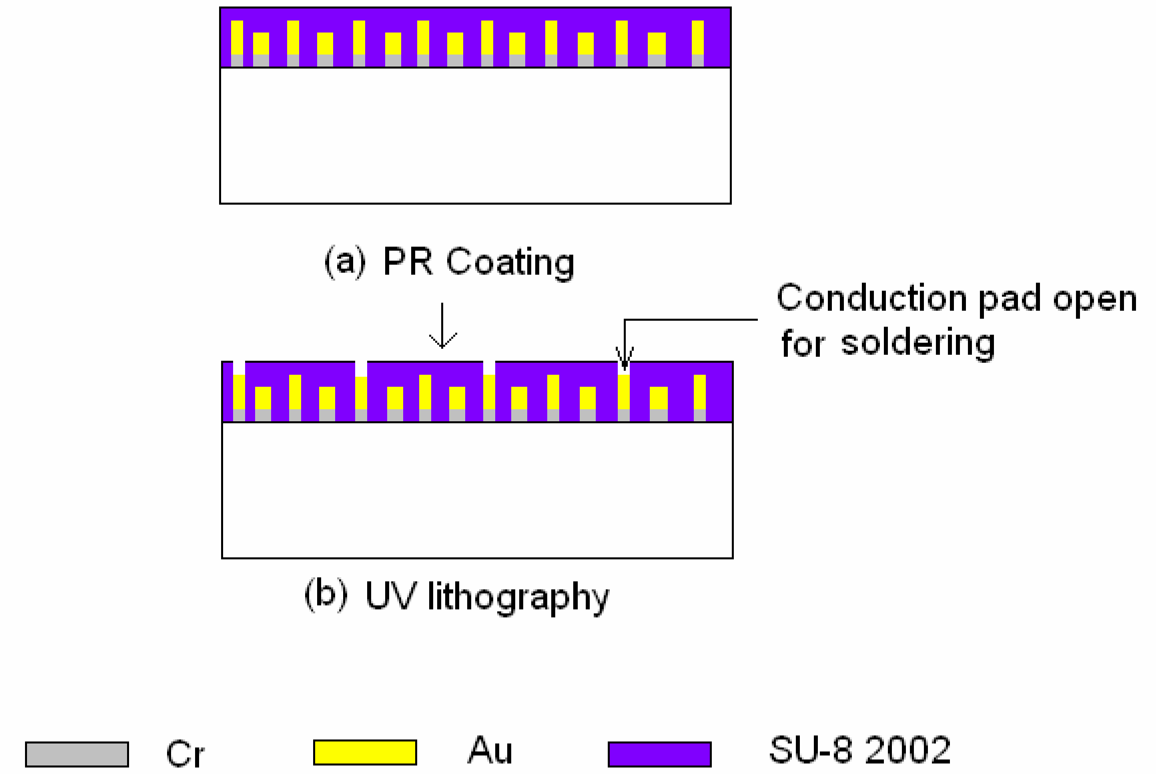

(a) PR Coating

(b) UV lithography

Fig. 2.15 Opening layer fabrication procedure

2.2.5 Opening layer fabrication procedure

The procedures from section 2.1.1 to section 2.1.4, the heater layer fabrication procedures to the procedures of seed layer removal, would be enough to complete the heater fabrication process as long as nothing touches the heater surface. But for this experiment, a water droplet touches the heater surface so the surface of the heater must be cleaned before every experiment. Thus, a protection layer is required for the heater. Without this coating, an electric short could occur between the microheater lines or between the wiring lines. The coating layer also protects the microheater and wiring layers. Without the coating, cleaning could damage the microheater and wiring lines. Thus, to protect the microheaters and wiring lines and to prevent an electric short, a coating layer is needed on top of the microheater lines and wiring lines. Fig. 2.3 shows the photo mask design of the opening layer, and Fig. 2.15 explains this opening layer fabrication procedure in terms of (a) PR coating and (b) UV lithography.

SU-8 is very stable and difficult to dissolve in many liquids. It is also an electrically non-conducting material, and the surface of SU-8 is strong if hard baked. SU-8 is used for the photo negatives, and the SU-8 2002 series is used for the protective coating.

RIE etching was performed at the final stage of the fabrication. There could have been some chemical remnants on the common electrode and individual electrode. With RIE, these remnants should be removed before soldering. As SU-8 is hard to remove with RIE, a higher power and longer RIE duration were required than in section 2.1.4.1

2.2.5.1 Minute process of opening layer fabrication

1. PR processing
    - a. Photoresist coating with SU-8 2002
        - 3000 rpm, 1 min
        - 2.5μm
    - b. Soft baking
        - 65°C, 1min
        - 95°C, 2min
    - c. UV exposure
        - $18mW/cm^2$, 8 sec
    - d. Developing
        - SU-8 developer, 2 min
    - e. Hard baking
        - 65°C, 1min
        - 95°C, 1min
    - f. Plasma etching
        - O_2 100-140 Torr 200W, 3 min

Now, with above fabrication process complete, the microheater is ready for use.

CHAPTER III

CONSTANT VOLTAGE DROPLET EVAPORATION EXPERIMENT

3.1 Heater dimension and temperature resistance relation

Under the constant current operation the heating power, i^2R, is linearly proportional to the resistance, and thus, the heat flux from the line heater is 21.70 times (0.133^{-1}*2.885) higher than that from the wiring line as stated previously in Chapter II.

For relatively narrow temperature ranges, such as the tested range from 273K to 400K, the temperature-resistance relation of gold is nearly perfectly linear as,

$$R = R_0(1 + \alpha(T - T_0))$$

where the resistance R varies linearly with the slope of temperature-resistance coefficient α. For a single linear resistor element, the resistance-temperature relation can be readily reduced to the resistivity-temperature relation by using the equation,

$$R = \rho \frac{L}{A} \qquad (3.1)$$

where ρ is the resistivity, L denotes the length of resistor, and A denotes its cross-sectional area. Resistivity temperature equation is,

$$\rho = \rho_0 (1 + \alpha (T - T_0)) \qquad (3.2\text{-a})$$

Equation (2.1) or Eq. (3.2-a) can also be expressed as

$$R = \rho_o \left[1 + \alpha \left(T - T_o\right)\right] \frac{L}{w \cdot d} \qquad (3.2\text{-b})$$

Table 3.1 Comparison between measured gold resistivity and the linearized data approximated by Eq. (2.1)

Temperature (K)	Measured gold resistivity [25, 26] (Ωm)	Calculated gold resistivity by the linearized equation, Eq. (2.1) (Ωm)	Percentile errors (%)
273	2.051×10^{-8}	2.051×10^{-8}	0.00
293	2.214×10^{-8}	2.214×10^{-8}	0.00
300	2.271×10^{-8}	2.272×10^{-8}	0.03
350	2.685×10^{-8}	2.683×10^{-8}	0.08
400	3.107×10^{-8}	3.094×10^{-8}	0.42

Comparison of the linearized data expressed by Eq. (2.1) with the actual measured resistivity data [25, 26] are shown in Table 3.1. For the present experiment for slow evaporation of water droplets, the maximum temperature condition will not exceed 80°C, and the linearized relation of Eq. (2.1) can be used with the linearization error of less than 0.1%.

3.2 Experimental setup

Fig. 3.1 presents a schematic illustration for the constant-voltage operation of the microheater array. A precision HP 6033A DC Power Supply powers the heater line array with a constant voltage specifying a constant dry temperature based on the linearized resistance-temperature relation of gold, Eq. (2.1). Input voltages of 2.09V, 3.00V, and 3.53V provide the tested dry heater line temperatures of 40°C, 60°C and 80°C, respectively. The individual data acquisition from the 32 line heaters is achieved with two NI PCI 6013 boards with two CB 68-LP shield connectors.

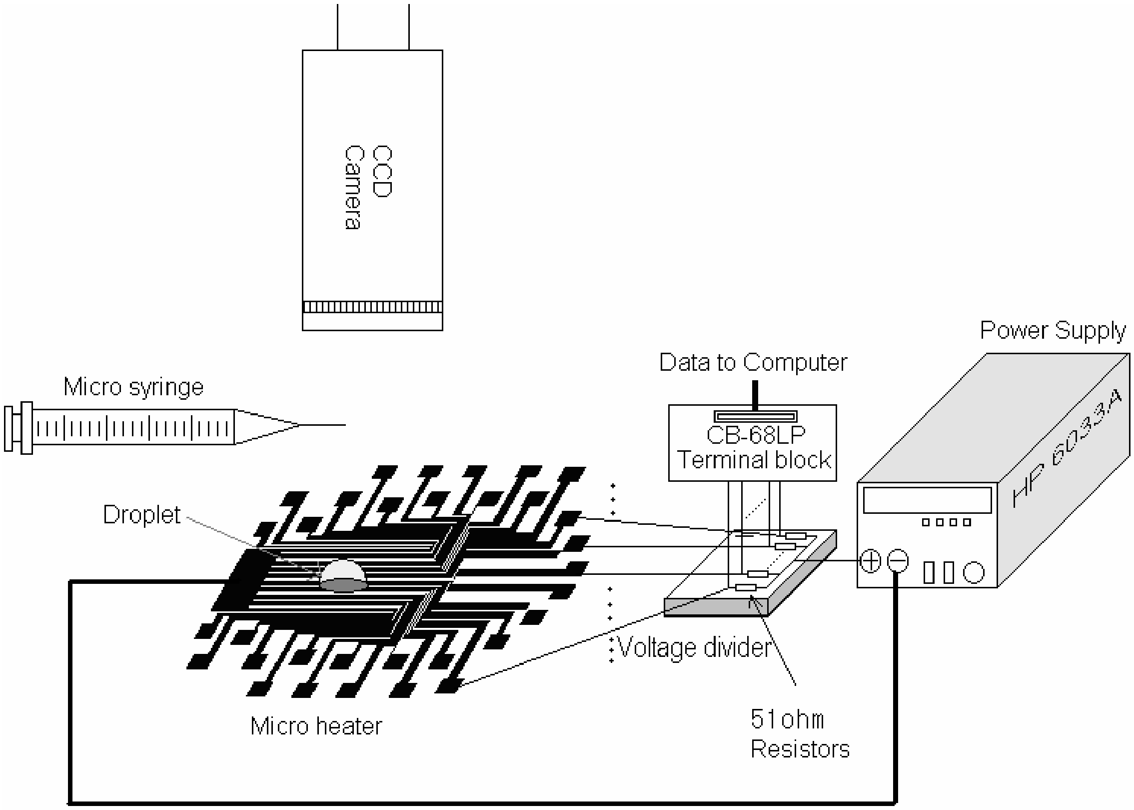

Fig. 3.1 Schematic illustration of the constant-voltage supply circuit for the microheater array

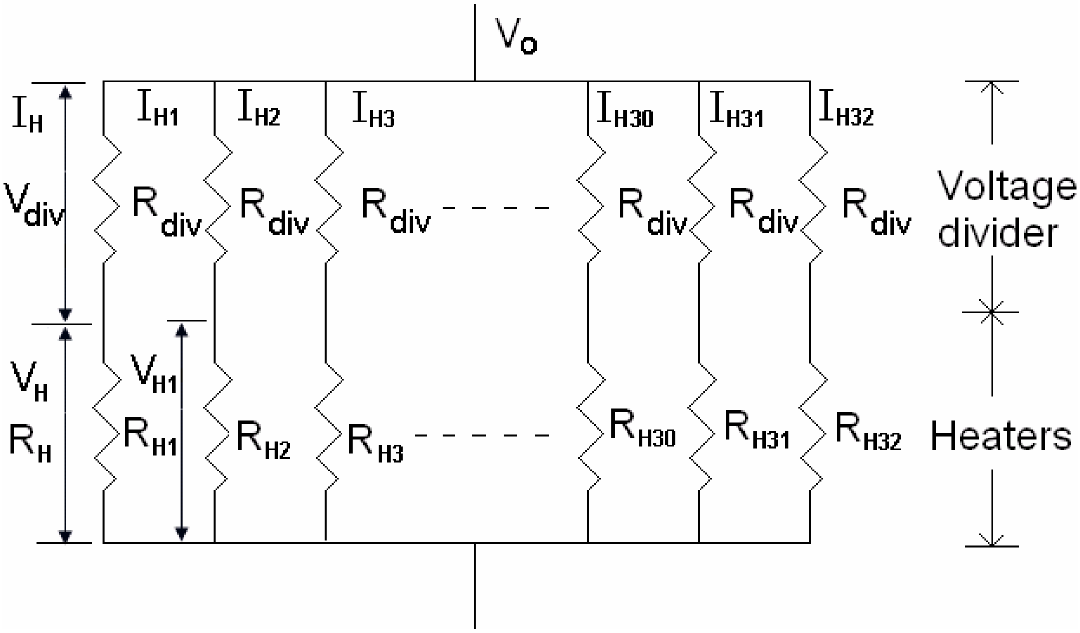

Fig. 3.2 Voltage divider

Fig. 3.2 is a voltage divider. With this voltage divider, we can measure the exact resistances of our microheater lines. Since the resistance of the voltage divider is fixed and input voltage is constant, we can easily calculate the voltage of the voltage divider. After we get the value of the voltage divider, we can get the current value of the heater and then the resistance of the heater. With these current and resistance values, we can calculate the power of the microheater. The following equations are for the calculation of microheater resistance and current values.

From Fig. 3.2,

$$V_{div} = V_o - V_H = I_H R_{div}$$

$$I_H = \frac{V_o - V_H}{R_{div}} \tag{3.3}$$

$$R_H = \frac{V_H}{I_H} = V_H \frac{R_{div}}{V_o - V_H} \tag{3.4}$$

From $V_o = I_H (R_{div} + R_H)$,

$$I_H = \frac{V_o}{R_{div} + R_H} \tag{3.5}$$

$$P_H = I_H^2 R_H = \frac{R_H V_o^2}{(R_{div} + R_H)^2} \tag{3.6}$$

where, *H* means heater and *div* means voltage divider. With Eqs. (3.4) and (2.1), we can easily calculate the temperature of the microheater.

Each line heater with identical resistance of approximately 6.63Ω is serially connected to a 51Ω resistor, as a voltage divider. The measured voltage across the 51Ω resistor determines the current as $I_H = V_{divider}/R_{divider}$ (= 50 Ω), the resistance of the line heater is calculated from $R_{heater} = (V_{total} - V_{divider})/I_H$, and the line heater temperature is determined from the resistance-temperature equation, Eq. (2.1). The heat flux is determined by the power consumption of the line heater, i.e., I^2R_{heater}. All experimental procedures including the data acquisition are recorded in PC by the Labview® software. Canon Macrolens FD 50mm captured dynamic images of evaporating droplets.

A precision 10-μl syringe is used to apply water droplets at three different volumes of 3μl, 5μl, and 10μl, on the heater array surface. Before each experiment, the microheater surface is thoroughly cleaned with 99.9% isopropyl alcohol and then dried for 30 minutes in a clean environment to ensure a dust-free and stain-free surface. The tested water droplets ranged from 2.1mm (3μl droplet) to 3.1mm (10μl droplet) in diameter before wetting.

When the droplet volume is sufficiently small, surface tension dominates the droplet's shape upon contact with a solid surface due to negligible gravitational deformation. This assumption is known to be valid when the total droplet volume is less than 1μl [27]. The larger droplets are distorted from the spherical cap shape because of gravity. The spherical cap assumption conditions are still in dispute as evidenced in numerous published articles (for example, [28]). Padday and Philos [29] proposed an oblate hemi-ellipsoid model, and Erbil and Meric [30] proposed ellipsoidal cap geometry for the droplet shape regardless of its volumetric size.

The spherical cap model [31, 32], thus, may be applied to determine the initial contact angle (θ) and the height (h) of the spread droplet that is assumed to have a perfectly spherical “cap” shape:

$$V = \frac{\pi r_o^3 (1-\cos\theta)^2 (2+\cos\theta)}{3\sin^3\theta} \qquad (3.7)$$

$$\tan\left[\frac{\theta}{2}\right] = \frac{h}{r_o} \qquad (3.8)$$

Using Eqs. (3.7) and (3.8) the initial contact angles and heights are calculated as 97.83° and 1.204mm for the 3μl droplet, and as 99.07° and 1.817mm for the 10μl droplet, assuming perfect sphericity.

The results seem to conflict with the generally known fact that the constant contact area evaporation is observed when the contact angle is less than 90 degrees [32-34]. However, since gravity tends to flatten the spherical shape into an ellipsoid, it is the author’s belief that the calculated results have been somewhat overestimated compared with the actual contact angles and heights. Bourges and Shanahan [31] presented a measured initial contact angle of approximately 88 degrees, for the case of 4μl water droplet contacting an epoxy resin surface, and the angle continually decreased thereafter.

Since the present SU-8 coated contact surface shares similar material characteristics as an epoxy surface (http://www.geocities.com/guerinlj/), the contact angles of the tested droplets are estimated to be somewhat less than 90°. In addition, Crafton et al. [11] also showed that water droplets under a similar contact surface maintain nearly constant contact area during evaporation while the droplet heights and contact angles both continually decrease from their initial values.

Figs. 3.3 to 3.11 show sequential images of the evaporation progress of water droplets from a 3μl droplet at 40 º C to a 10μl droplet at 80ºC. At the beginning of evaporation at $t/\tau = 0$, water contacts the heater surface, and it maintains the same contact area until the evaporation is nearly complete. The diameter of the droplet remains the same until completing about 90% of the evaporation time, and then the droplet diameter begins to shrink in a rapid manner. For all tested conditions of the three different droplets (3, 5, and 10μl volume), and three different dry temperatures (40, 60, and 80°C), the constant-area evaporation prevails, and their evaporation processes are qualitatively similar.

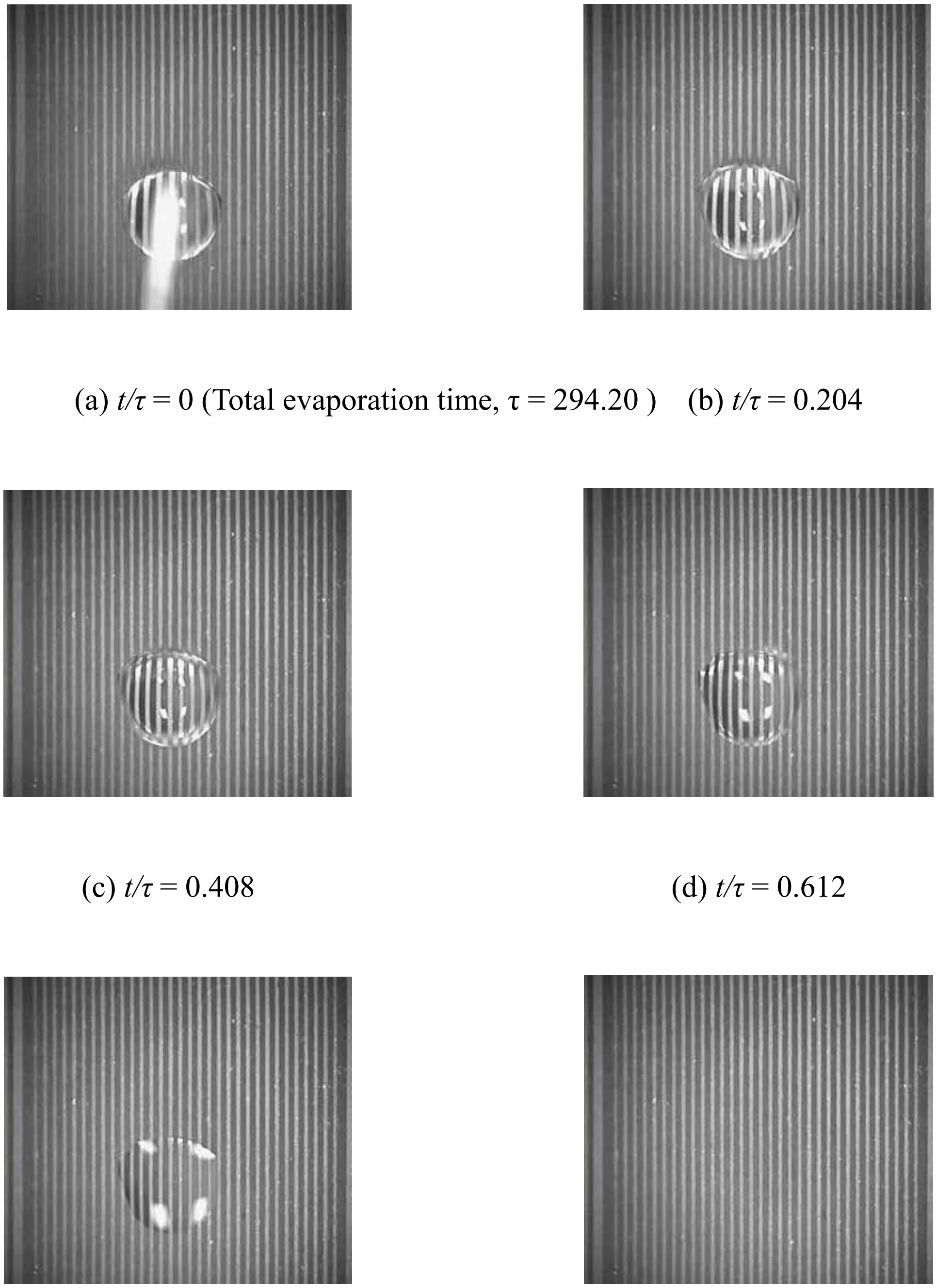

(a) $t/\tau = 0$ (Total evaporation time, $\tau = 294.20$)   (b) $t/\tau = 0.204$

(c) $t/\tau = 0.408$ (d) $t/\tau = 0.612$

(e) $t/\tau = 0.816$ (f) $t/\tau = 0.989$

Fig. 3.3 Sequential images of slowly evaporating water droplets on the microheater array at T_{dry} = 40°C, 3μl

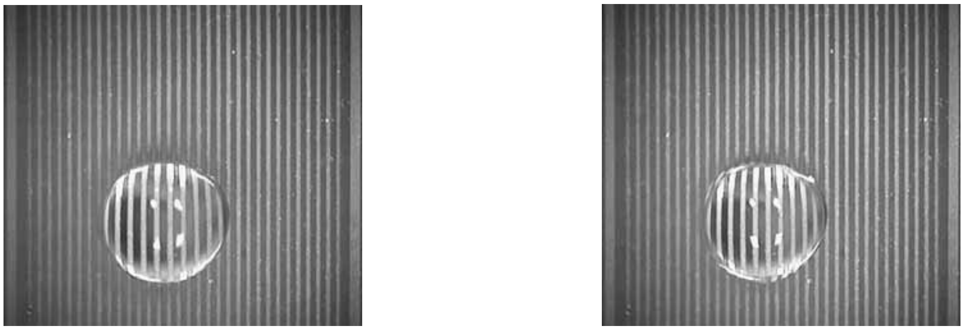

(a) $t/\tau = 0$ (Total evaporation time, $\tau = 369.10$)

(b) $t/\tau = 0.217$

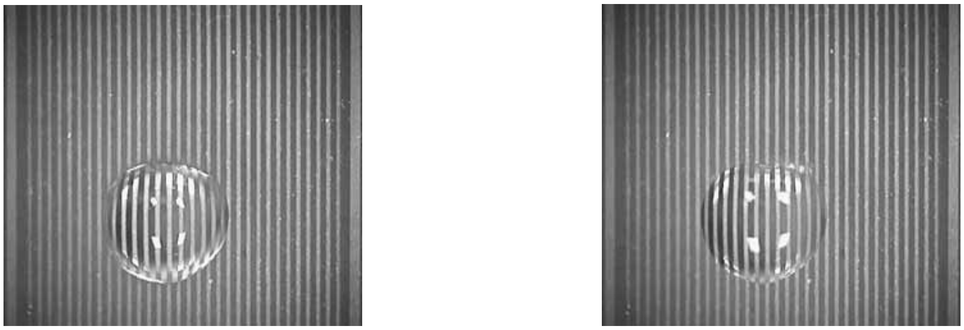

(c) $t/\tau = 0.433$

(d) $t/\tau = 0.650$

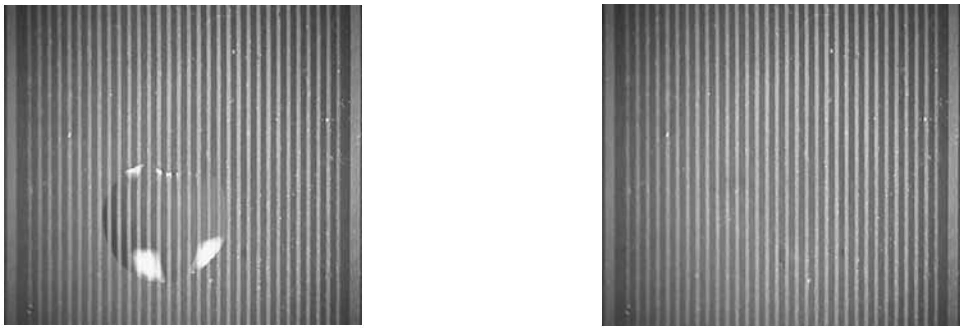

(e) $t/\tau = 0.867$

(f) $t/\tau = 0.989$

Fig. 3.4 Sequential images of slowly evaporating water droplets on the microheater array at T_{dry} = 40°C, 5μl

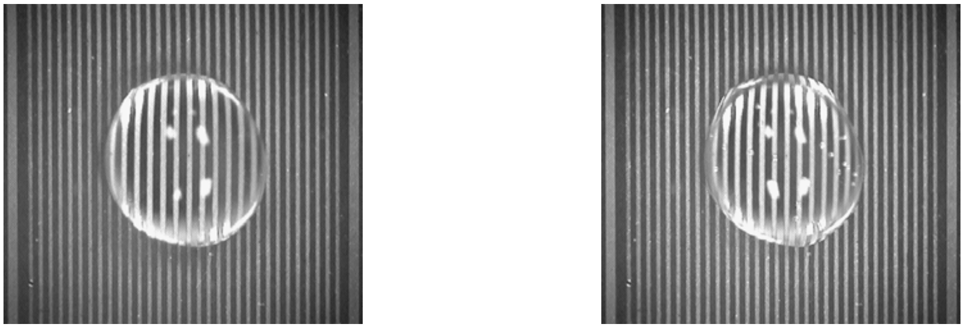

(a) $t/\tau = 0$ (Total evaporation time, $\tau = 724.24$)

(b) $t/\tau = 0.207$

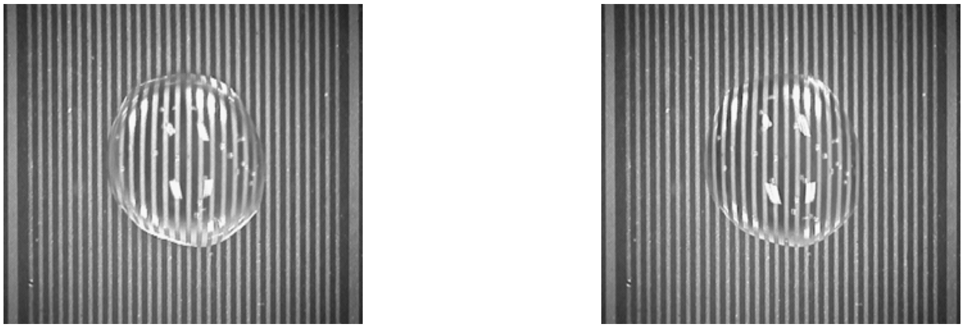

(c) $t/\tau = 0.414$

(d) $t/\tau = 0.620$

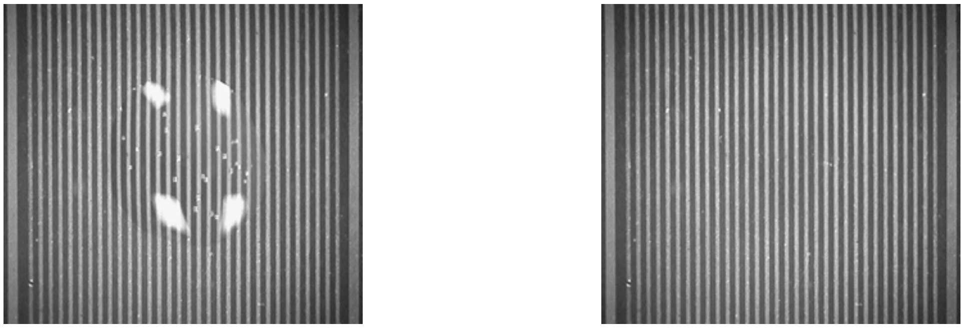

(e) $t/\tau = 0.827$

(f) $t/\tau = 0.993$

Fig. 3.5 Sequential images of slowly evaporating water droplets on the microheater array at T_{dry} = 40°C, 10μl

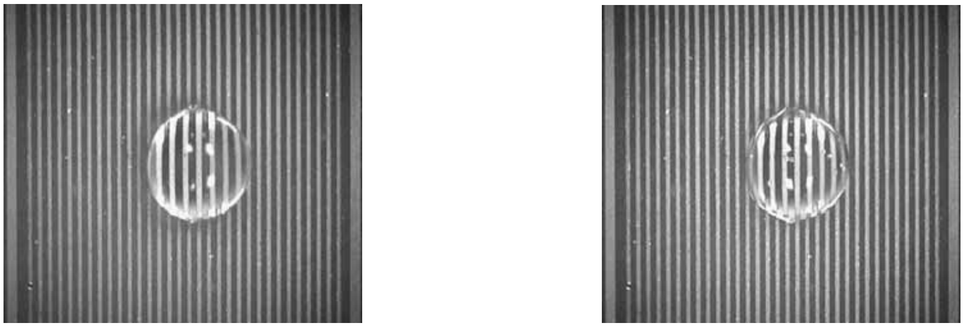

(a) $t/\tau = 0$ (Total evaporation time, $\tau = 115.23$) (b) $t/\tau = 0.208$

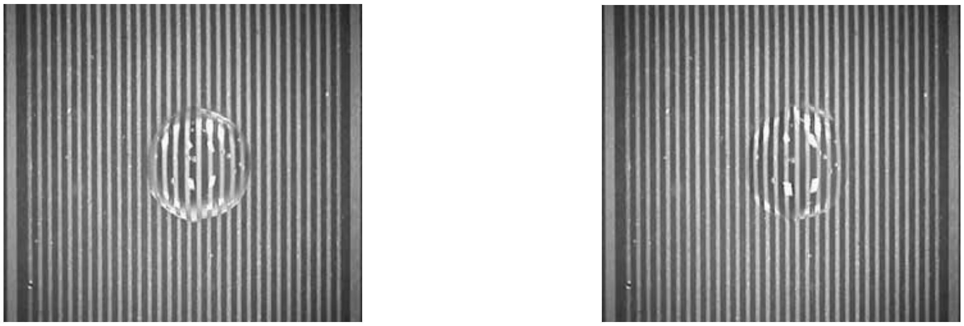

(c) $t/\tau = 0.417$ (d) $t/\tau = 0.625$

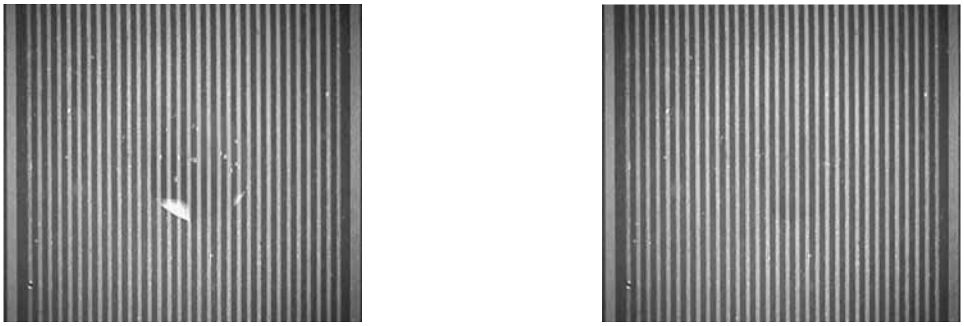

(e) $t/\tau = 0.833$ (f) $t/\tau = 0.981$

Fig. 3.6 Sequential images of slowly evaporating water droplets on the microheater array at T_{dry} = 60°C, 3μl

(a) $t/\tau = 0$ (Total evaporation time, $\tau = 292.56$) (b) $t/\tau = 0.196$

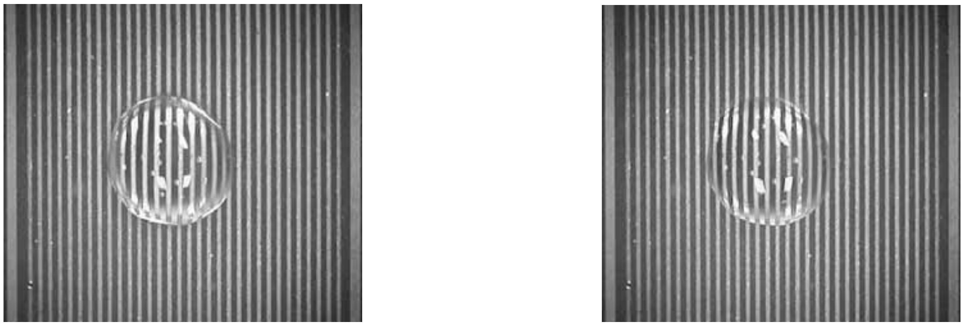

(c) $t/\tau = 0.393$ (d) $t/\tau = 0.589$

(e) $t/\tau = 0.785$ (f) $t/\tau = 0.993$

Fig. 3.7 Sequential images of slowly evaporating water droplets on the microheater array at T_{dry} = 60°C, 5μl

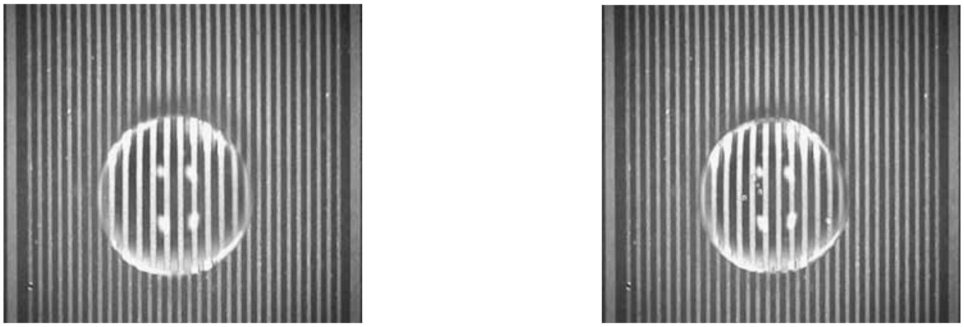

(a) $t/\tau = 0$ (Total evaporation time, $\tau = 292.56$) (b) $t/\tau = 0.205$

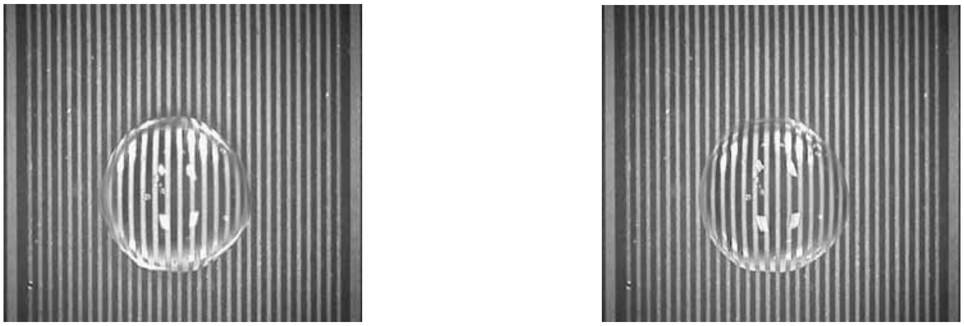

(c) $t/\tau = 0.410$ (d) $t/\tau = 0.615$

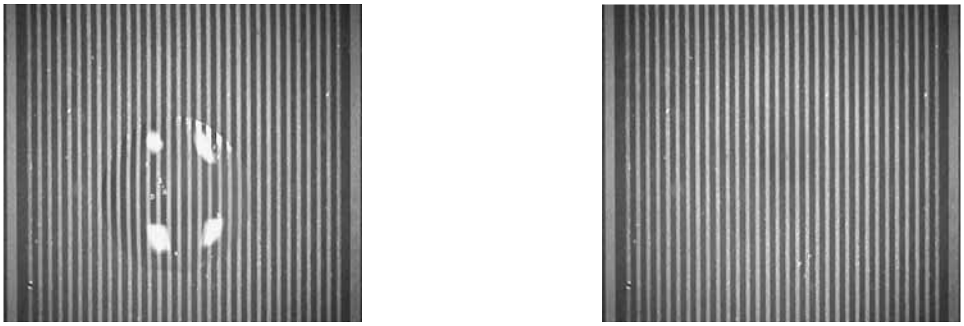

(e) $t/\tau = 0.820$ (f) $t/\tau = 0.991$

Fig. 3.8 Sequential images of slowly evaporating water droplets on the microheater array at T_{dry} = 60°C, 10μl

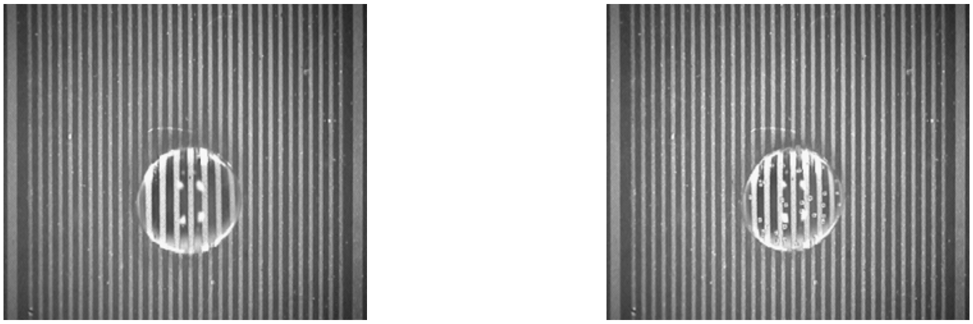

(a) t/τ = 0 (Total evaporation time, τ =70.75) (b) t/τ = 0.205

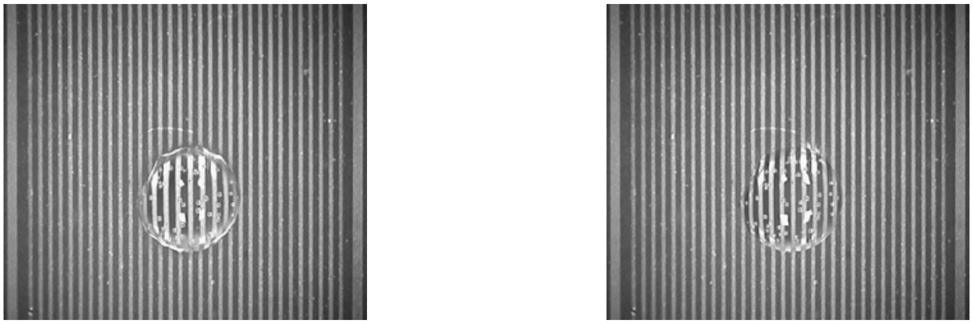

(c) t/τ = 0.410 (d) t/τ = 0.615

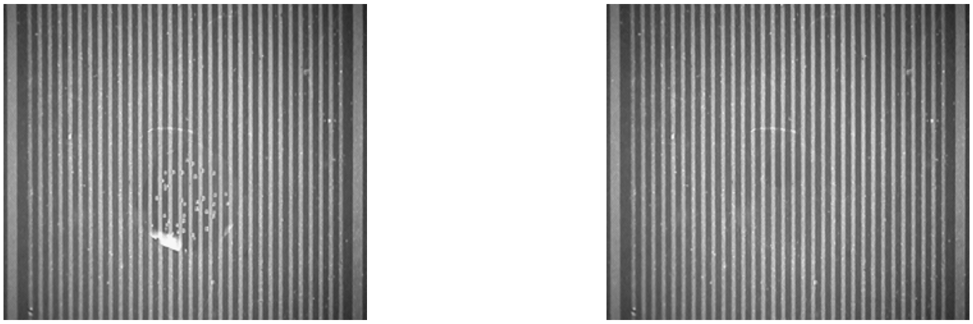

(e) t/τ = 0.820 (f) t/τ = 0.991

Fig. 3.9 Sequential images of slowly evaporating water droplets on the microheater array at T_{dry} = 80°C, 3μl

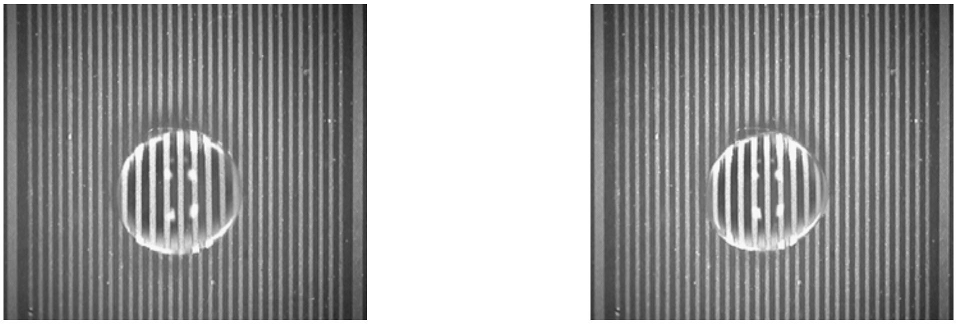

(a) $t/\tau = 0$ (Total evaporation time, $\tau = 100.06$) (b) $t/\tau = 0.200$

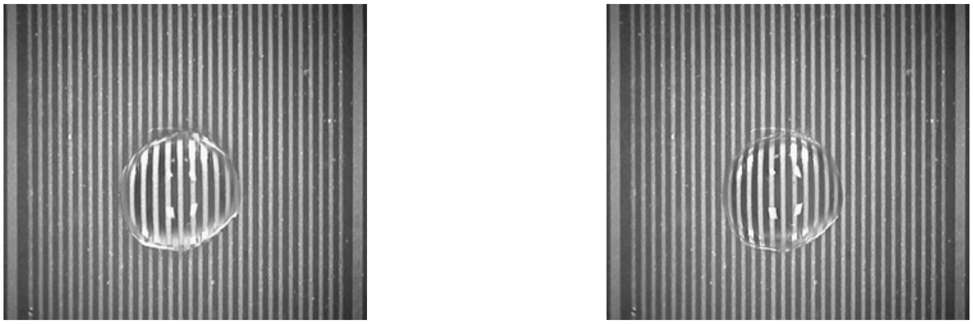

(c) $t/\tau = 0.400$ (d) $t/\tau = 0.600$

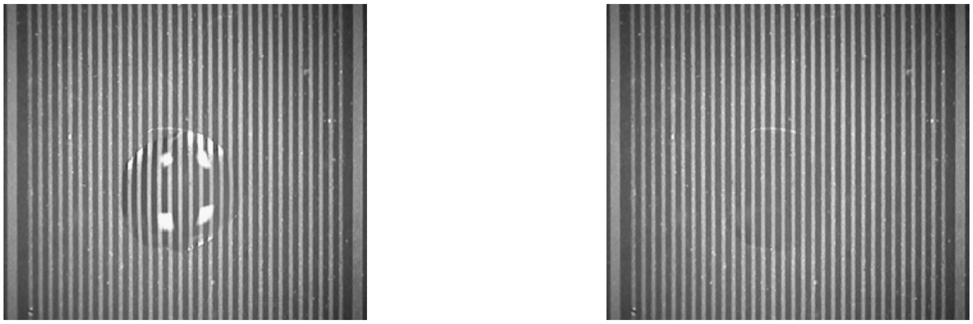

(e) $t/\tau = 0.800$ (f) $t/\tau = 0.979$

Fig. 3.10 Sequential images of slowly evaporating water droplets on the microheater array at T_{dry} = 80°C, 5μl

(a) $t/\tau = 0$ (Total evaporation time, $\tau = 142.23$) (b) $t/\tau = 0.225$

(c) $t/\tau = 0.450$ (d) $t/\tau = 0.675$

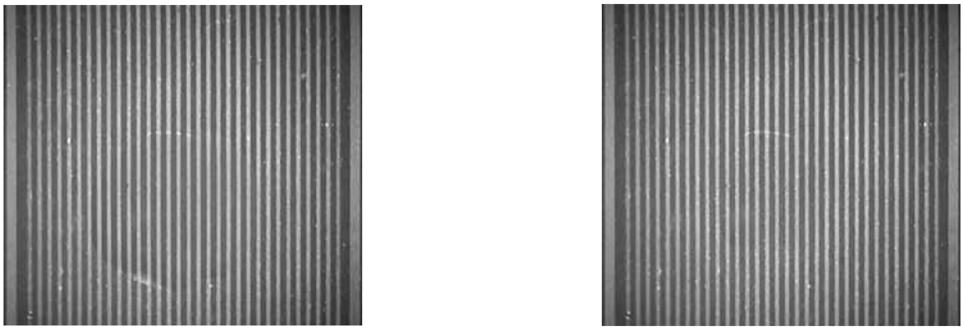

(e) $t/\tau = 0.900$ (f) $t/\tau = 0.984$

Fig. 3.11 Sequential images of slowly evaporating water droplets on the microheater array at T_{dry} = 80°C, 10µl

Table 3.2 Measured dry-out time (τ in seconds) for complete evaporation of droplet for three different droplet volumes and three different dry-surface temperatures. (Evaporation time defined as the time between droplet hit the heater surface and the time droplet thorough evaporation.)

Droplet Volume (μl) → Dry-Surface Temperature (°C)	3 (1.05-mm diameter)	5 (1.25-mm diameter)	10 (1.55-mm diameter)
40	294	369	724
60	115	163	293
80	71	100	142

The dry-out times (Table 3.2) of the tested droplets persistently increase with increasing droplet volume and with decreasing dry-surface temperature. The wetting droplet diameter *R* is measured as 1.05, 1.25, and 1.55 mm, respectively. The larger droplet increases the contact area between the droplet and the heater surface, and the increased heated surface makes the evaporation rate faster. While the droplet volume increases more than three times from 3 μl to 10 μl, the dry-out time increases less than three times because the contact area increases by 2.2 times, and the evaporation rate is proportional to the contact area.

3.3 Line-Averaged Raw Data

The "line-averaged" data are determined from measurements of the overall resistance variation of the heater line, assuming a uniform temperature for the entire heater surface at any given instant of time. Note that this is not a precise representative for wetted heater elements where strong temperature gradients exist on each element. Figs. 3.12 to 3.14 show line-averaged spatial temperature distributions of the microheater. As the temperature of the heater goes up, temperature variation is also enlarged, and at the center of the droplet, the temperature drop is the most for all 9 experiment cases.

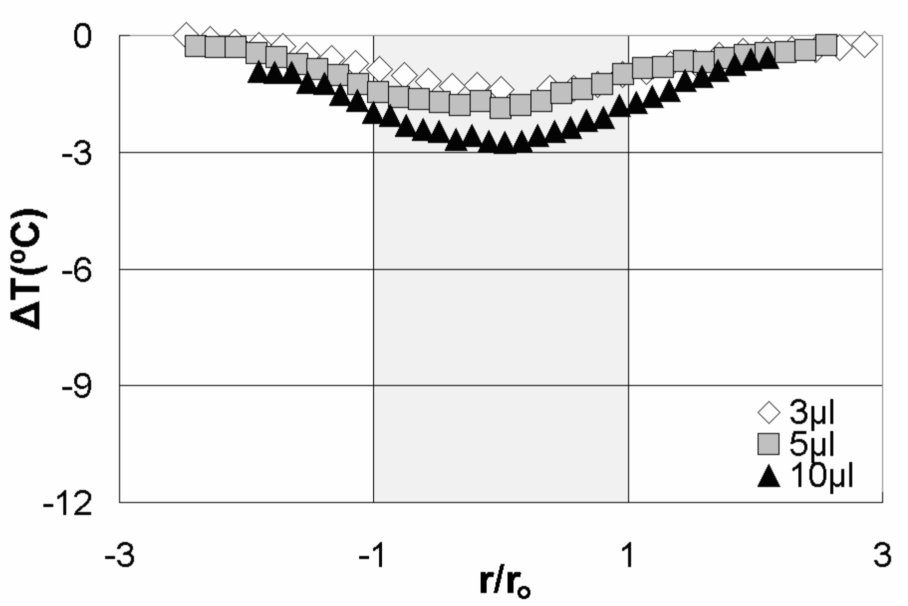

(a) t/τ = 0.01

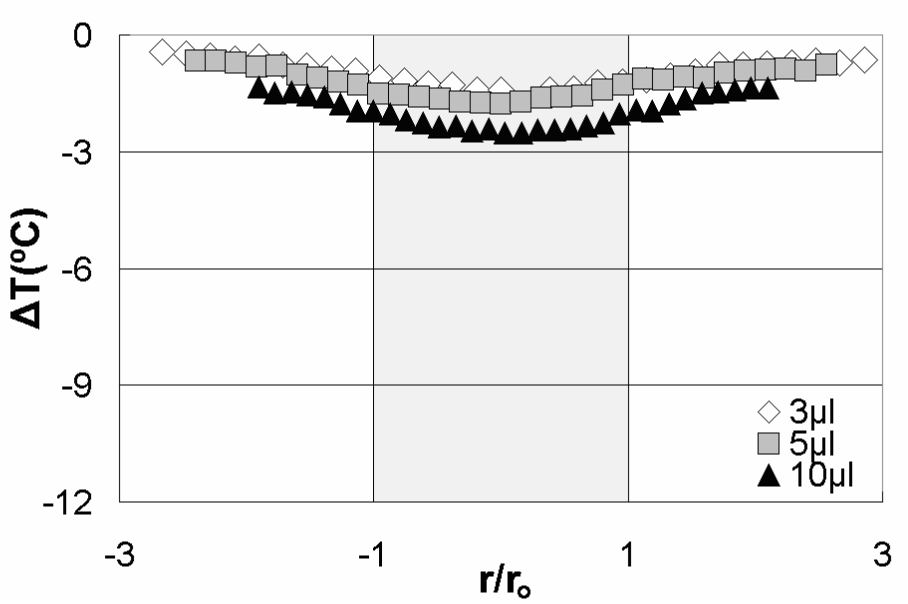

(b) t/τ = 0.1

Fig. 3.12 Line-averaged temperature drop profile at T_{dry} = 40°C

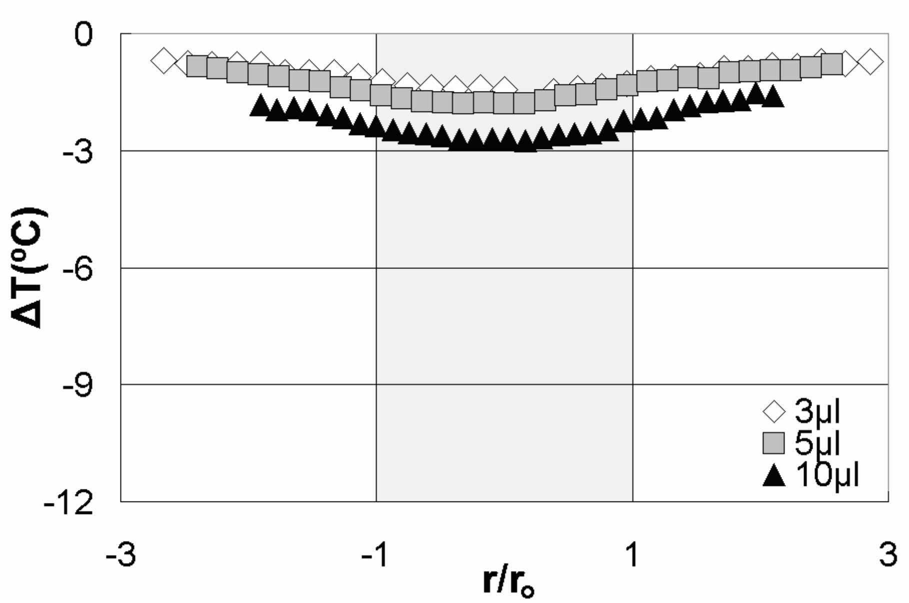

(c) t/τ = 0. 5

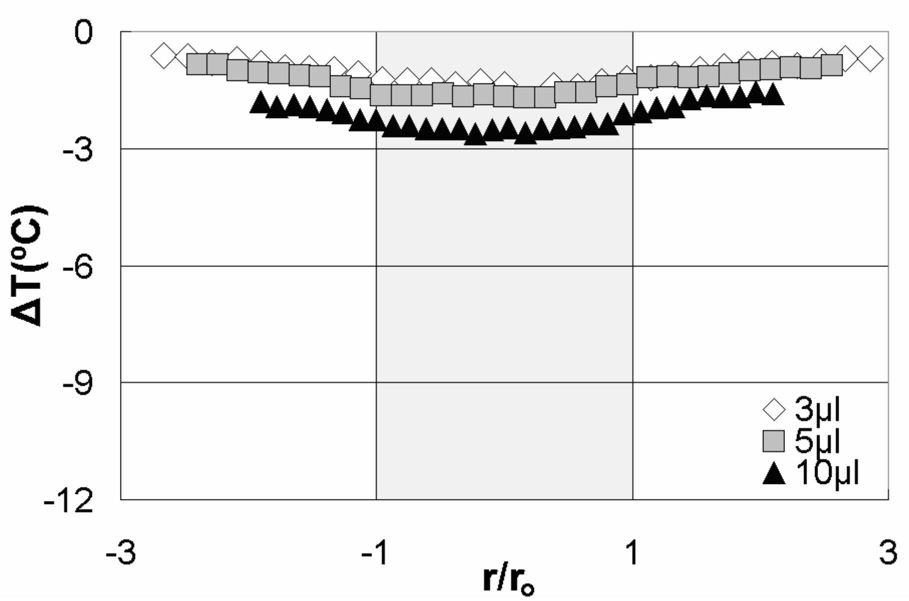

(d) t/τ = 0. 9

Fig. 3.12 Continued

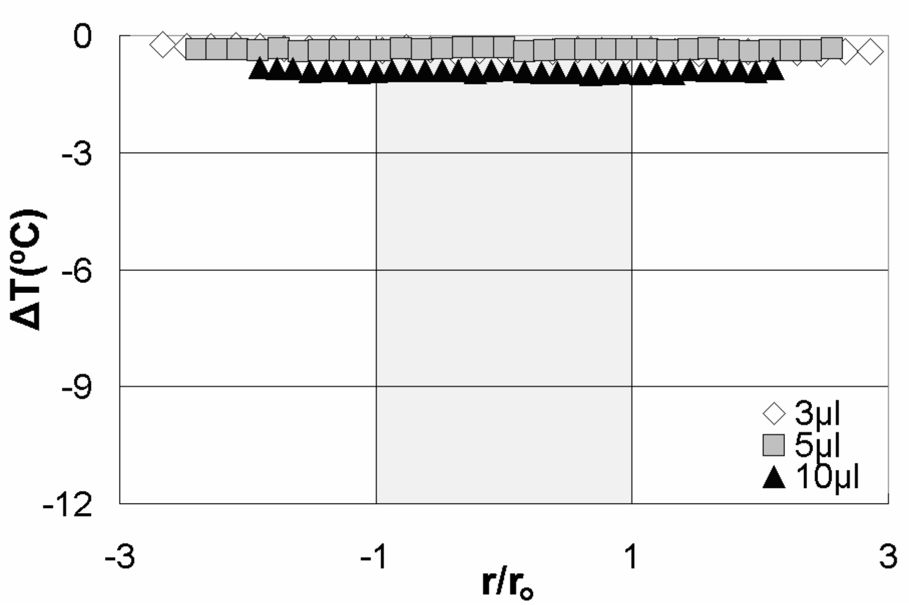

(e) t/τ = 1.1

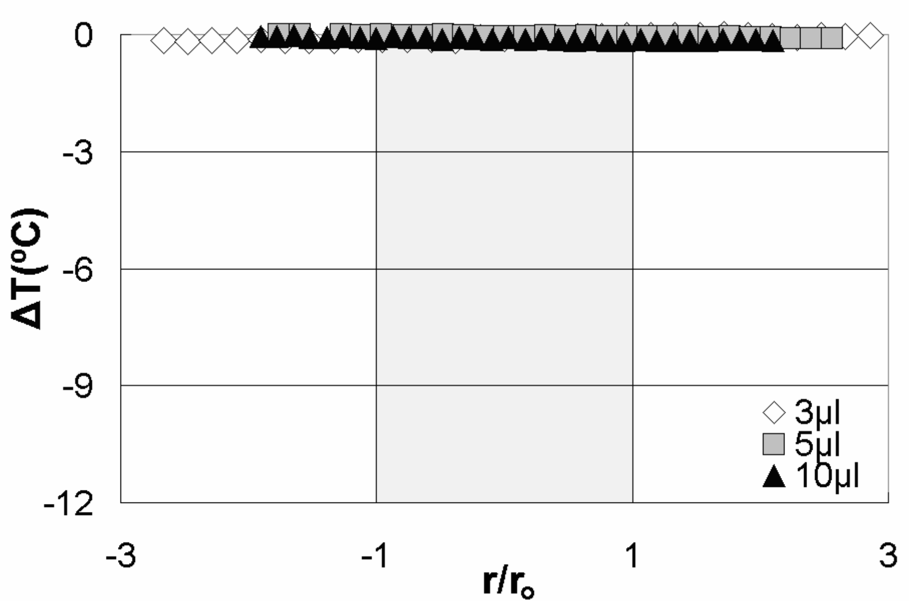

(f) t/τ = 2.0

Fig. 3.12 Continued

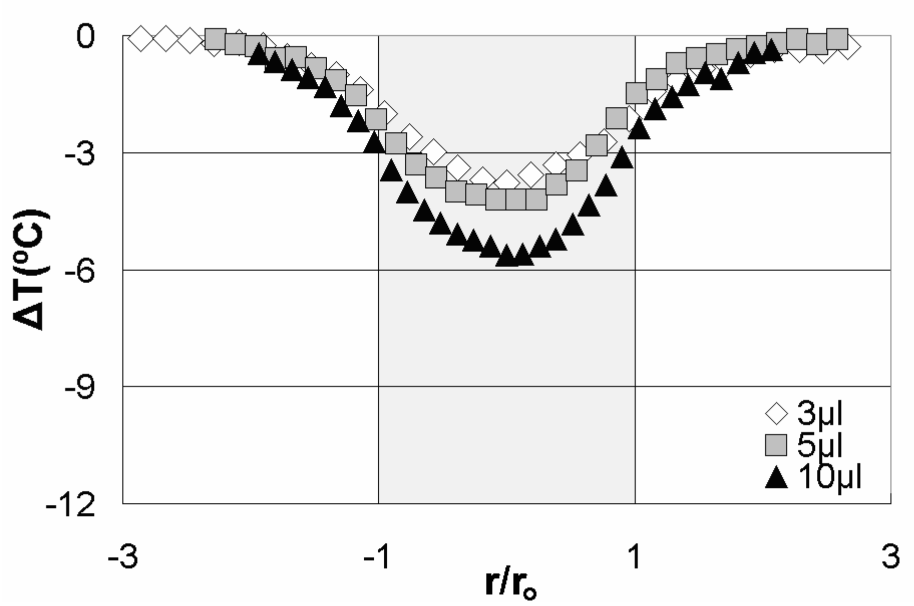

(a) t/τ = 0.01

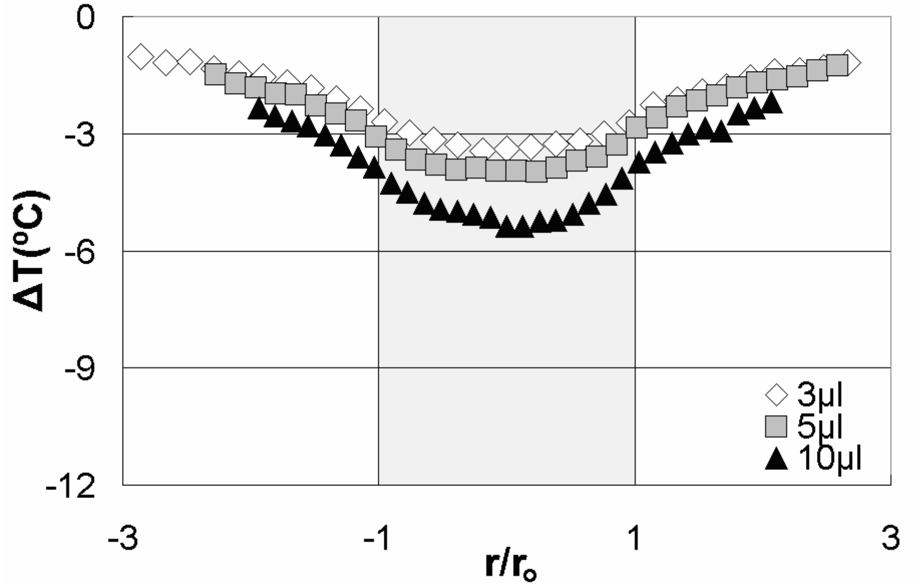

(b) t/τ = 0.1

Fig. 3.13 Line-averaged temperature drop profile at T_{dry} = 60°C

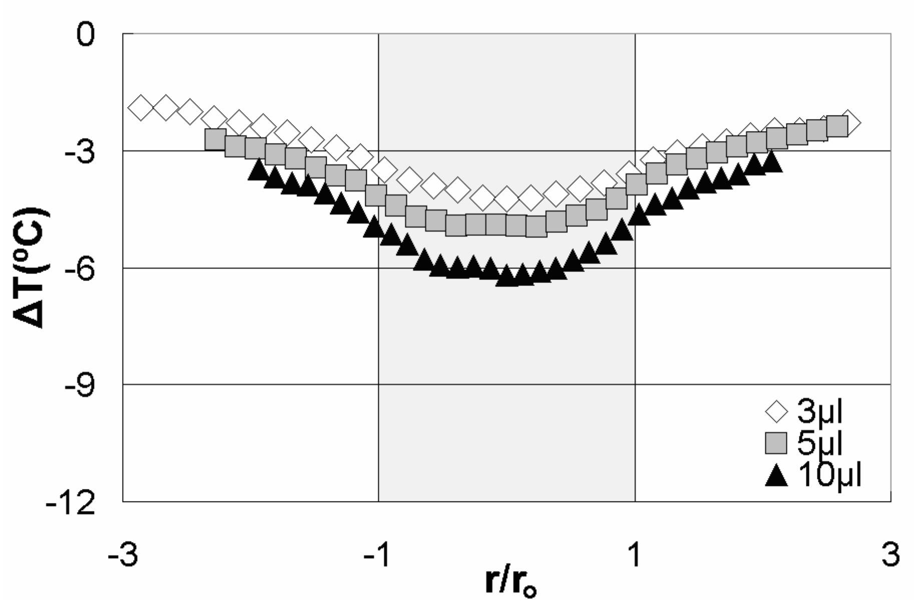

(c) t/τ = 0.5

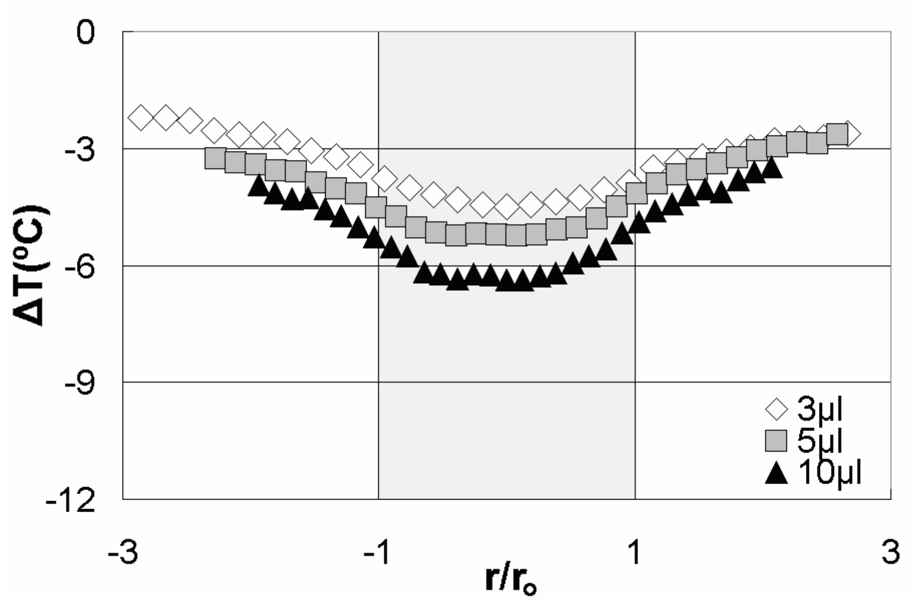

(d) t/τ = 0.9

Fig. 3.13 Continued

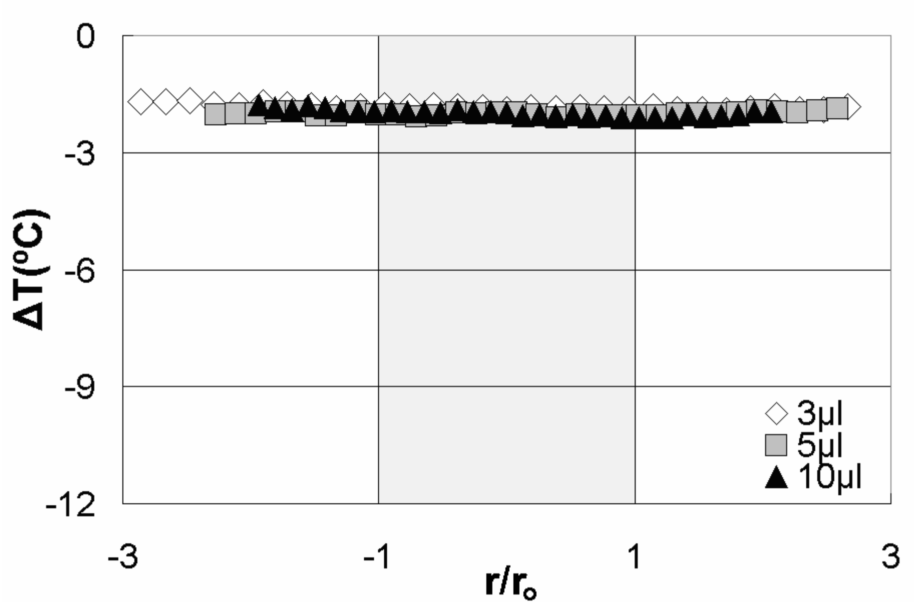

(e) t/τ = 1.1

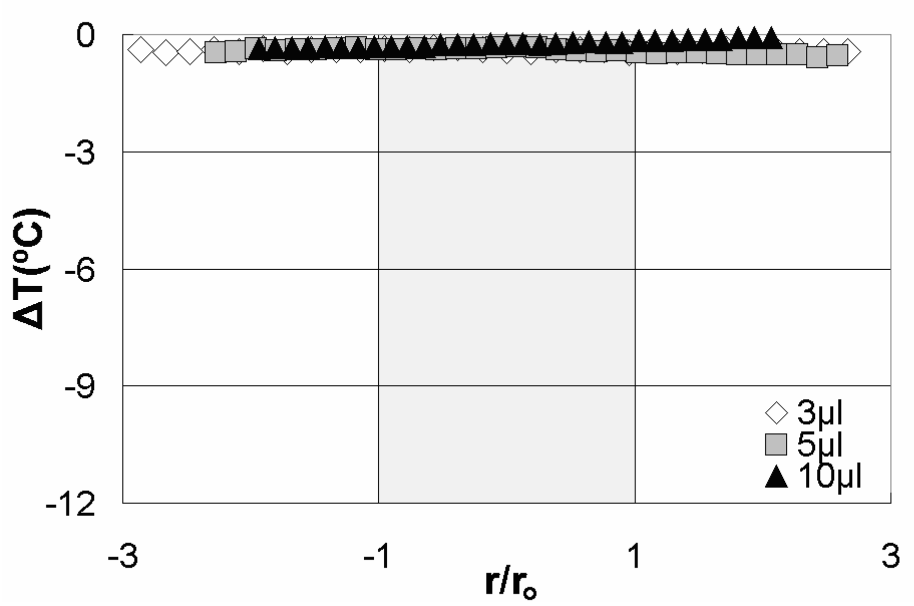

(f) t/τ = 2.0

Fig. 3.13 Continued

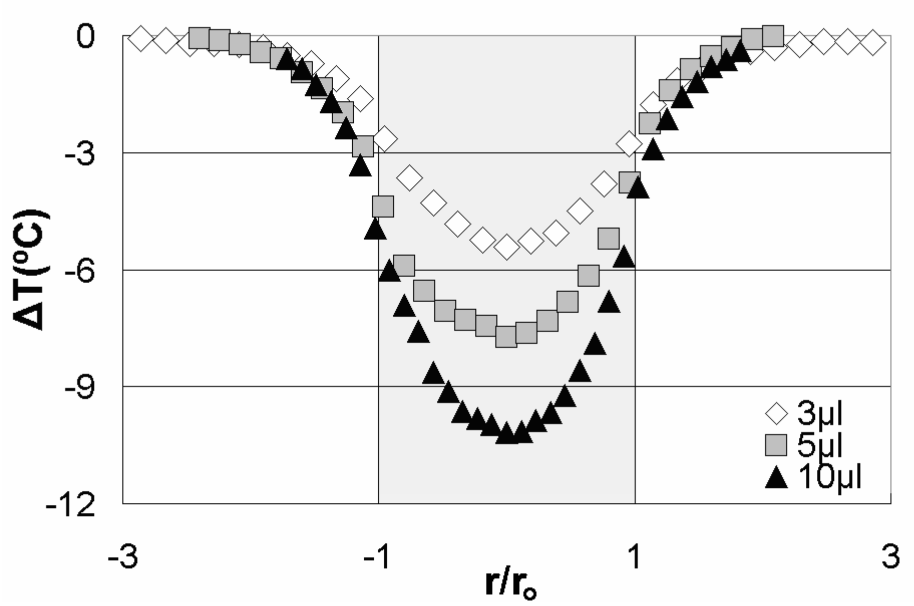

(a) t/τ = 0.01

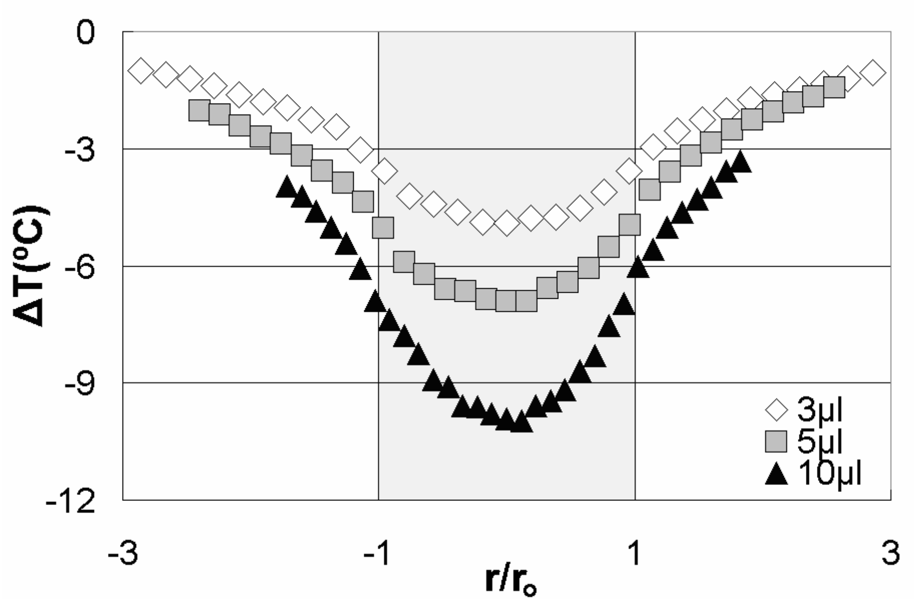

(b) t/τ = 0.1

Fig. 3.14 Line-averaged temperature drop profile at T_{dry} = 80°C

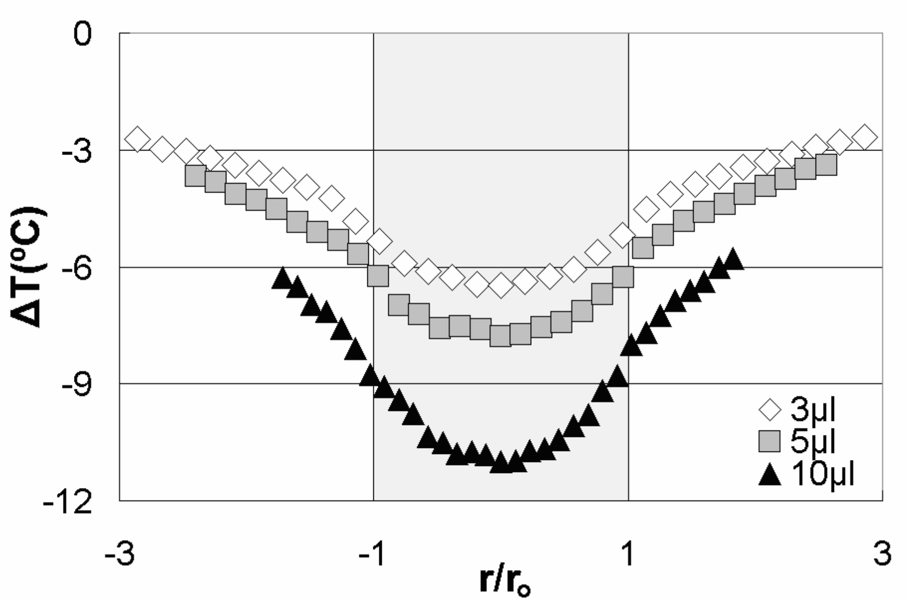

(c) t/τ = 0.5

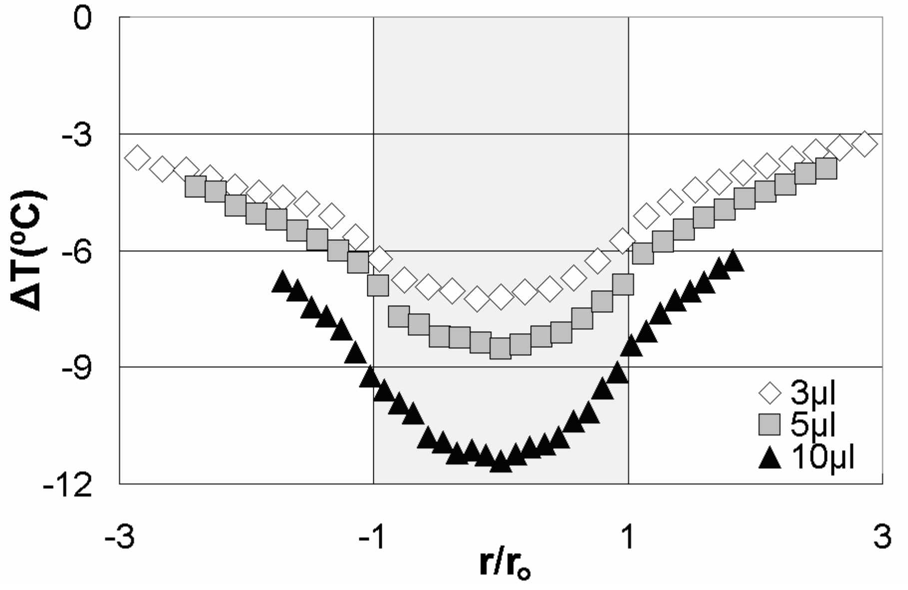

(d) t/τ = 0.9

Fig. 3.14 Continued

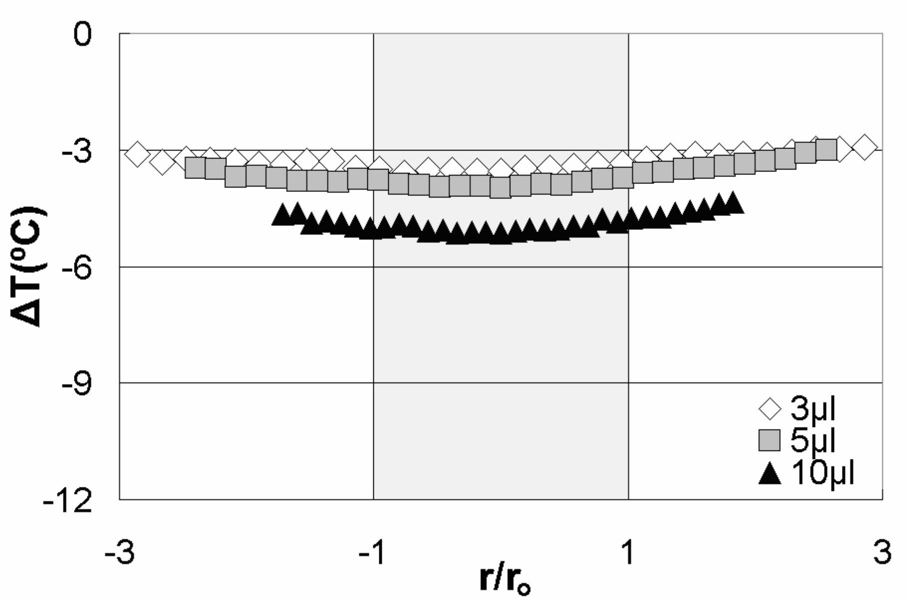

(e) t/τ = 1.1

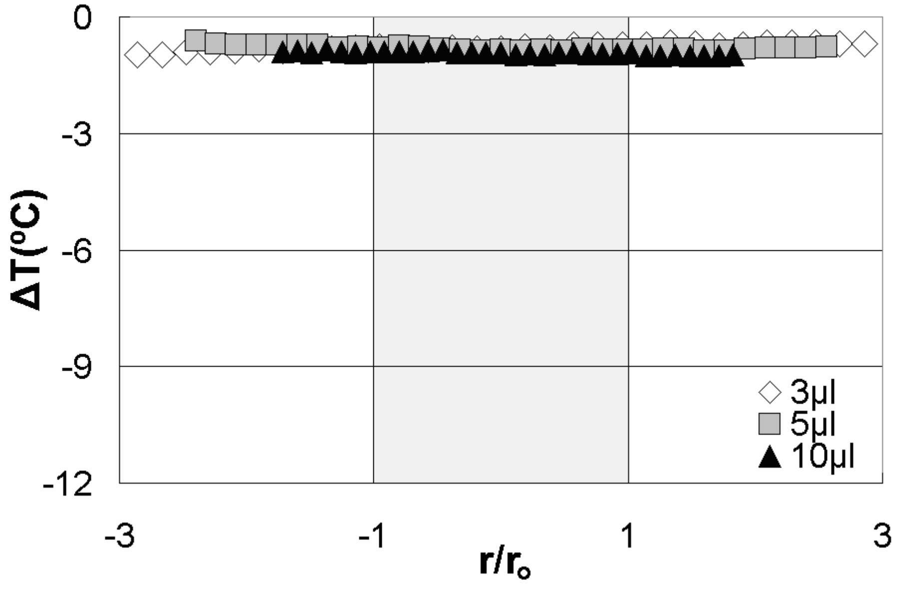

(f) t/τ = 2.0

Fig. 3.14 Continued

3.4 Tomographic deconvolution of line-averaged raw temperature data

The value of temperatures converted from the line-averaged resistance data are valid only if each heater is imposed to have a uniform temperature at any given instant of time. In reality, however, substantial temperature gradients exist since the different heat transfer characteristics between dry and wet sections prevail on a single heater surface, and the temperature gradient distribution varies in time as the droplet evaporation progresses.

In order to determine the distributed temperature profile accounting for the temperature gradients, tomographic conversion [35-37] is conducted to deconvolve the line-averaged data into radially distributing temperature profiles, assuming axi-symmetric evaporation and heat transfer. Fig. 3.15-a illustrates 8 concentric deconvolution zones for the axi-symmetric tomographic conversion. Zone I covers only the central region of the middle heater element (A). Zone II covers the central regions of the next two left (B) and right (C) heater elements as well as the two sub regions of the middle heater. Thus, Zone VIII includes partial regions from all 16 heater elements, from A to O. The entire tomographic conversion domain covers the circular region of 6.4mm in diameter, corresponding to the width of the 32-element heater array. 16 concentric zones are used for the actual tomographic conversion calculations, whereas only eight of them are presented in Fig. 3.15 for simplicity.

The sixteen unknown temperatures for the sixteen concentric zones must be determined from the sixteen line-averaged measured data points. Thus, sixteen

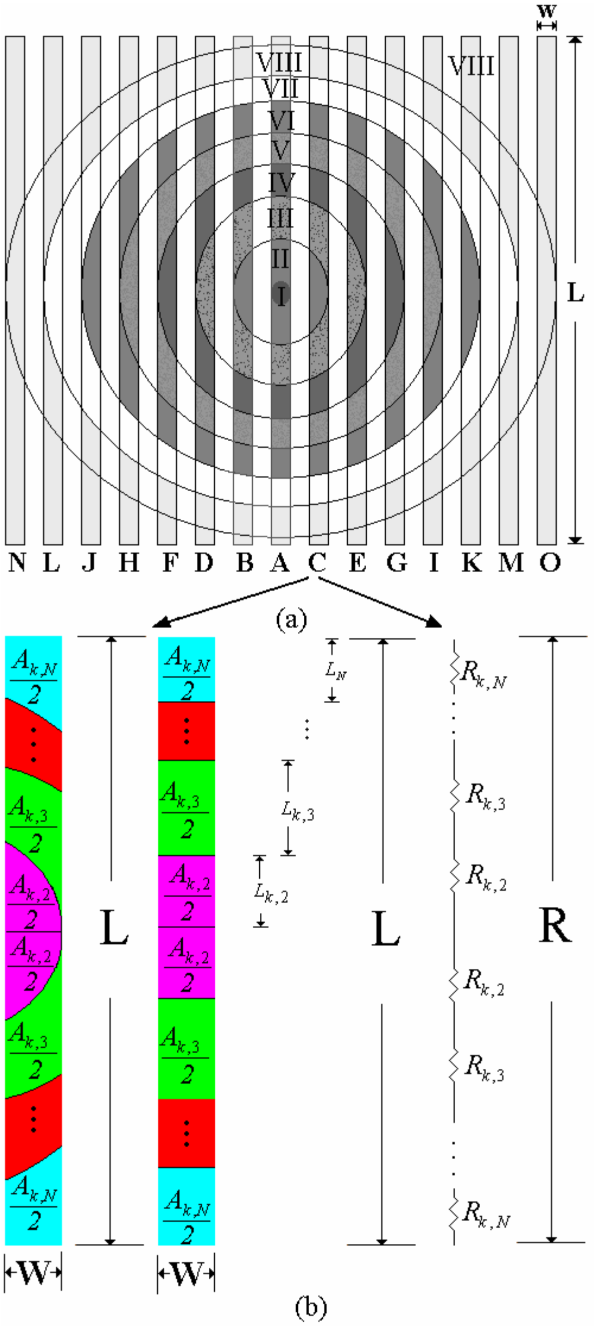

Fig. 3.15 Tomographic deconvoluted temperature zones (a) Eight zone tomographic deconvoluted heater area (b) Zone reconstruction for temperature calculation with electric resistance

linear algebraic equations correlating the line-averaged data with concentric temperature unknowns are established using the linear resistance/resistivity-temperature relations of Eqs. (1-a) and (1-b). The *k*-th line heater, as represented by the 2^{nd} line heater in Fig. 3.15-b, consists of concentric zones of $i = k, k+1, \ldots, N$ ($N = 16$), and its resistance is therefore given as,

$$R_k = \sum_{i=k}^{N} R_{k,i} = \sum_{i=k}^{N} \rho_{k,j} \frac{L_{k,j}}{w \cdot d} = \sum_{i=k}^{N} \rho_o \left[1 + \alpha\left(T_{k,i} - T_o\right)\right] \frac{L_{k,i}}{w \cdot d} = \frac{\rho_o L}{w \cdot d} + \frac{\rho_o \alpha}{w \cdot d} \sum_{i=k}^{N} \left(T_{k,i} - T_o\right) L_{k,i} \tag{3.9}$$

where, *w* and *d* are line heater width and thickness, respectively, and $\sum_{i=k}^{N} L_{k,i} = L$.

Assuming a rectangular area for each sub-zone of the *k*-th heater line, the equivalent heater length of the sub-zone is given as,

$$L_{k,i} = \frac{A_{k,i}}{w} \tag{3.10}$$

Substituting Eq. (3.10) into Eq. (3.9) gives,

$$R_k = \frac{\rho_o L}{w \cdot d} + \frac{\rho_o \alpha}{w \cdot d \cdot w} \sum_{i=k}^{N} \left(T_{k,i} - T_o\right) A_{k,i} \tag{3.11}$$

On the other hand, the measured line-averaged resistance is expressed as,

$$R_k = \rho_o\left[1+\alpha\left(T_k - T_o\right)\right]\frac{L}{w\cdot d} \qquad (3.12)$$

where, T_k represents the averaged temperature of the k^{th} line heater, i.e., $T_k \equiv \sum_{i=k}^{N} T_{k,i}$.

Combining Eqs. (3.11) and (3.12),

$$T_k = \frac{1}{L\cdot w}\sum_{i=k}^{N} T_{k,i}A_{k,i} \qquad (3.13)$$

where the left-hand side presents the measured line-averaged temperature data and the deconvoluted temperature data for each concentric zone, $T_{k,i}$, can be calculated one by one starting from the outmost heater where the heater temperature is uniform and equal to the dry heater temperature.

The temporal developments of the droplet (10-μl) center temperature are shown for the line-averaged profile (red line) and for the tomographically deconvoluted profile (blue line) in Fig. 3.16. Also shown is the temperature variation for the case of flooding (black line) at about the same height of the wetted droplet of 10-μl.

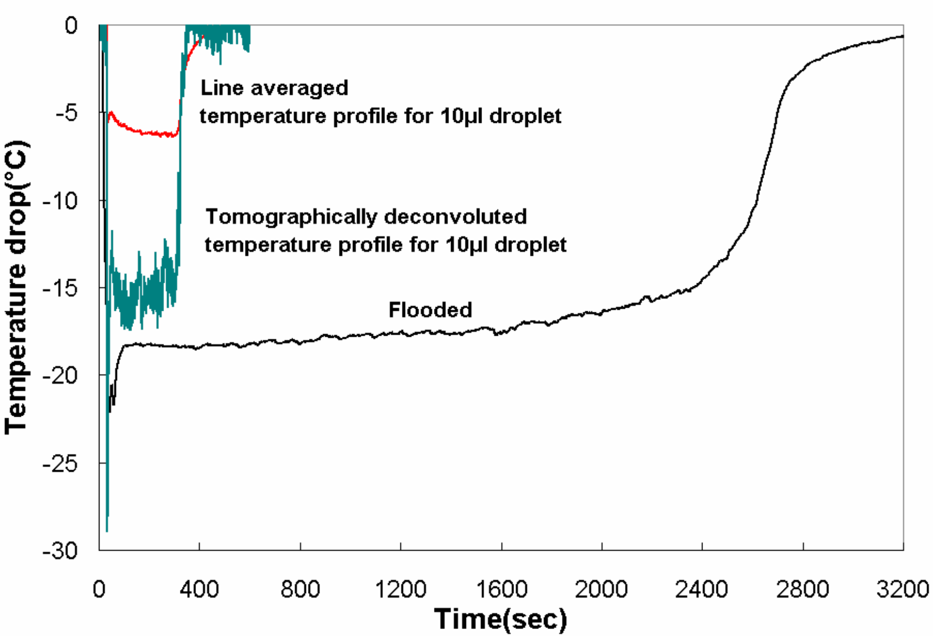

Fig. 3.16 Temperature variation of droplet center on the microheater (for 10µl data, both of them are 100 data moving average method was used)

The droplet evaporation is expected to result in slightly less of a temperature drop compared with the flooded evaporation since the droplet is surrounded by dry heater area, and this dry part supplies extra heat through the conduction by the glass substrate, as well as the convection through nearby air. The line-averaged data, however, unacceptably deviates from the flooded case and fails to predict physically valid temperature history. The overly smoothed line-averaged data also overlooks the temperature fluctuations occurring from the fluid motion inside the droplet, which are driven by the interfacial thermocapillary stress and thermally induced buoyancy.

3.5. Results and discussion

Figs. 3.17-3.19 show temporal development of tomographically deconvoluted temperature profiles for 3μl, 5μl, and 10μl droplets for the case of 40°C, 60°C, 80°C dry heater temperature.

When the radial distance is normalized by the wet radius of each droplet, all three profiles for the three droplets collapse together showing similar development for practically the entire test period. Upon contact, the largest ΔT is a result of the instantaneous maximum cooling rate (Figs. 3.17-3.19-a). ΔT remains nearly unchanged during the evaporation in which a latent heat transfer process at a constant temperature prevails (Figs. 3.17-3.19-b to d). Then ΔT returns to the dry heater temperature after completion of evaporation (Figs. 3.17-3.19-e) and fully recovers to the dry heater temperature in $t = 2.0\,\tau$ (Figs. 3.17-3.19-f).

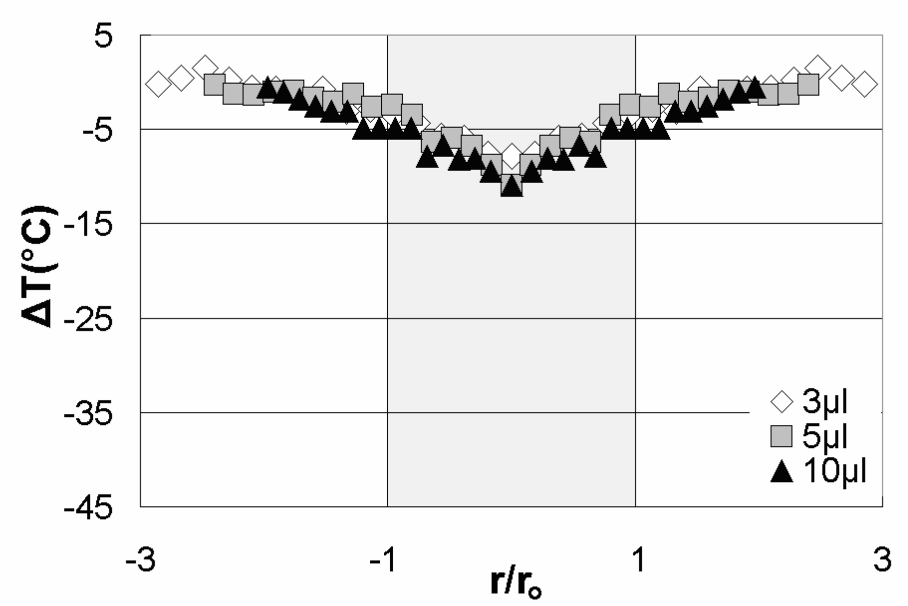

(a) t/τ = 0.01

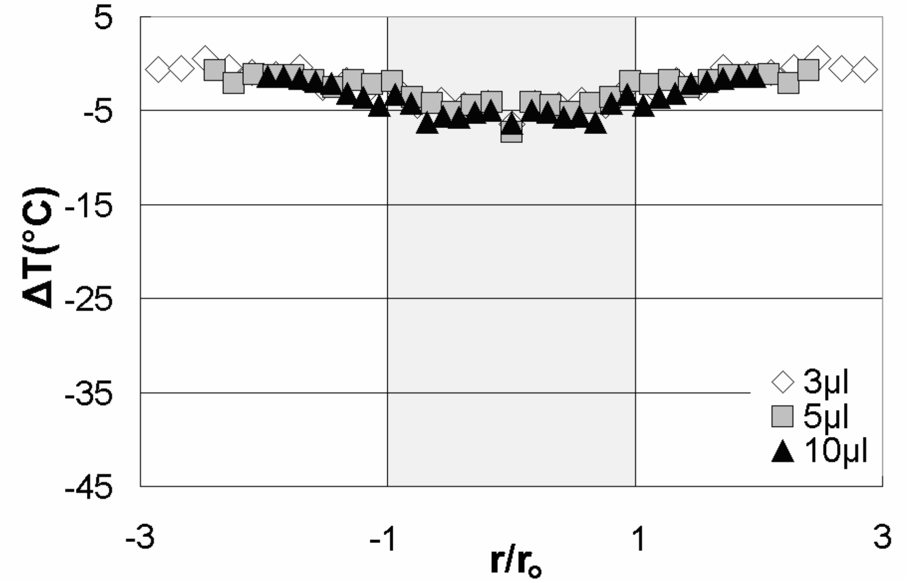

(b) t/τ = 0.1

Fig. 3.17 Tomographic temperature drop profile at T_{dry} = 40°C

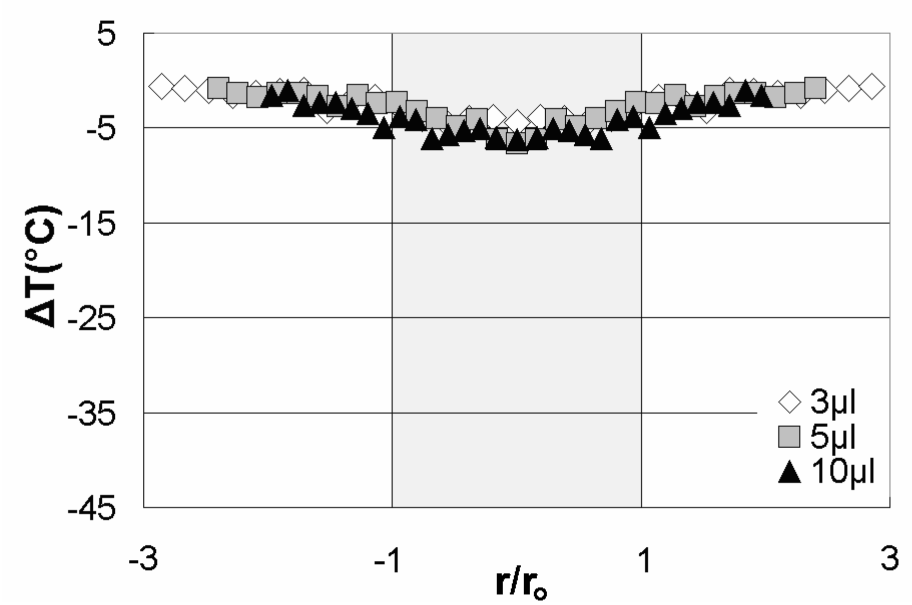

(c) t/τ = 0.5

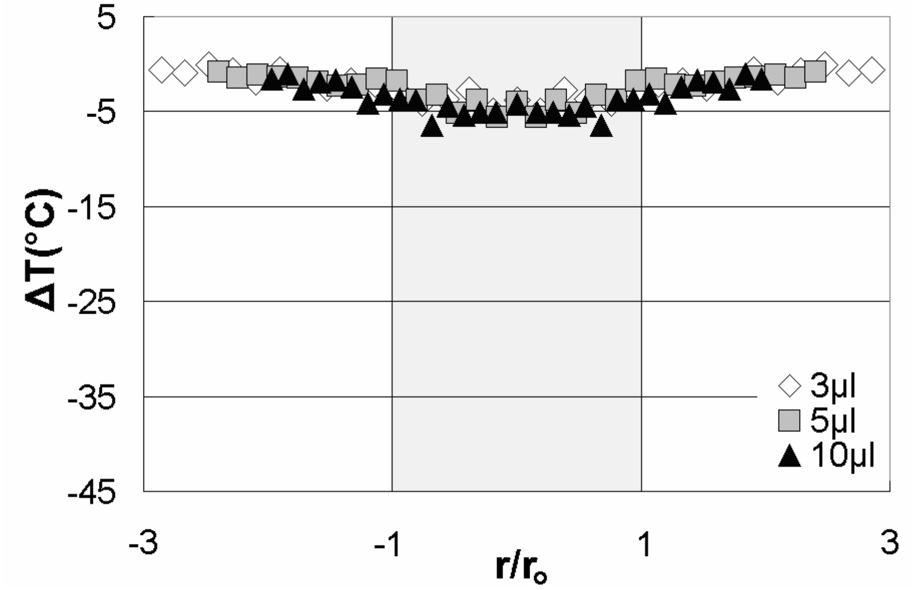

(d) t/τ = 0.9

Fig. 3.17 Continued

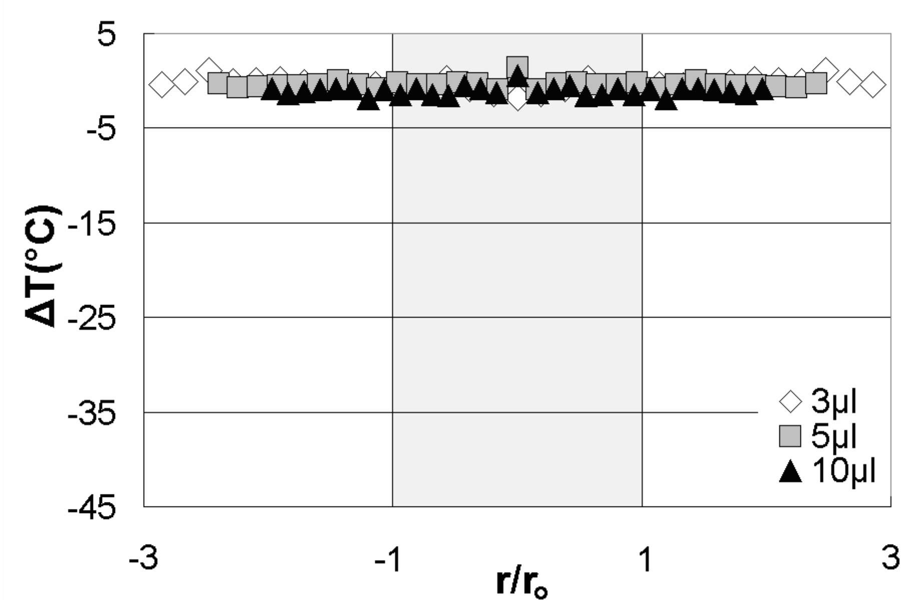

(e) t/τ = 1.1

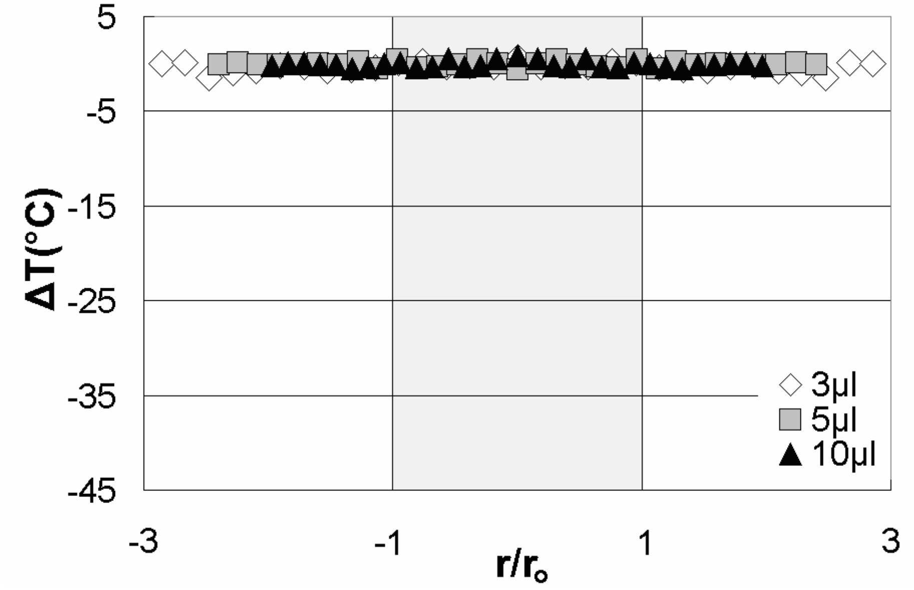

(f) t/τ = 2.0

Fig. 3.17 Continued

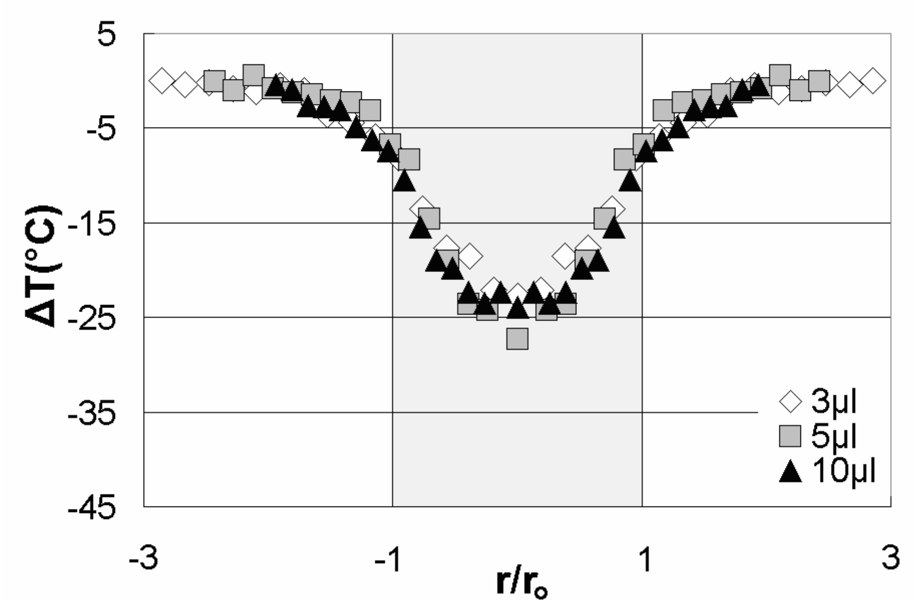

(a) t/τ = 0.01

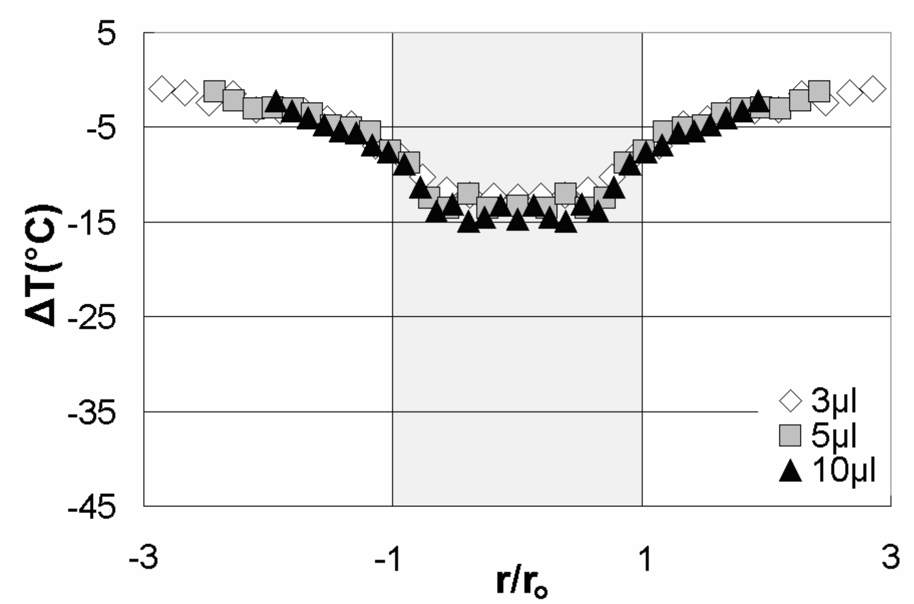

(b) t/τ = 0.1

Fig. 3.18 Tomographic temperature drop profile at T_{dry} = 60°C

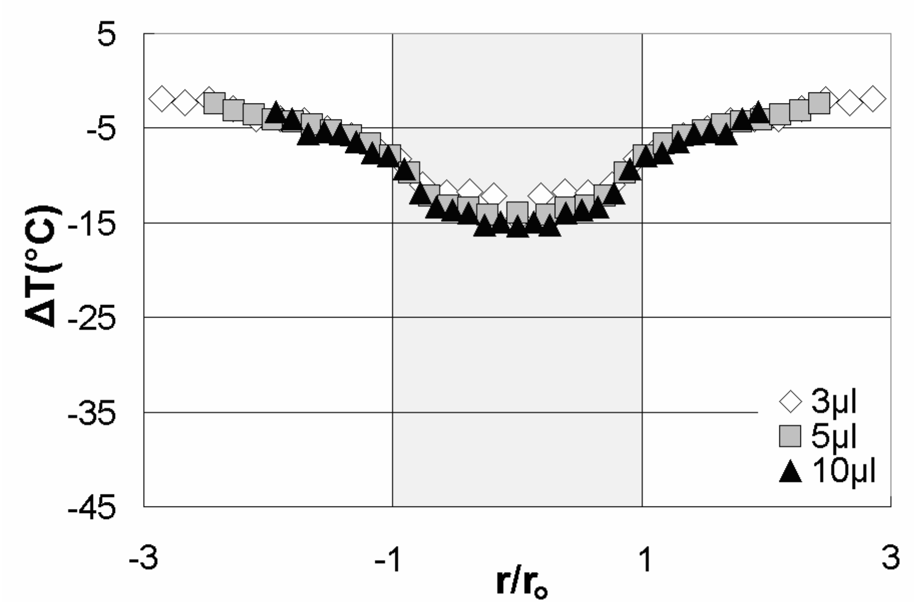

(c) t/τ = 0.5

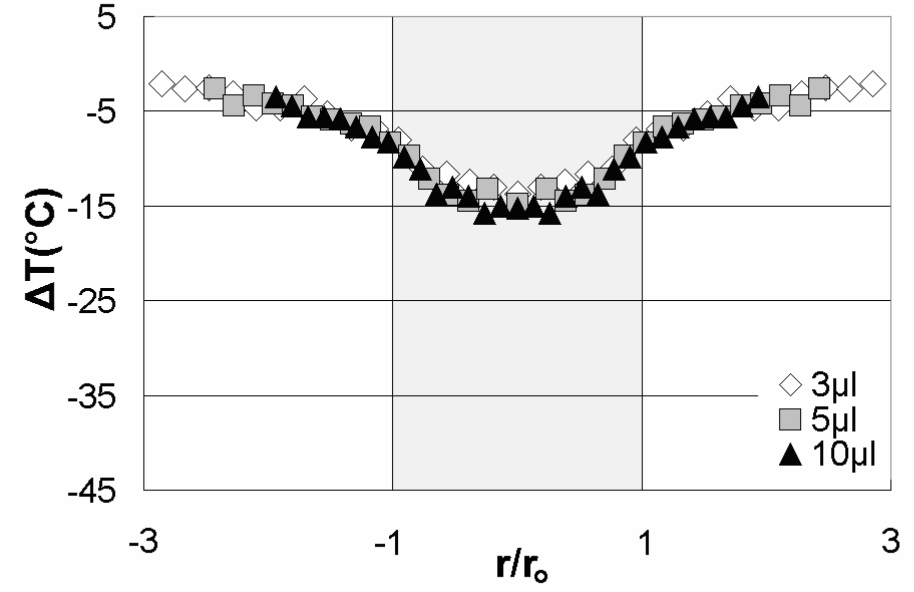

(d) t/τ = 0.9

Fig. 3.18 Continued

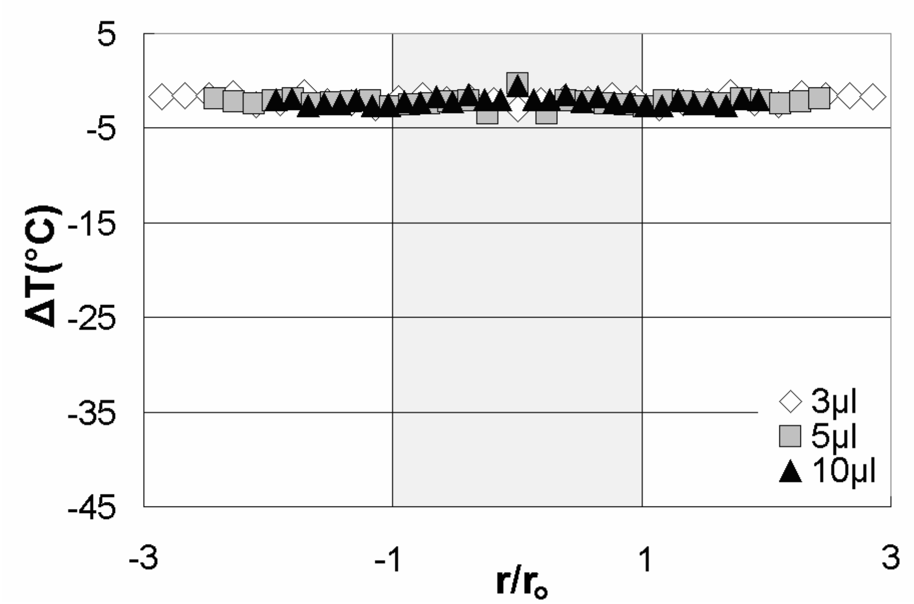

(e) t/τ = 1.1

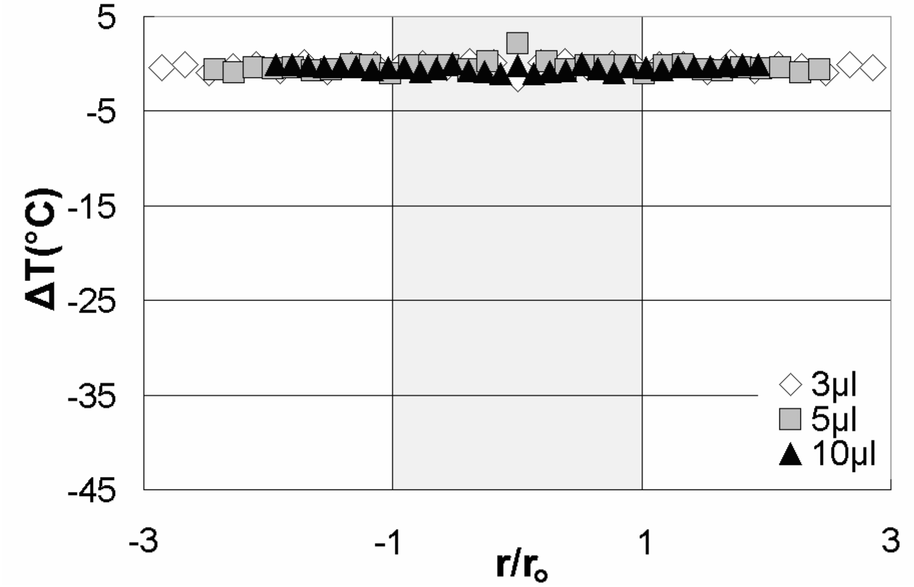

(f) t/τ = 2.0

Fig. 3.18 Continued

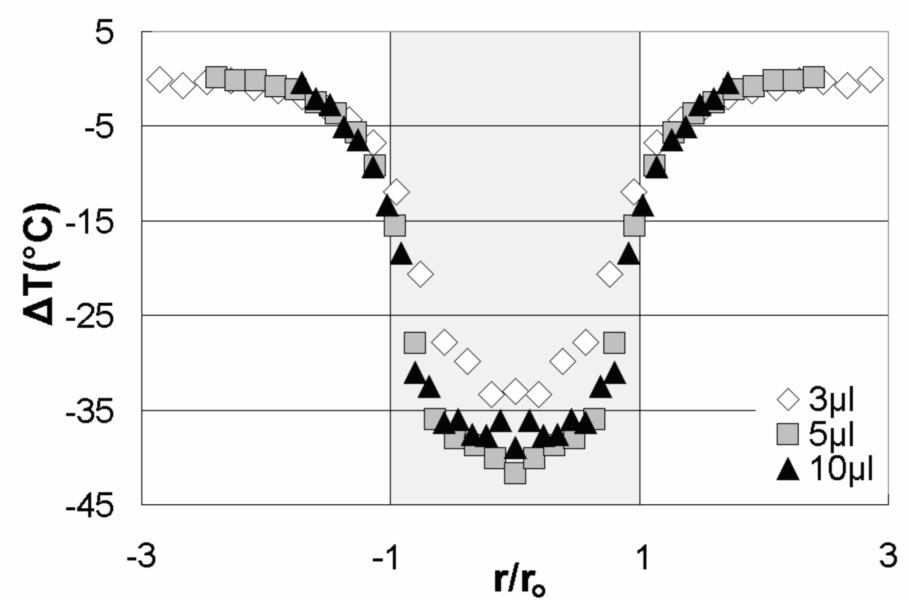

(a) t/τ = 0.01

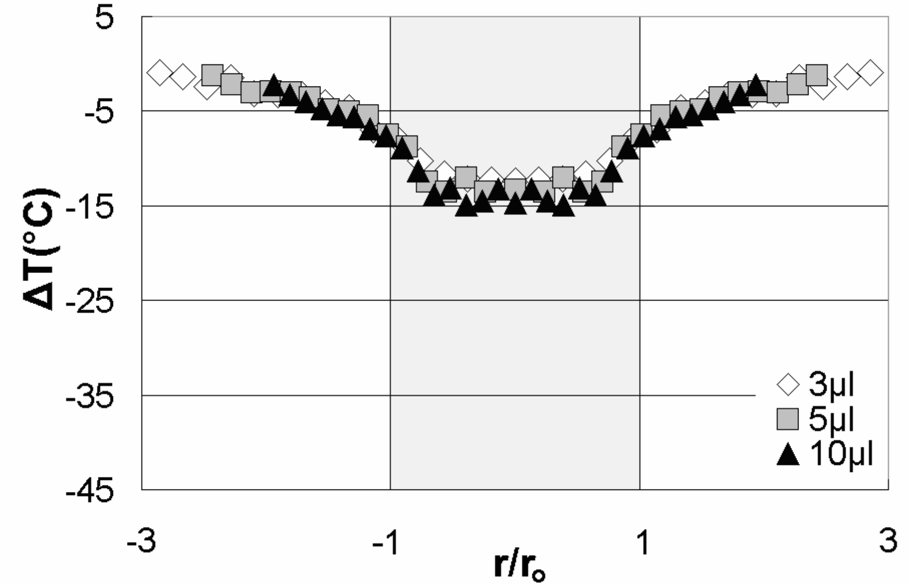

(b) t/τ = 0.1

Fig. 3.19 Tomographic temperature drop profile at T_{dry} = 80°C

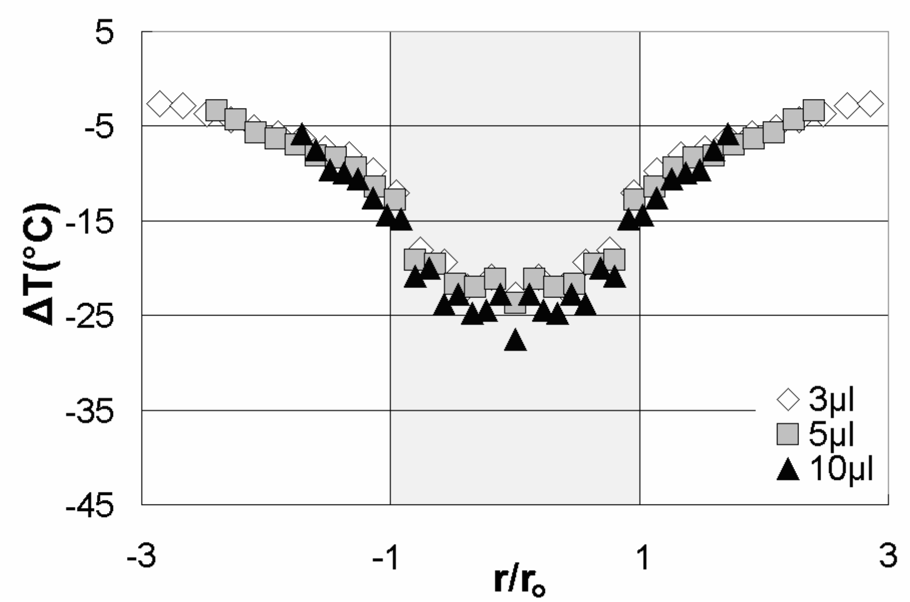

(c) t/τ = 0.5

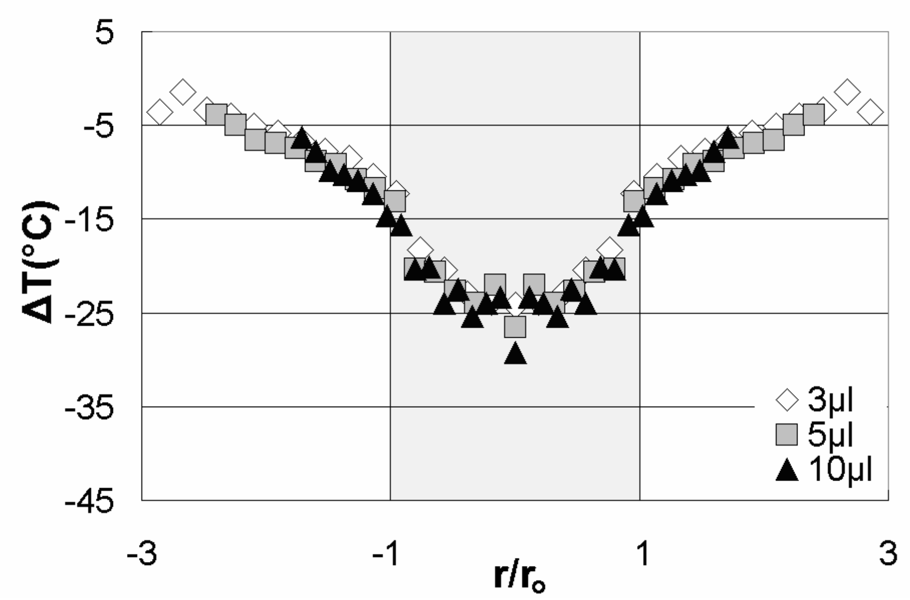

(d) t/τ = 0.9

Fig. 3.19 Continued

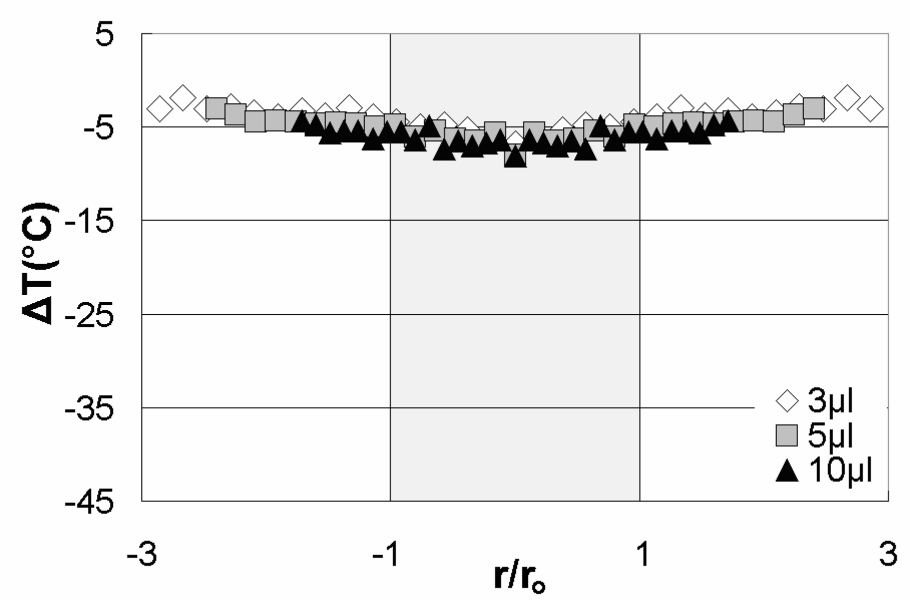

(e) t/τ = 1.1

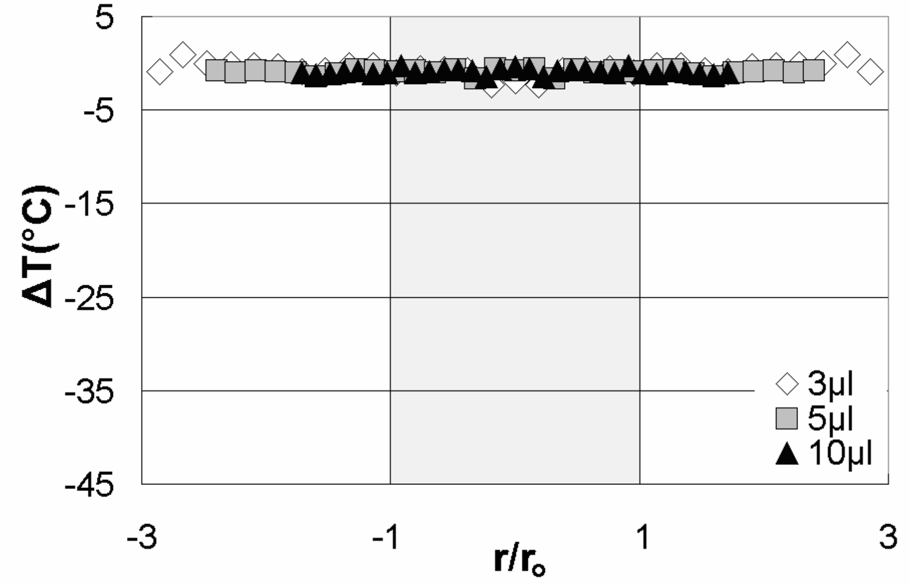

(f) t/τ = 2.0

Fig. 3.19 Continued

Figs. 3.20 to 3.22 show temporal temperature variations measured at the center of the heater surface for all three dry heater temperatures of 40°C, 60°C, and 80°C, and each of Figs. 3.20 to 3.22 show temperature variations for the cases of 3μl, 5μl, and 10μl droplets, respectively. For each of the nine cases shown in Figs. 3.20 to 3.22, a maximum temperature drop is experienced at $t = 0$, and the amount of temperature drop is equivalent to the temperature differential between the dry heater temperature and the droplet temperature before contact of approximately 25°C.

The amounts of temperature drops remain unchanged almost for the entire evaporation period before they recover to the dry heater temperature upon completion of evaporation. Heaters recover to the original dry temperature quickly after evaporation ends.

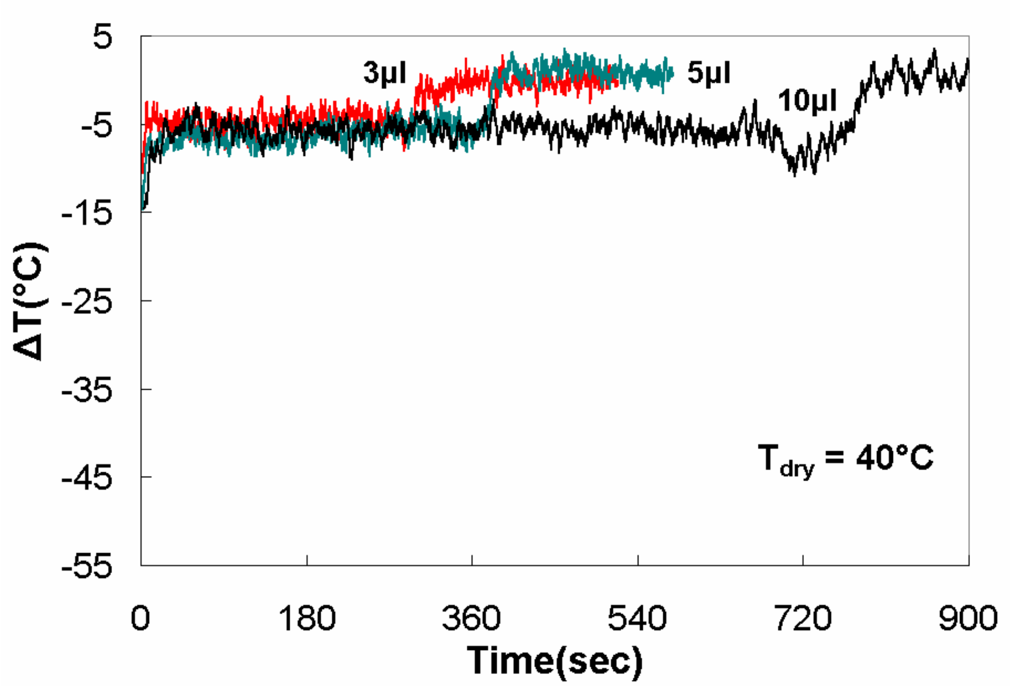

Fig. 3.20 Tomographic temporal temperature drop profile at T_{dry} = 40°C

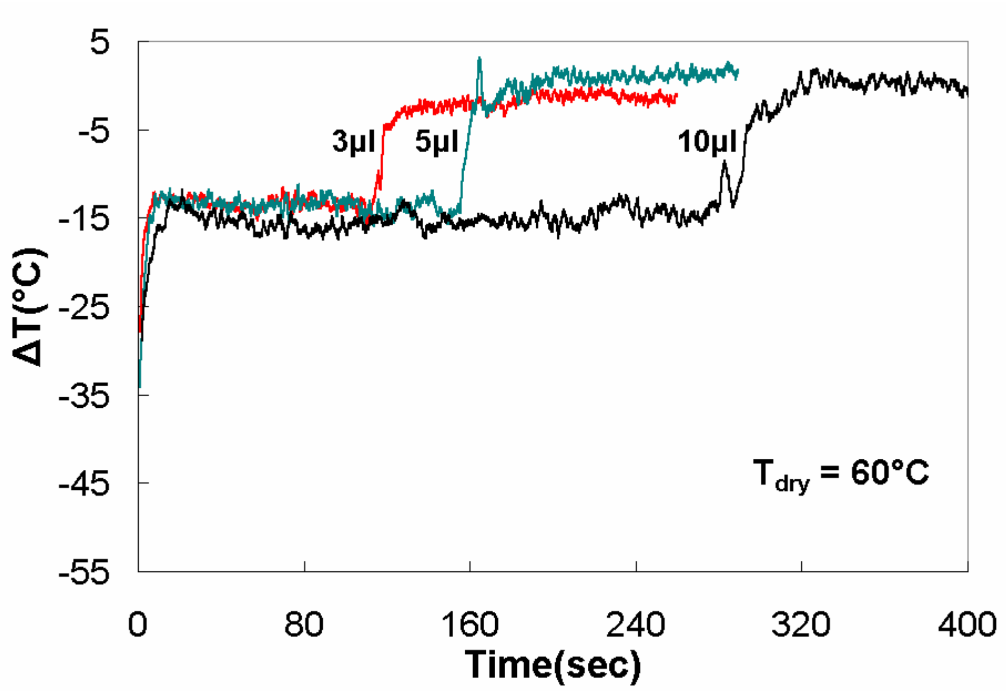

Fig. 3.21 Tomographic temporal temperature drop profile at T_{dry} = 60°C

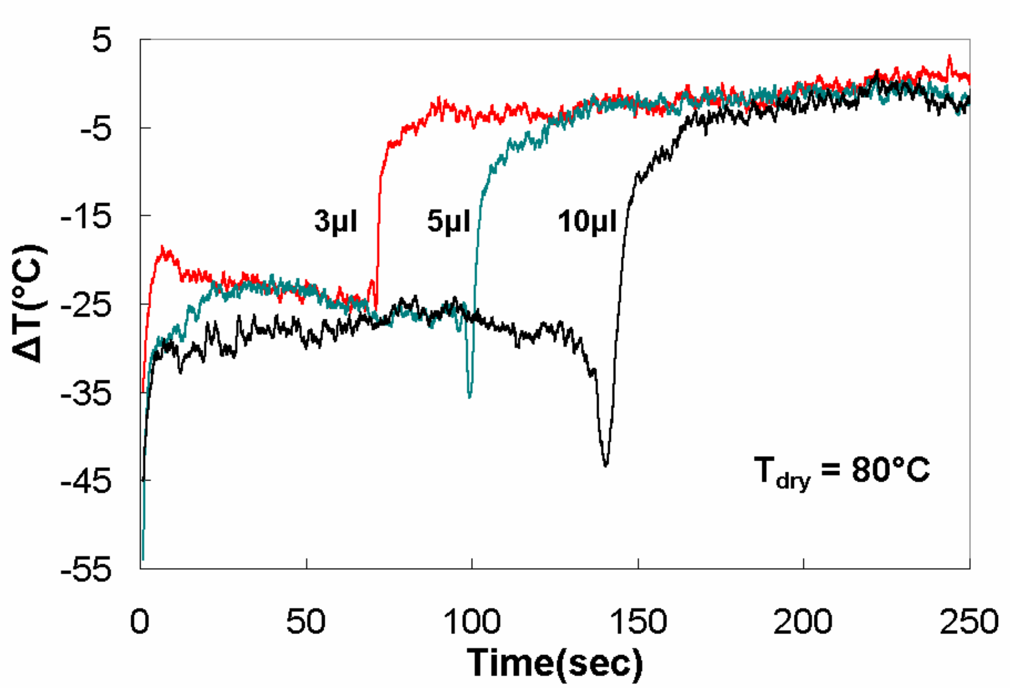

Fig. 3.22 Tomographic temporal temperature drop profile at T_{dry} = 80°C

Note that for the cases of the highest heater temperature (Fig. 3.22) sudden temperature drops are apparent at the final stage of evaporation. It is conjectured that this is attributed to a possible contraction of the relatively thin droplet at the later stage because of the thermocapillary action. In other words, the relatively lower air-water interfacial temperature at the droplet center increases the local surface tension so that the surface flow is induced toward the center from the droplet rim at relatively high temperature and smaller surface tension. Thus, at the final stage of the evaporation, the center region of the water droplet is suddenly thickened based on the droplet contraction, thus the increased local mass enhances the cooling and momentarily lowers the temperature.

Figs. 3.23 to 3.31 show temporal variations of temperature drop at four selected radial locations for the cases of 40°C, 60°C, 80°C dry heater temperature with 3μl, 5μl, 10μl droplets evaporating. The initial temperature drop upon the droplet impact is most pronounced at the center (r/r_o = 0), and the amount of temperature drop diminishes as the droplet boundary is approached ($r/r_o \sim 0.9$). The temperature drop peak exists only inside of the droplet, while outside the droplet boundary the heater surface temperature gradually decreases because of the conduction heat loss to the droplet along the heater surface. The sudden temperature drop near the completion of evaporation, as discussed with Fig. 3.20 to 3.22 above, do not exist other than at the droplet center, and this supports the conjecture of sudden thickening of the central region driven by the thermocapillary phoresis.

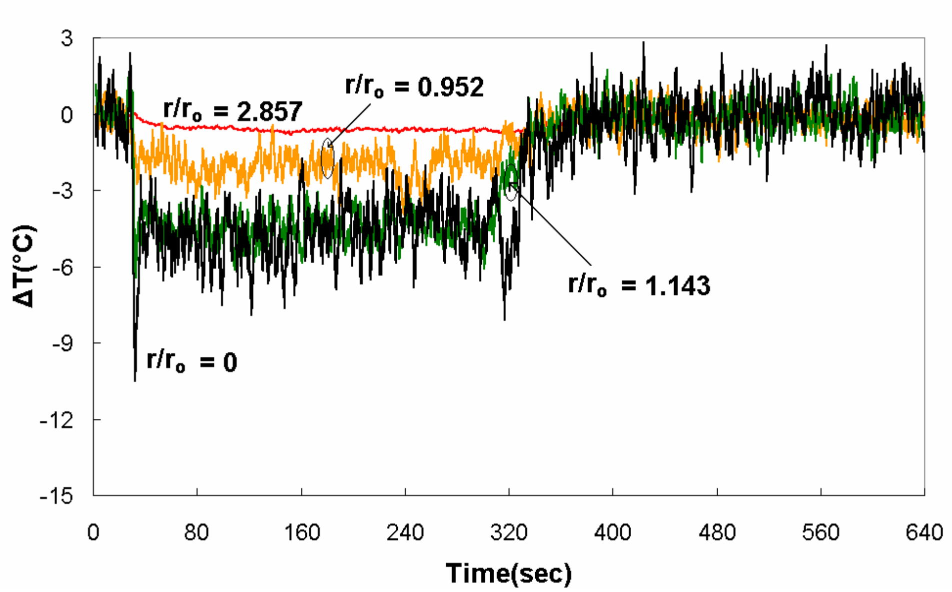

Fig. 3.23 Tomographic temporal temperature drop profile T_{dry} =40°C, 3μl

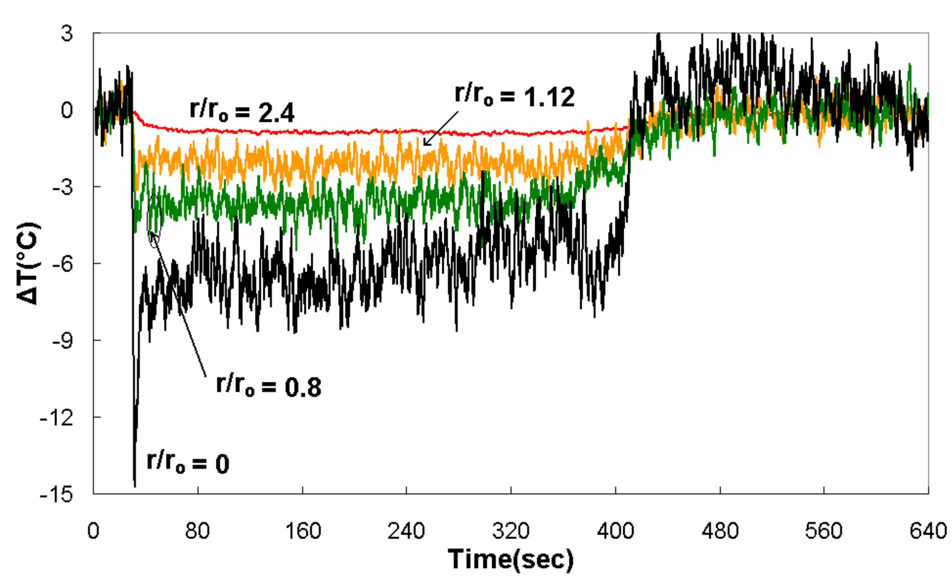

Fig. 3.24 Tomographic temporal temperature drop profile T_{dry} =40°C, 5μl

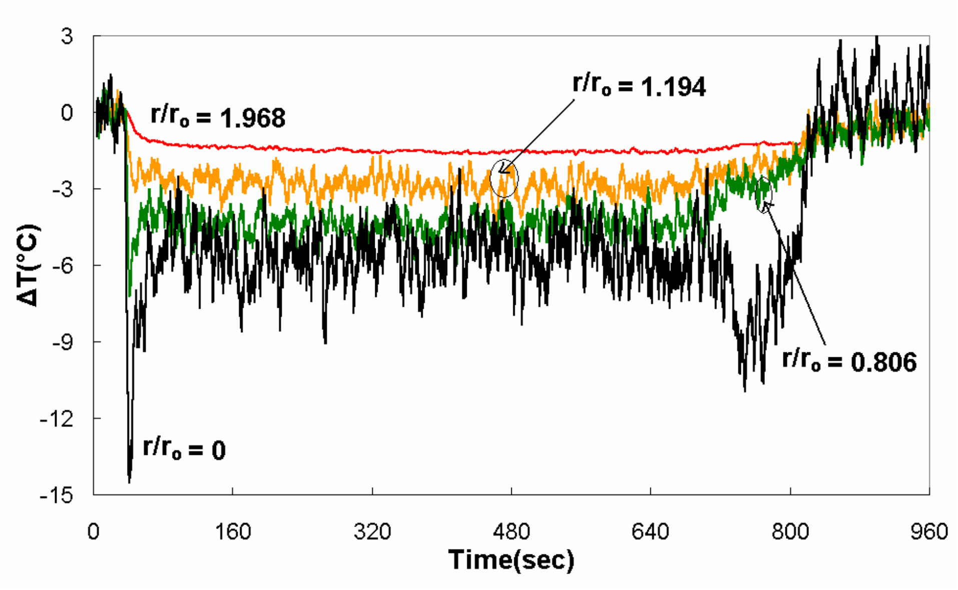

Fig. 3.25 Tomographic temporal temperature drop profile T_{dry} =40°C, 10μl

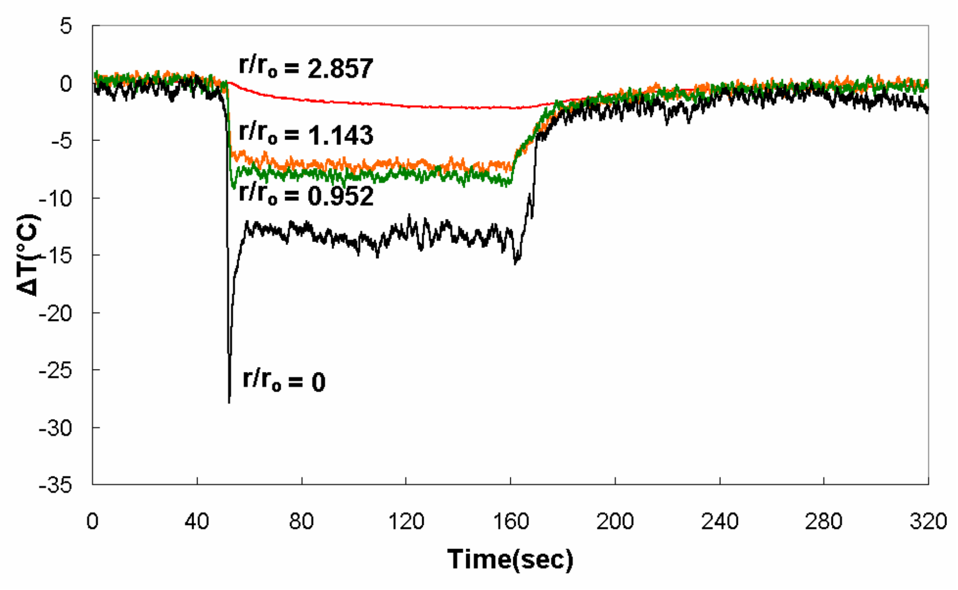

Fig. 3.26 Tomographic temporal temperature drop profile T_{dry} =60°C, 3μl

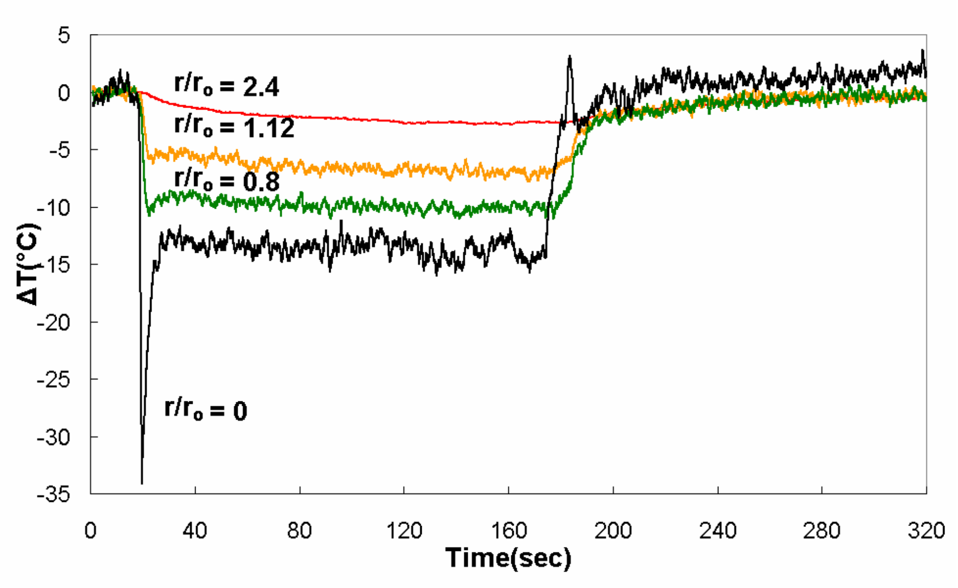

Fig. 3.27 Tomographic temporal temperature drop profile T_{dry} =60°C, 5μl

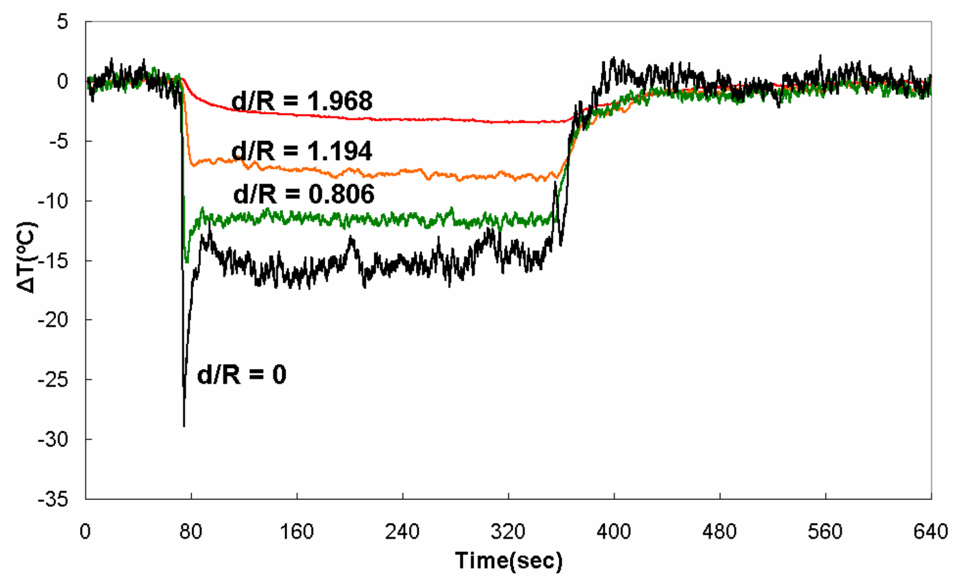

Fig. 3.28 Tomographic temporal temperature drop profile T_{dry} =60°C, 10μl

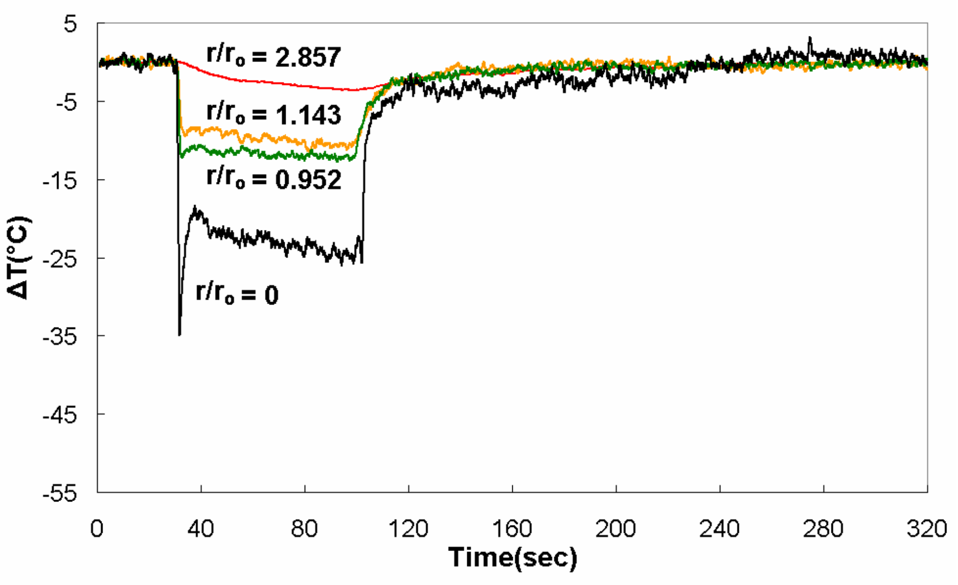

Fig. 3.29 Tomographic temporal temperature drop profile T_{dry} =80°C, 3μl

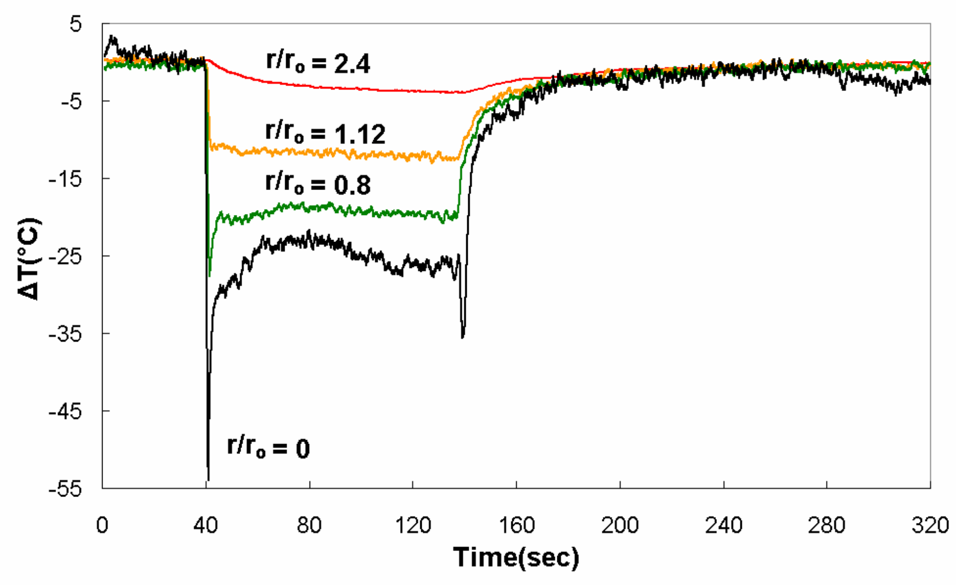

Fig. 3.30 Tomographic temporal temperature drop profile T_{dry} =80°C, 5μl

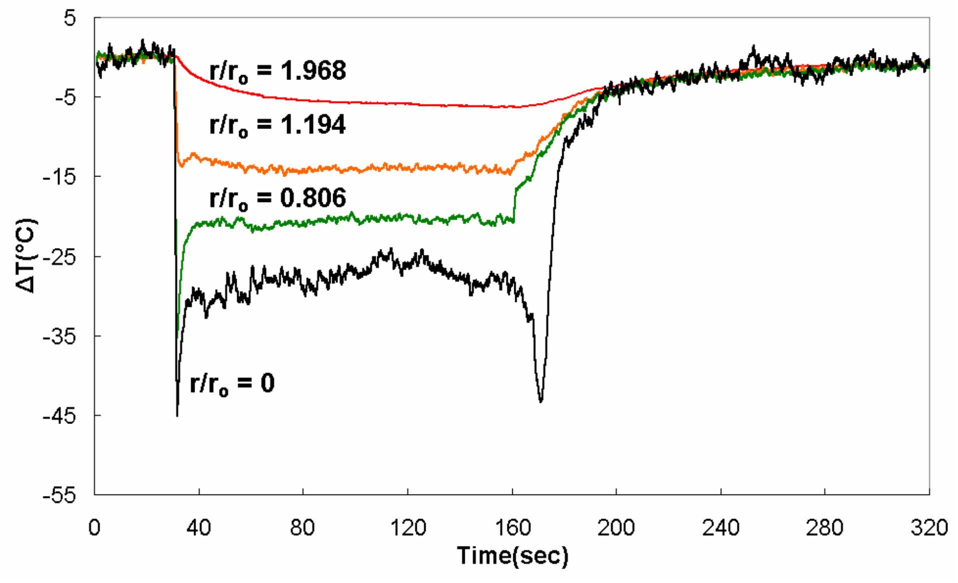

Fig. 3.31 Tomographic temporal temperature drop profile T_{dry} =80°C, 10μl

Also, the temperature recovery to the dry heater level starts earlier and faster at r/r_o ~ 0.90, than at the center, which also manifests that the dry-off starts from the boundary and finishes towards the center. Note that the highly sensitive and fluctuating data at the center represents the unstationary nature of evaporative heat and mass transfer at the droplet center, quite possibly occurring because of the unsteady convectional flow inside the droplet. The fluctuation magnitudes diminish with increasing radius, and the fluctuation disappears farther away from the droplet boundary that is not affected by the unsteadiness of droplet evaporation.

3.6 Tomographic deconvolution of line-averaged raw heat flux data

The heat flux or heater power per unit area can be calculated from Eq. (3.6) by dividing this equation into the unit area. While the heater resistance varies linearly with the heater temperature (Eq. 2.1), it is apparent that the heater power varies non-linearly with the heater temperature. However, since the resistance of the voltage divider is 6.4 times larger than the nominal resistance of the line heaters, the former dominates the latter in the denominator of Eq. (3.6). Neglecting the heater resistance contribution in the denominator, the heat flux can be regarded linearly varying with heater resistance, as well as measured heater temperature. Henceforth, the spatial and temporal heat flux distributions must closely resemble the corresponding temperature profiles shown in tomographic deconvoluted spatial or temporal temperature distribution graphs.

With Eq. (3.6), and by applying constant voltage (3V) and constant voltage divider resistance (51 Ω), we simply changed the resistance of the heater from 6.3 Ω to 7.8 Ω for the numeric calculation. As a result, following Fig. 3.32, a resistance and heat flux relation was made. The blue solid line is the relation of heater resistance and heat flux. This is a calculated result, and the actual heater heat fluxes are the same if the microheater has the same resistance as shown below.

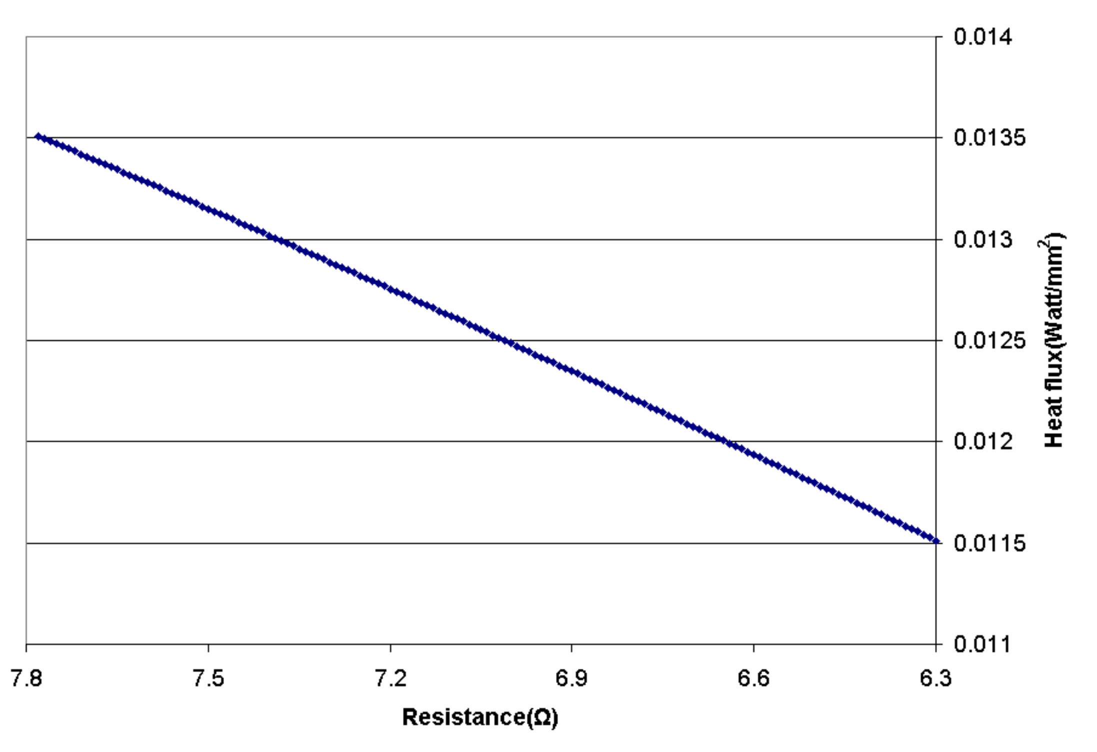

Fig. 3.32 Resistance-heat flux relation for constant voltage microheater

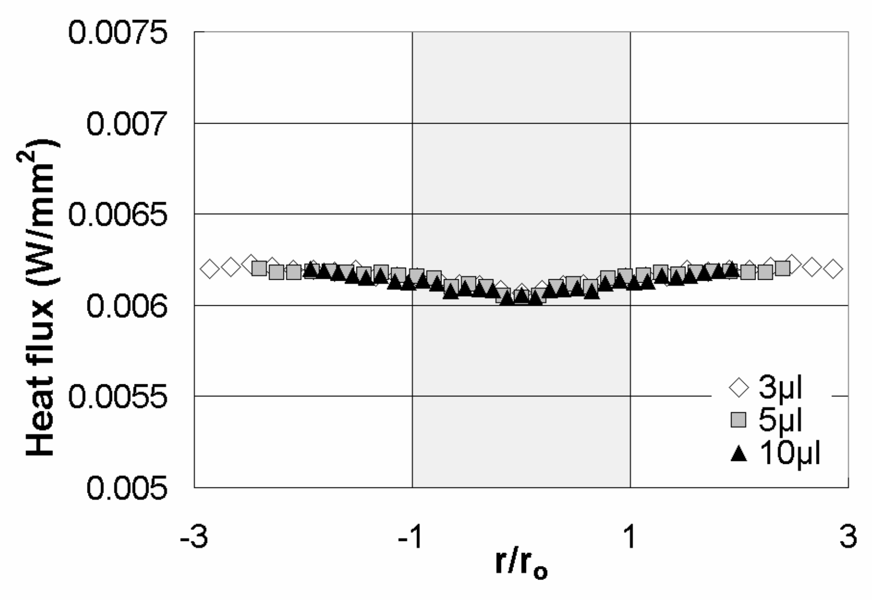

(a) t/τ = 0.01

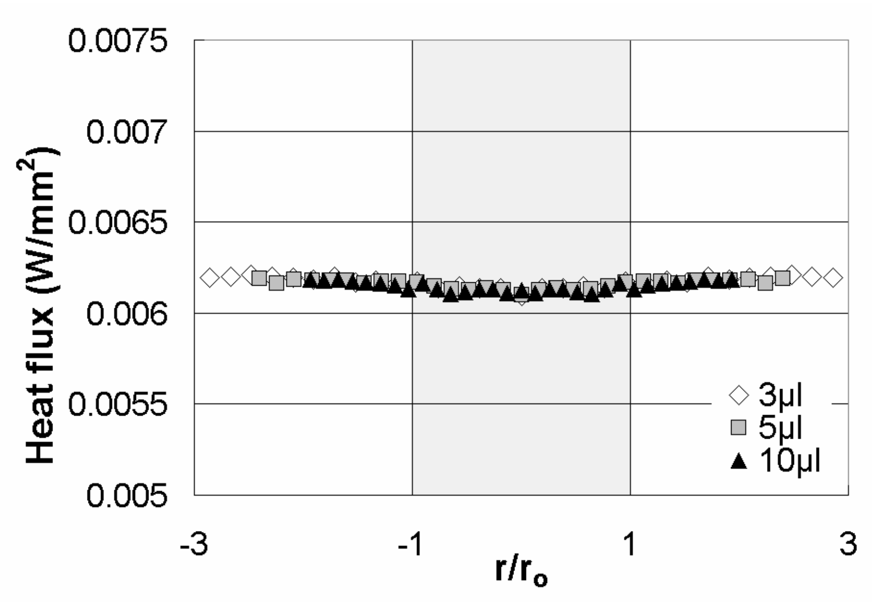

(b) t/τ = 0.1

Fig. 3.33 Tomographic heat flux drop profile at T_{dry} = 40°C

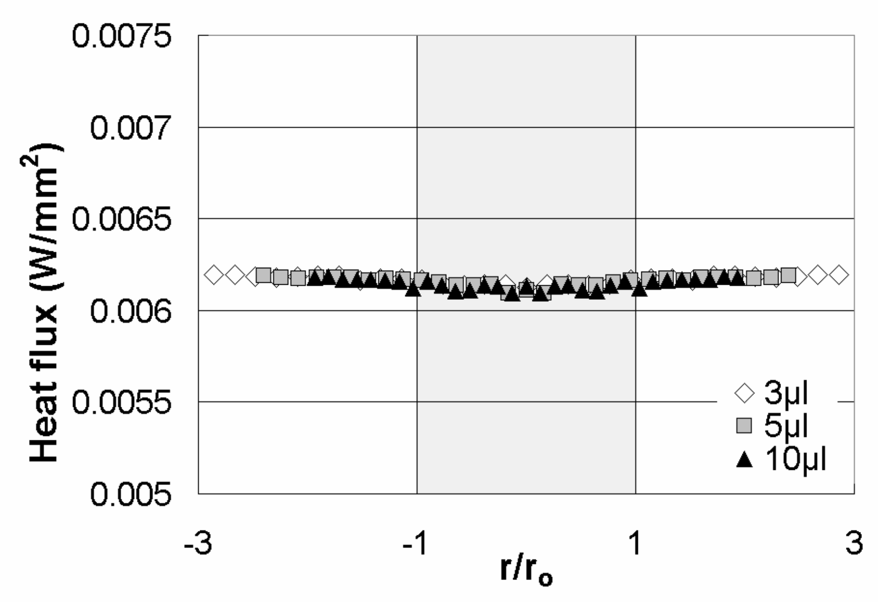

(c) t/τ = 0.5

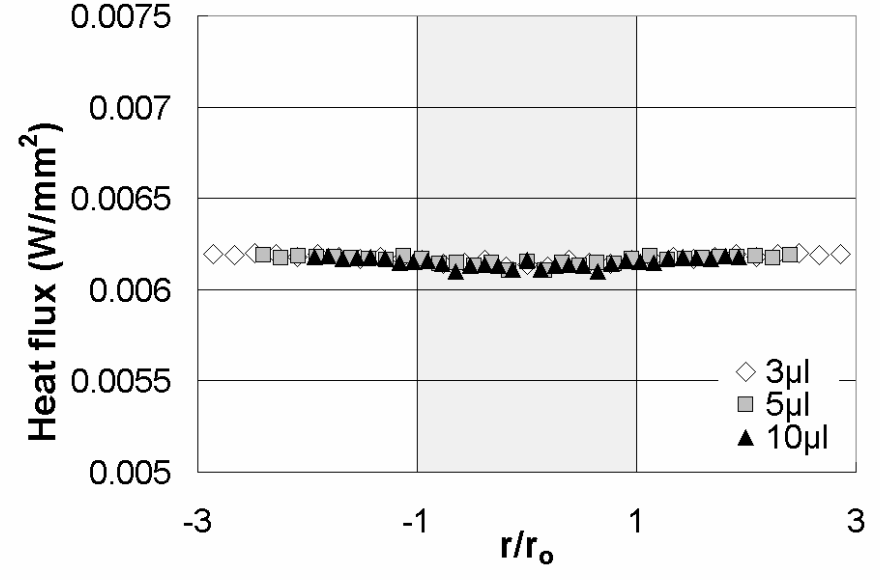

(d) t/τ = 0.9

Fig. 3.33 Continued

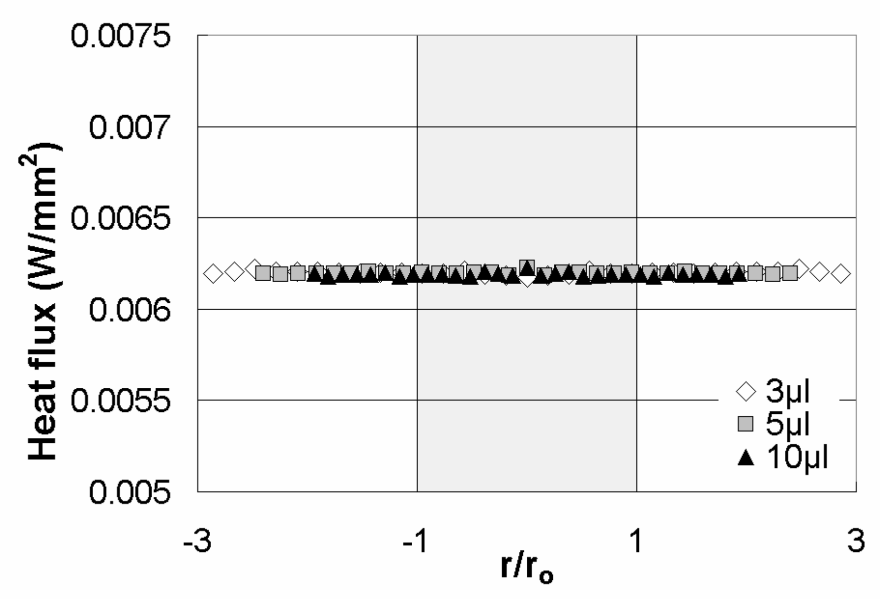

(e) t/τ = 1.1

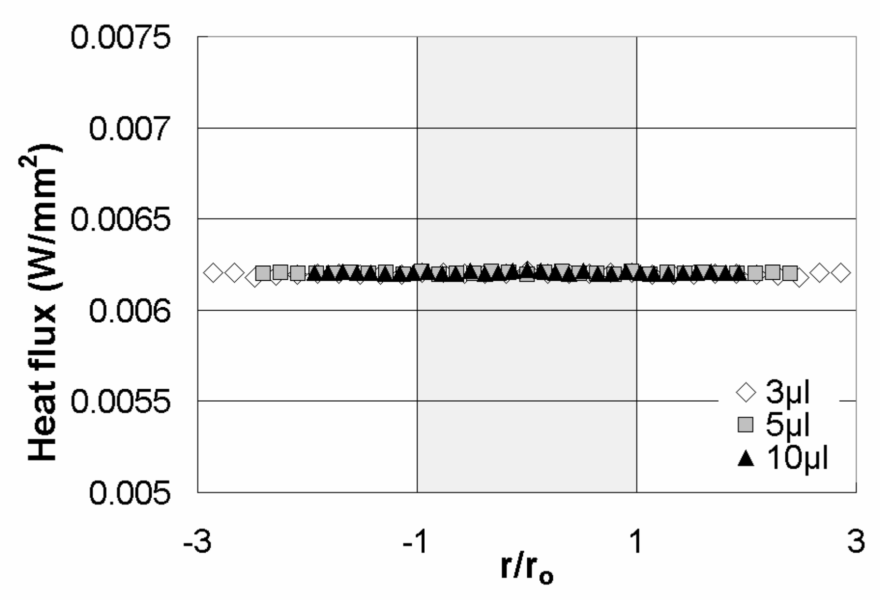

(f) t/τ = 2.0

Fig. 3.33 Continued

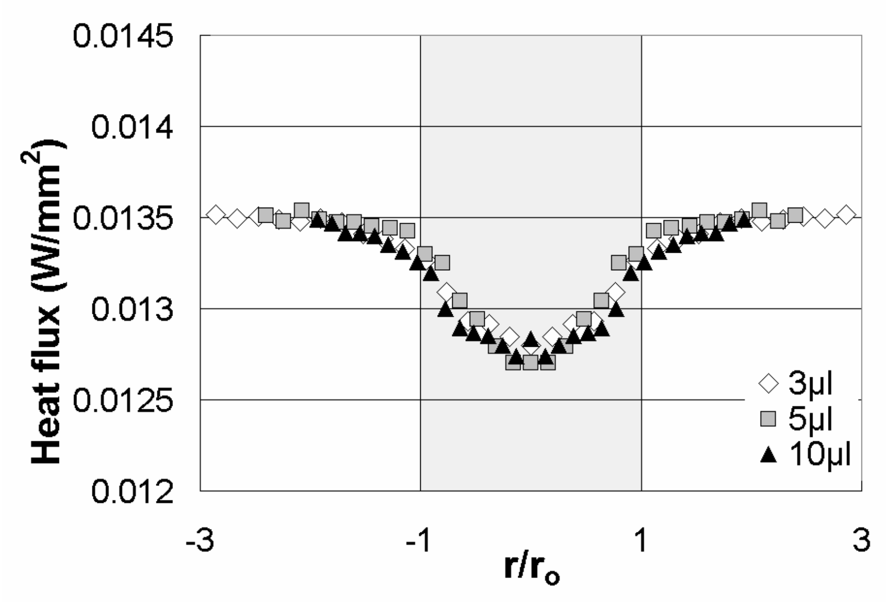

(a) t/τ = 0.01

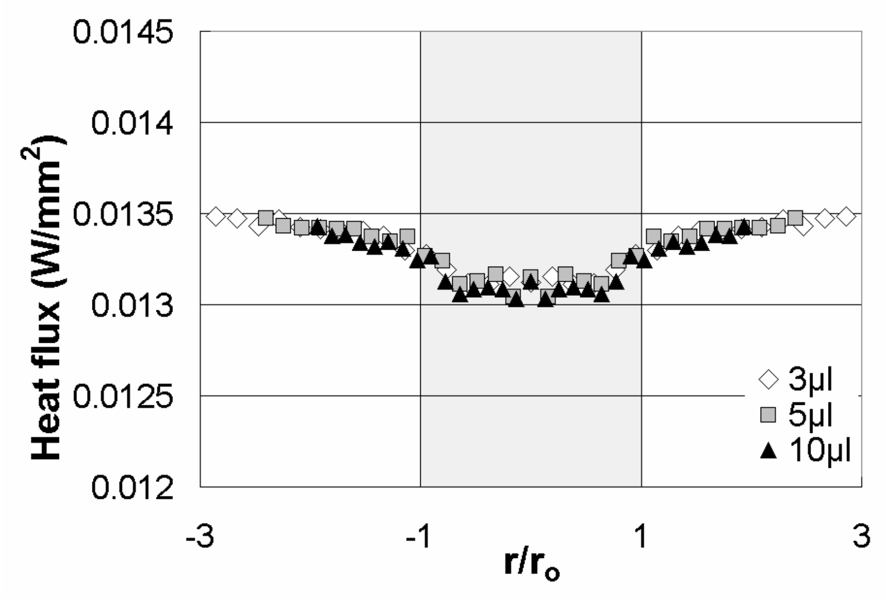

(b) t/τ = 0.1

Fig. 3.34 Tomographic heat flux drop profile at T_{dry} = 60°C

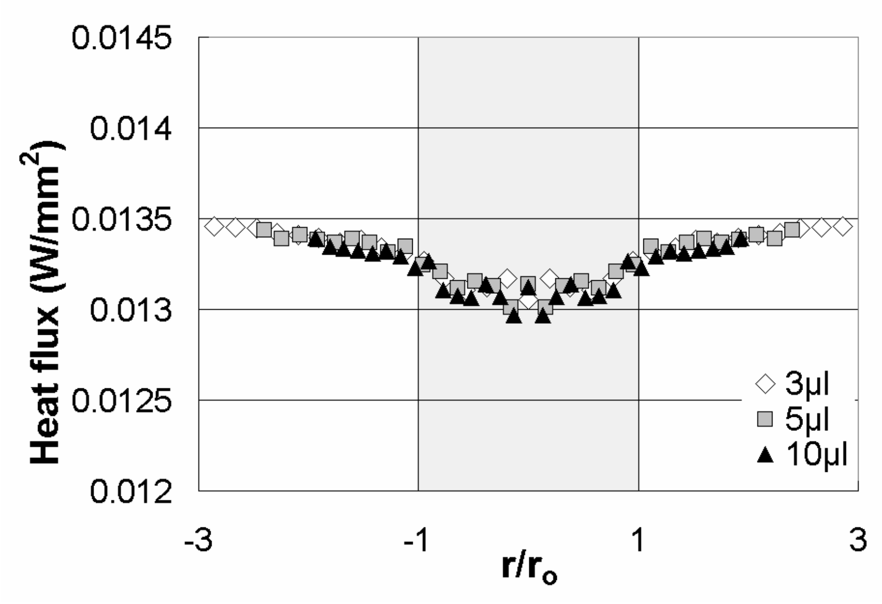

(c) t/τ = 0.5

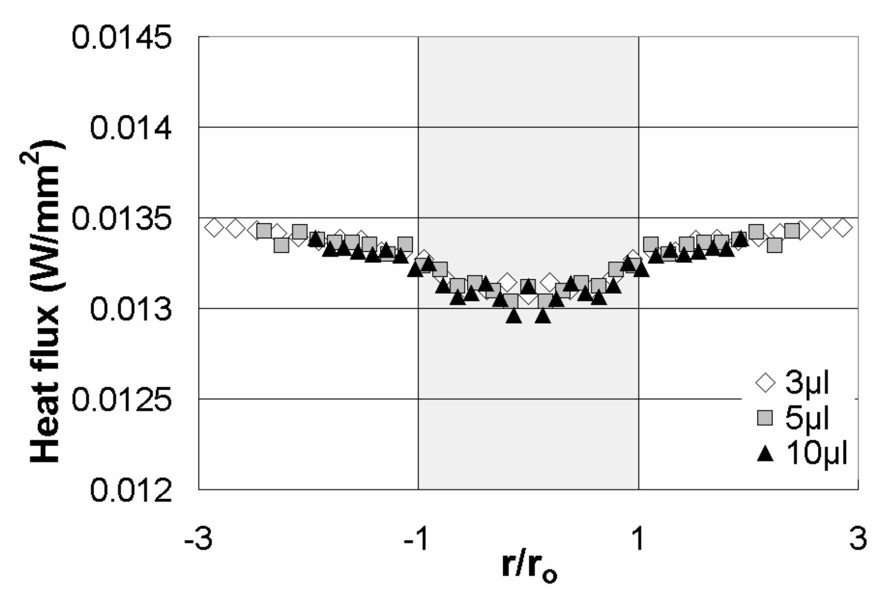

(d) t/τ = 0.9

Fig. 3.34 Continued

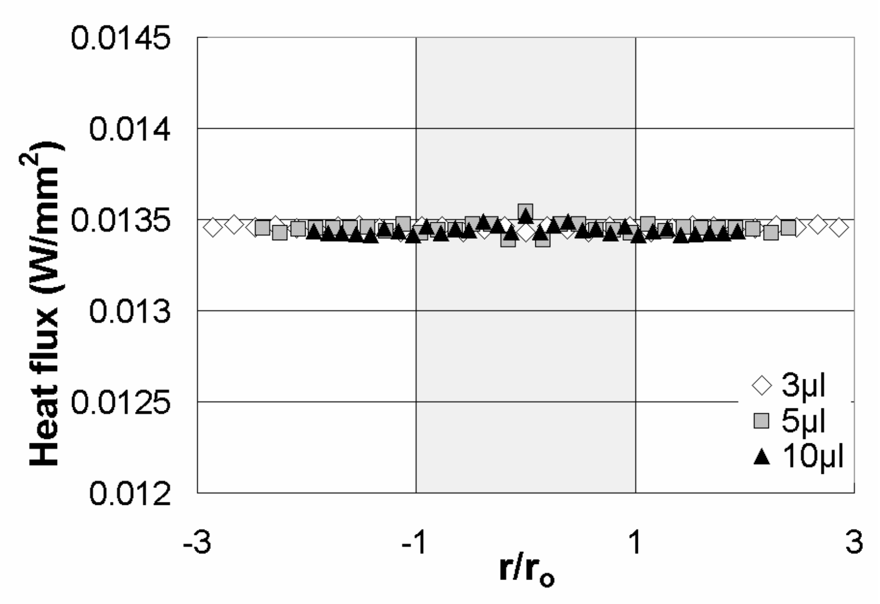

(e) t/τ = 1.1

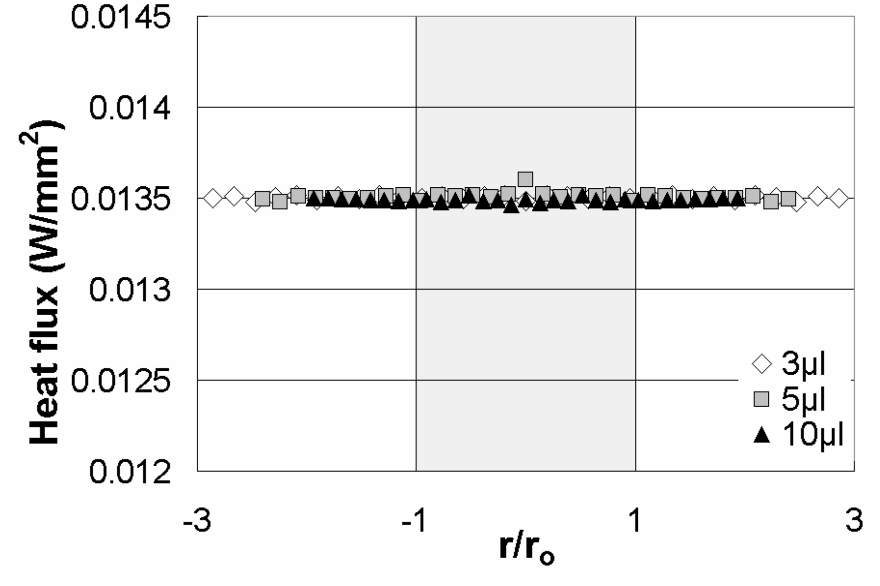

(f) t/τ = 2.0

Fig. 3.34 Continued

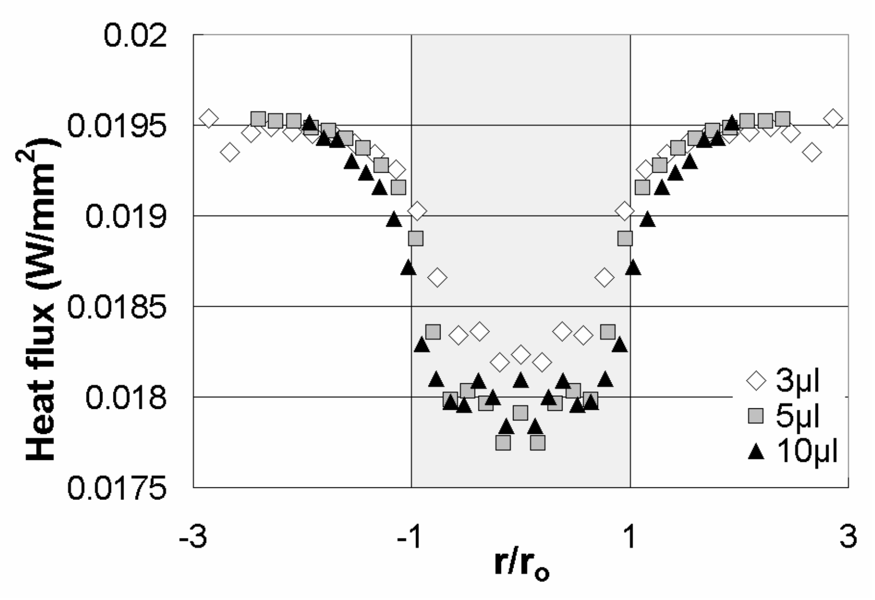

(a) t/τ = 0.01

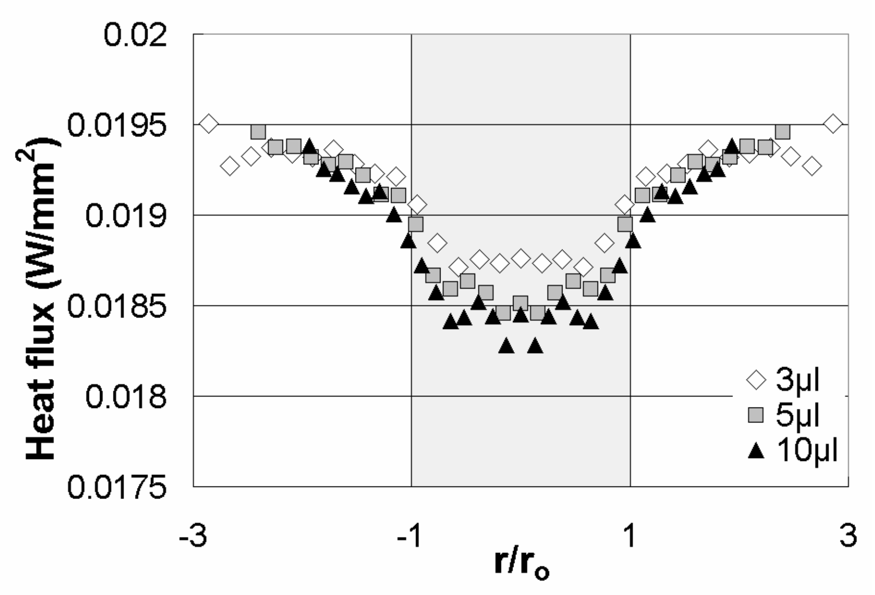

(b) t/τ = 0.1

Fig. 3.35 Tomographic heat flux drop profile at T_{dry} = 80°C

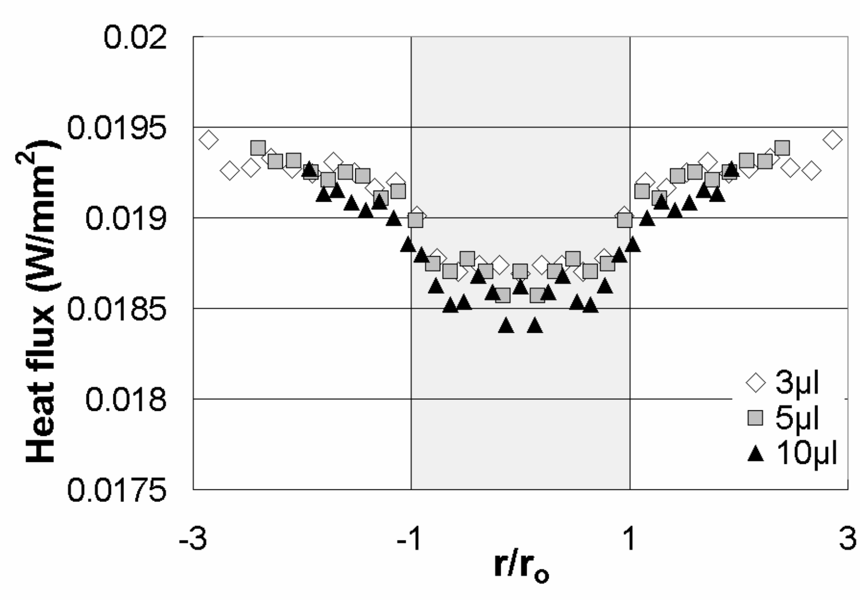

(c) t/τ = 0.5

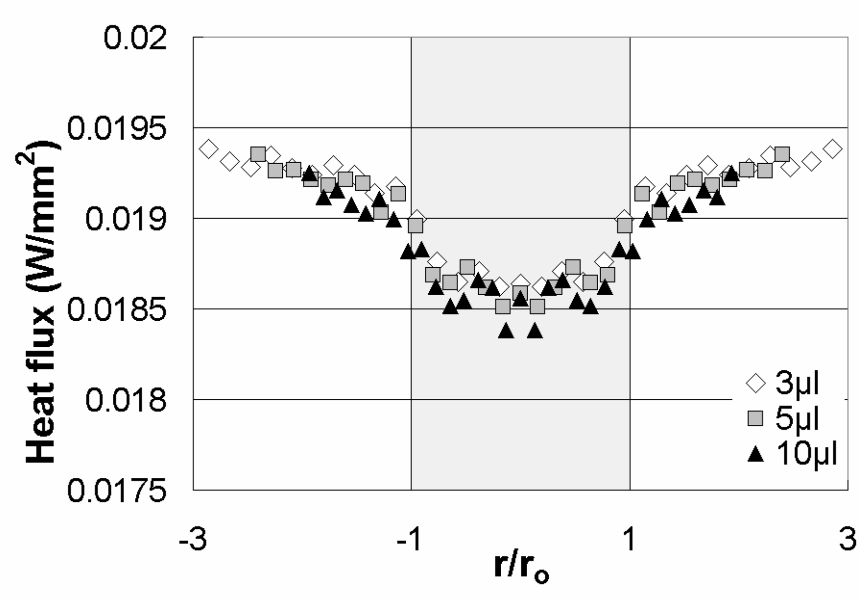

(d) t/τ = 0.9

Fig. 3.35 Continued

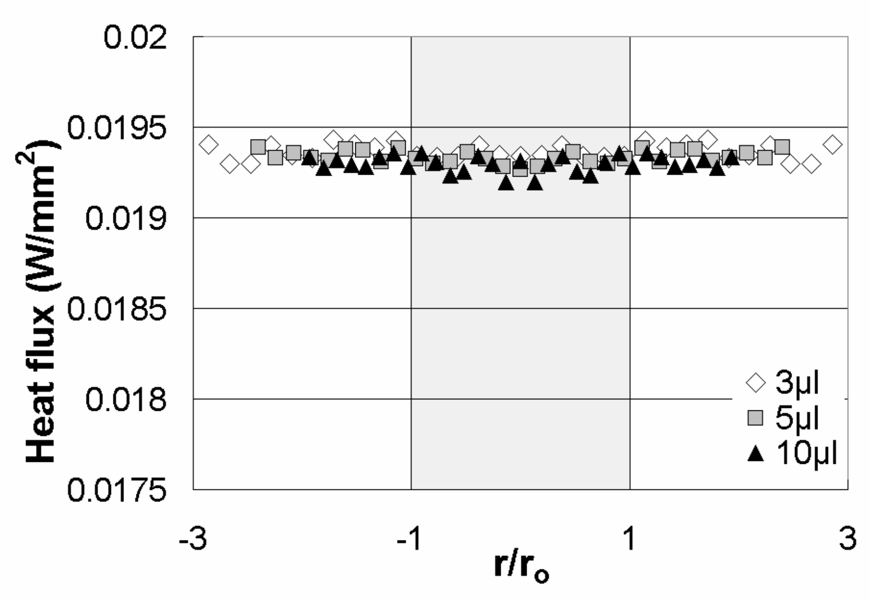

(e) t/τ = 1.1

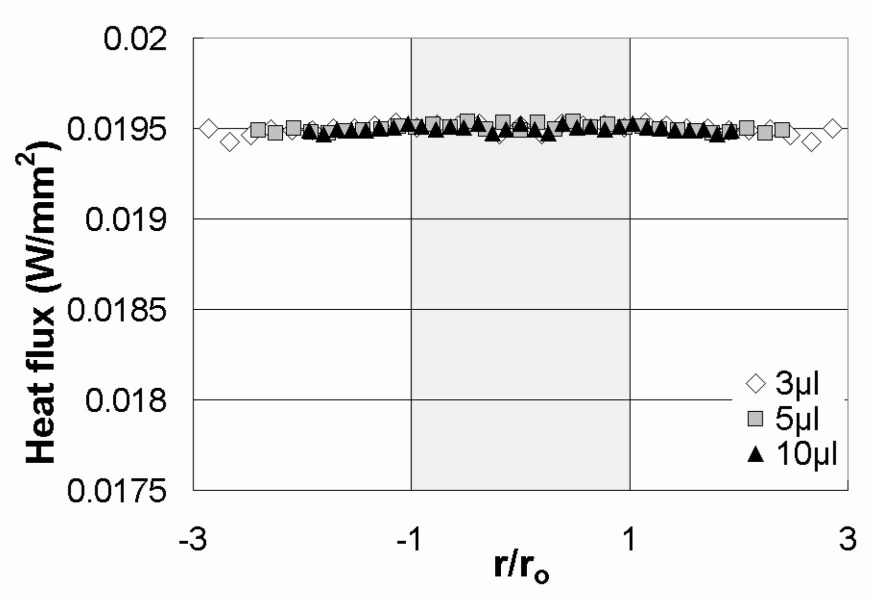

(f) t/τ = 2.0

Fig. 3.35 Continued

Figs. 3.33-3.35 show temporal development of tomographically deconvoluted heat flux profiles for 3μl, 5μl, and 10μl droplets for the cases of 40°C, 60°C, 80°C dry heater temperature.

When the radial distance is normalized by the wet radius of each droplet, all three profiles for the three droplets collapse together showing similar development for practically the entire test period. Upon contact, the largest heat flux drop resulted because of the instantaneous maximum cooling rate (Figs. 3.33-35-a). Heat flux remains nearly unchanged during the evaporation in which a latent heat transfer process at a constant heat flux prevails (Figs. 3.33-3.35-b to d). Then heat flux returns to the dry heater heat flux after completion of evaporation (Figs. 3.33-3.35-e), and fully recovers to it in $t = 2.0\tau$ (Figs. 3.33-3.35-f).

Figs. 3.36 to 3.38 show temporal heat flux variations measured at the center of the heater surface for all three dry heater temperatures of 40°C, 60°C, and 80°C, and each of Figs. 3.36 to 3.38, respectively, show heat flux variations for the cases of 3μl, 5μl, and 10μl droplets. For each of the nine cases shown in Figs. 3.36 to 3.38, a maximum heat flux drop is experienced at $t = 0$. The amount of heat flux drops remain unchanged almost for the entire evaporation period before they recover to the dry heater heat flux upon completion of evaporation. Heaters recover to the original dry heat flux quickly after evaporation ends.

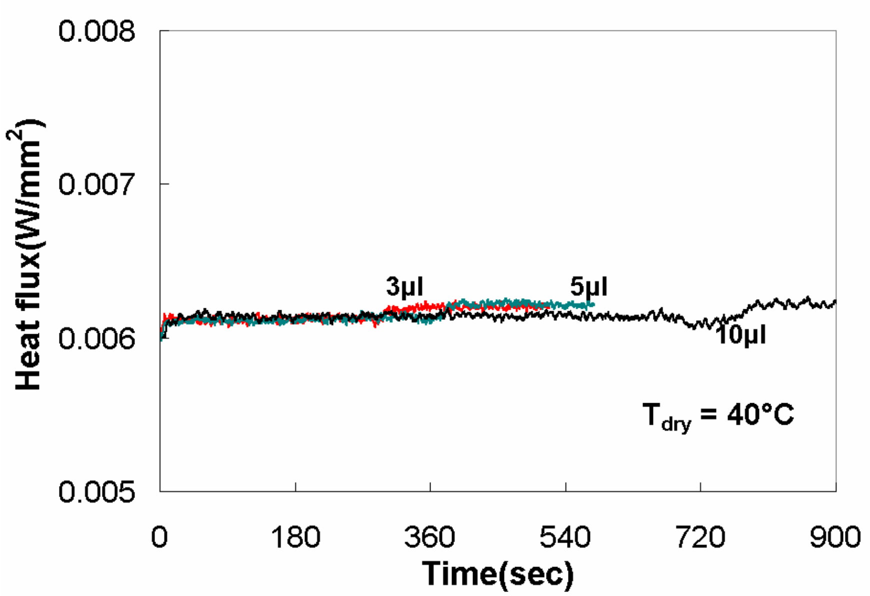

Fig. 3.36 Tomographic temporal heat flux drop profile at T_{dry} = 40°C

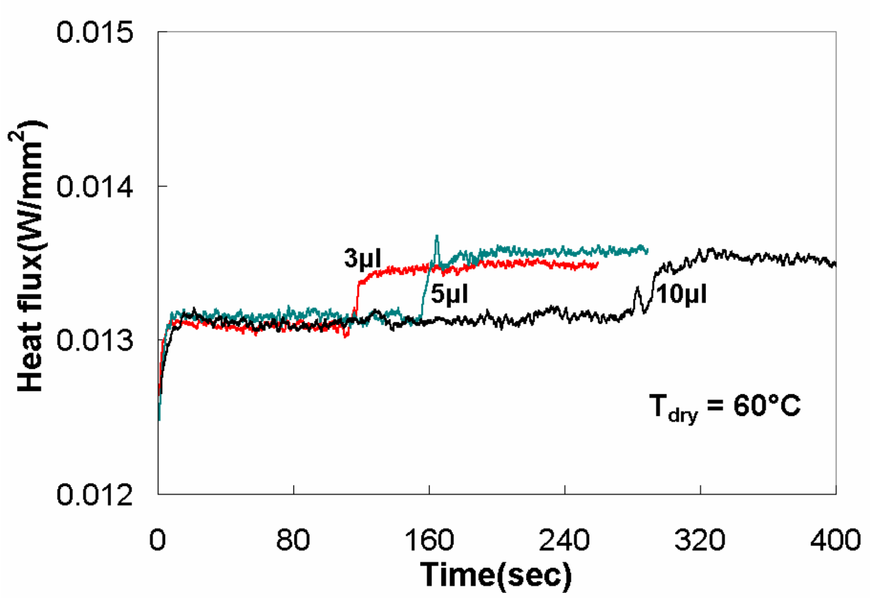

Fig. 3.37 Tomographic temporal heat flux drop profile at T_{dry} = 60°C

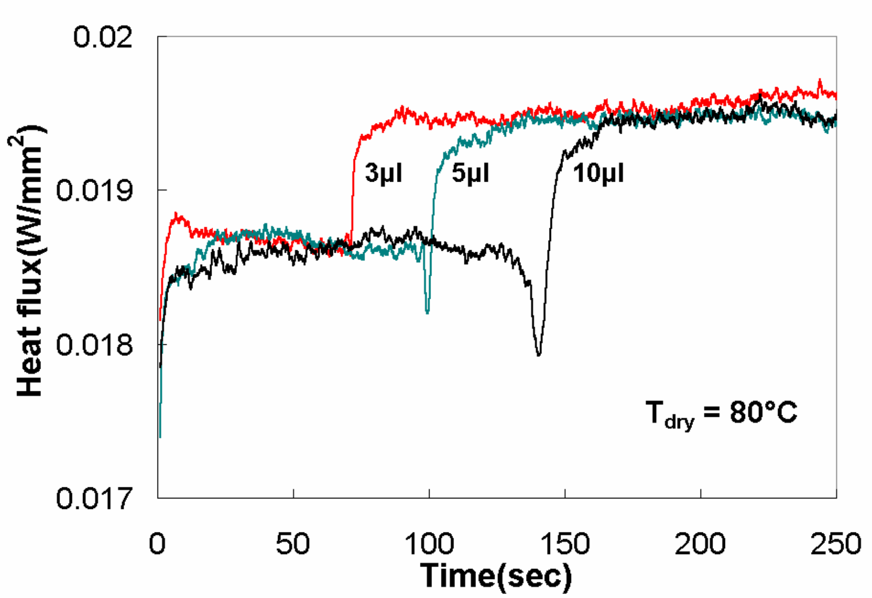

Fig. 3.38 Tomographic temporal heat flux drop profile at T_{dry} = 80°C

Note that for the cases of the highest heater temperature, (Fig. 3.38) sudden heat flux drops are apparent at the final stage of evaporation. It is conjectured that this is attributed to a possible contraction of the relatively thin droplet at the later stage because of the thermocapillary action. In other words, the relatively lower air-water interfacial temperature at the droplet center increases the local surface tension so that the surface flow is induced toward the center from the droplet rim at relatively high temperatures and smaller surface tension. Thus, at the final stage of the evaporation, the center region of the water droplet is suddenly thickened based on the droplet contraction, so that the increased local mass enhances the cooling and momentarily lowers the heat flux.

Figs. 3.39 to 3.47 show temporal variations of heat flux drop at four selected radial locations for the cases of 40°C, 60°C, 80°C dry heater temperature with 3μl, 5μl, 10μl droplet evaporating. Upon droplet impact, the initial heat flux drop is most pronounced at the center ($r/r_o = 0$), and the amount of heat flux drop diminishes as the droplet boundary is approached ($r/r_o \sim 0.9$). The heat flux drop peak exists only inside of the droplet, while outside the droplet boundary the heater surface heat flux gradually decreases because of the conduction heat loss to the droplet along the heater surface. The sudden heat flux drop near the completion of evaporation, as discussed with Figs. 3.36 to 3.38 above, do not exist other than at the droplet center, and this supports the conjecture of sudden thickening of the central region driven by the thermocapillary phoresis.

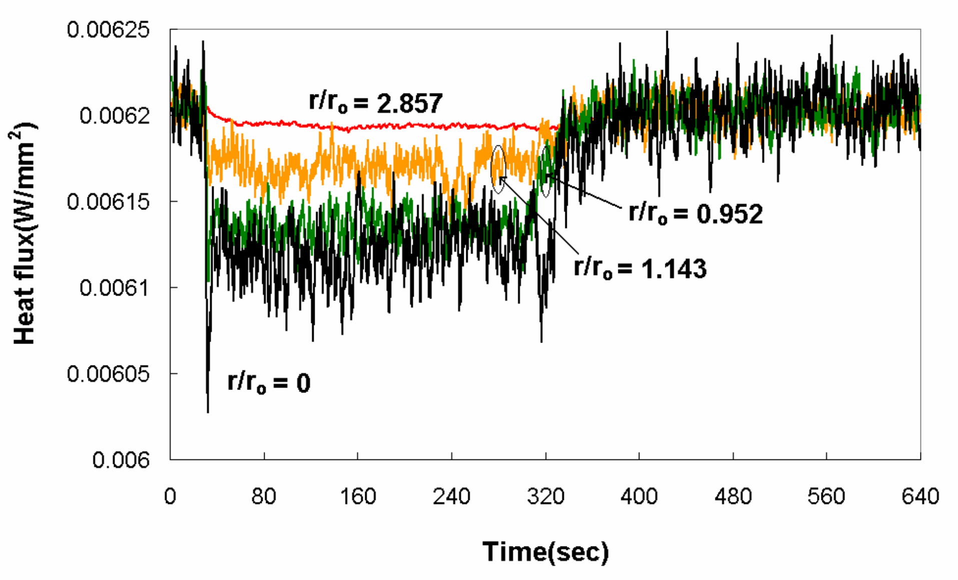

Fig. 3.39 Tomographic temporal heat flux drop profile T_{dry} =40°C, 3μl

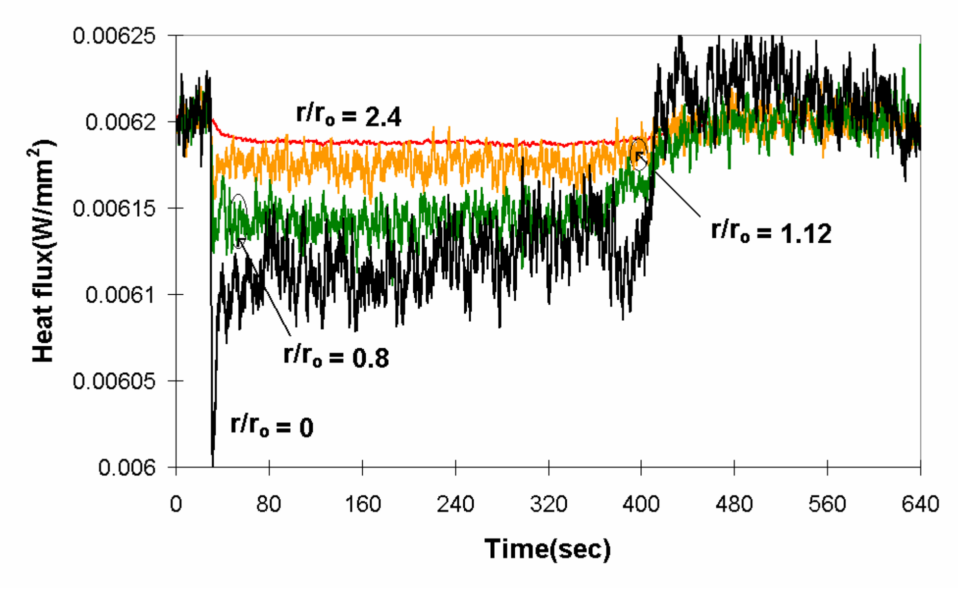

Fig. 3.40 Tomographic temporal heat flux drop profile T_{dry} =40°C, 5µl

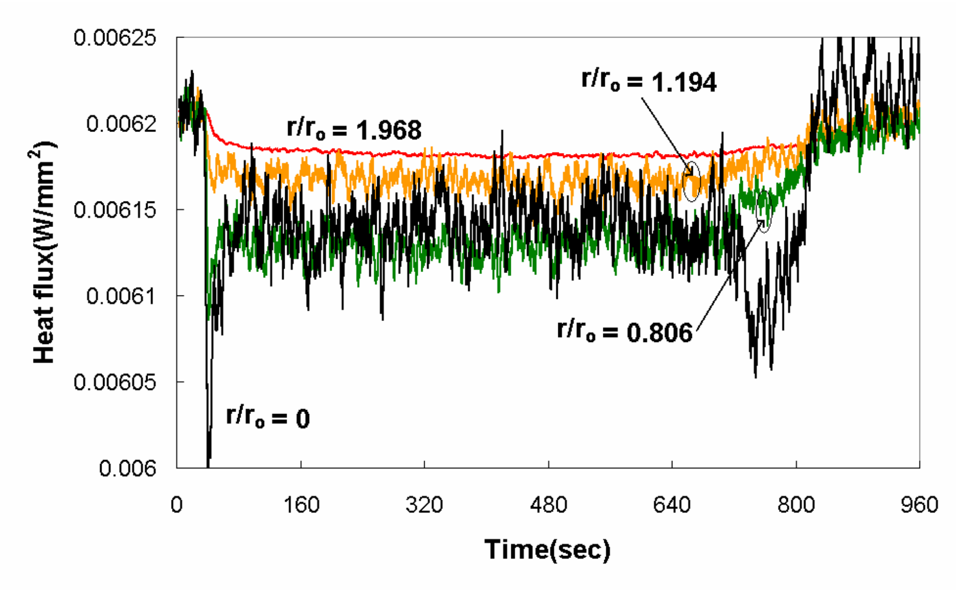

Fig. 3.41 Tomographic temporal heat flux drop profile T_{dry} =40°C, 10µl

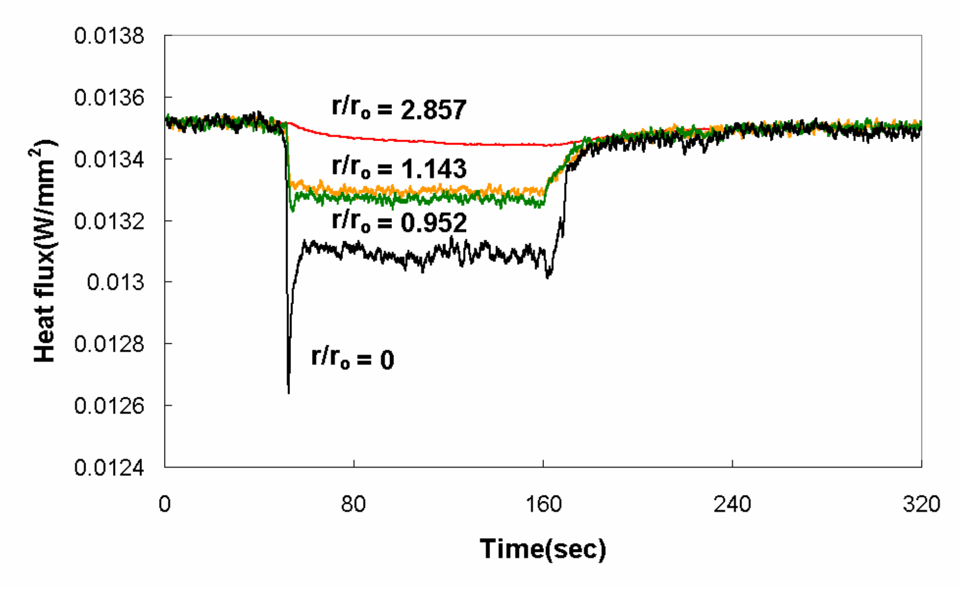

Fig. 3.42 Tomographic temporal heat flux drop profile T_{dry} =60°C, 3μl

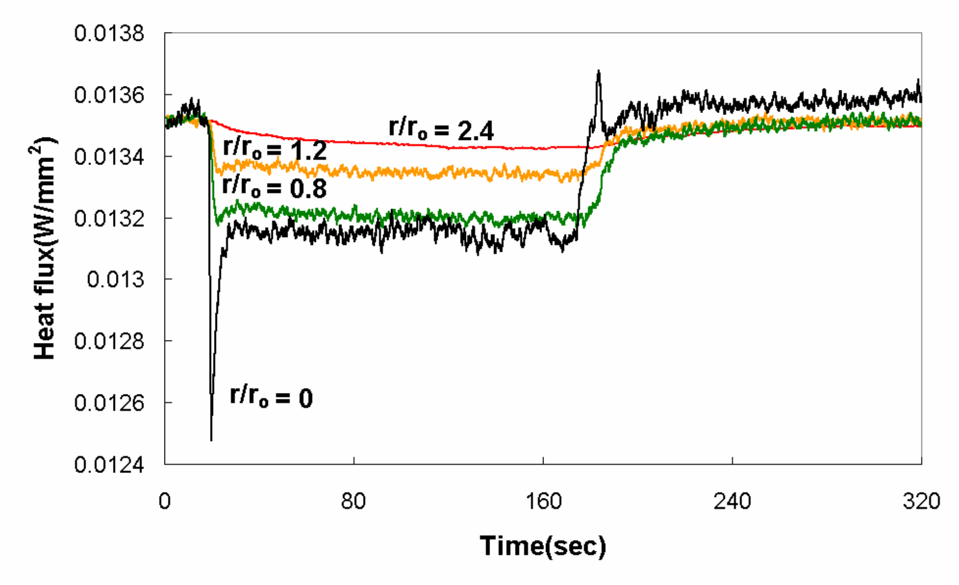

Fig. 3.43 Tomographic temporal heat flux drop profile T_{dry} =60°C, 5μl

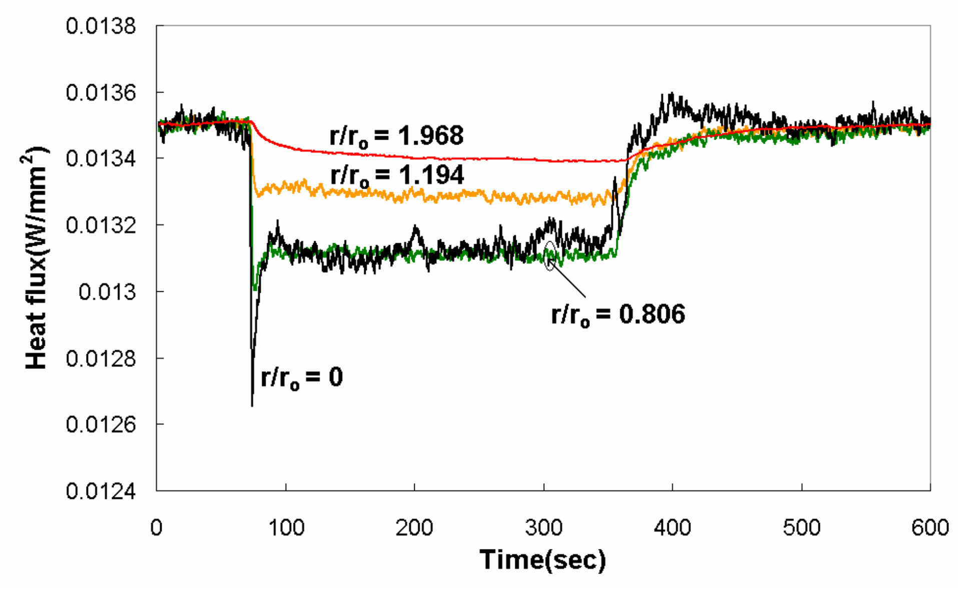

Fig. 3.44 Tomographic temporal heat flux drop profile T_{dry} =60°C, 10μl

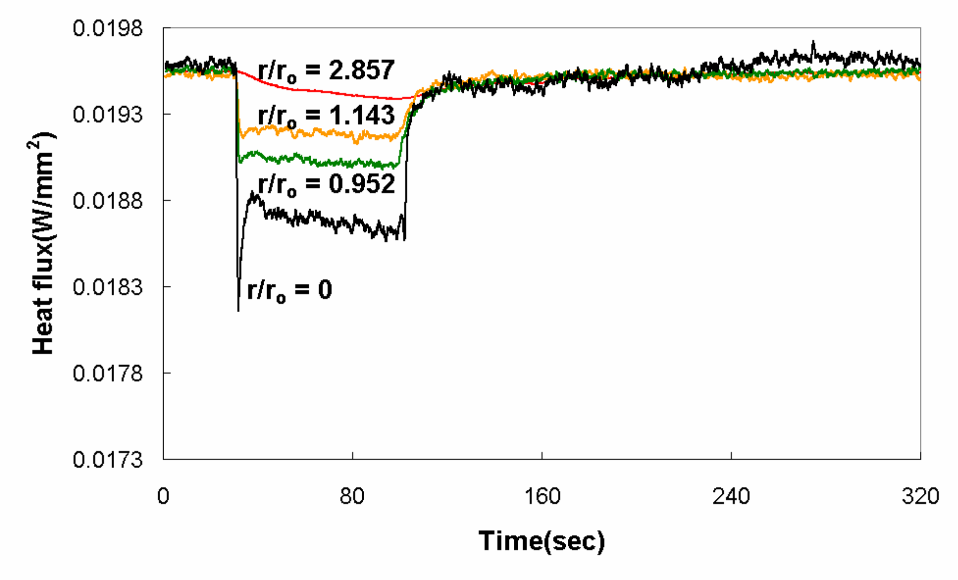

Fig. 3.45 Tomographic temporal heat flux drop profile T_{dry} =80°C, 3μl

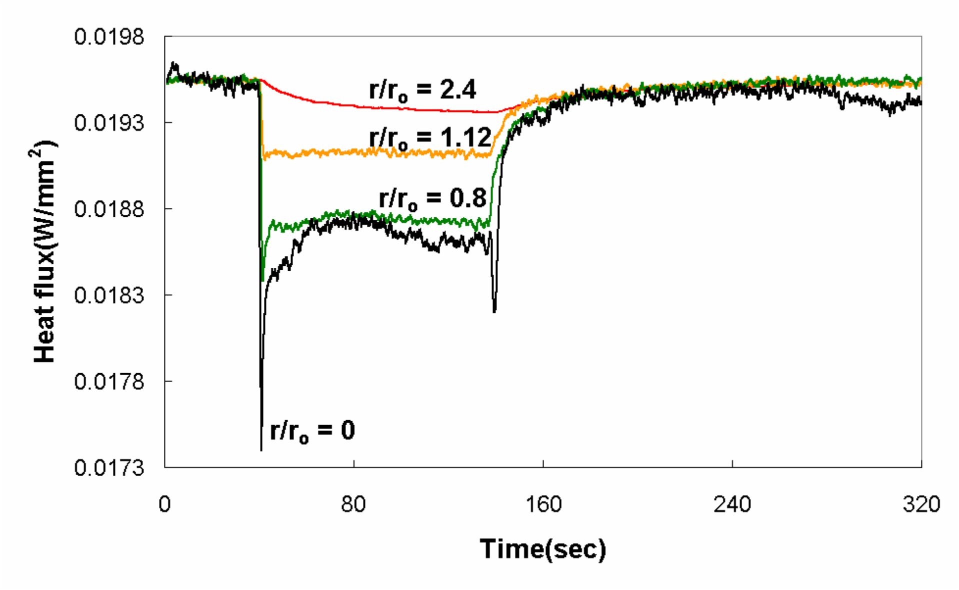

Fig. 3.46 Tomographic temporal heat flux drop profile T_{dry} =80°C, 5μl

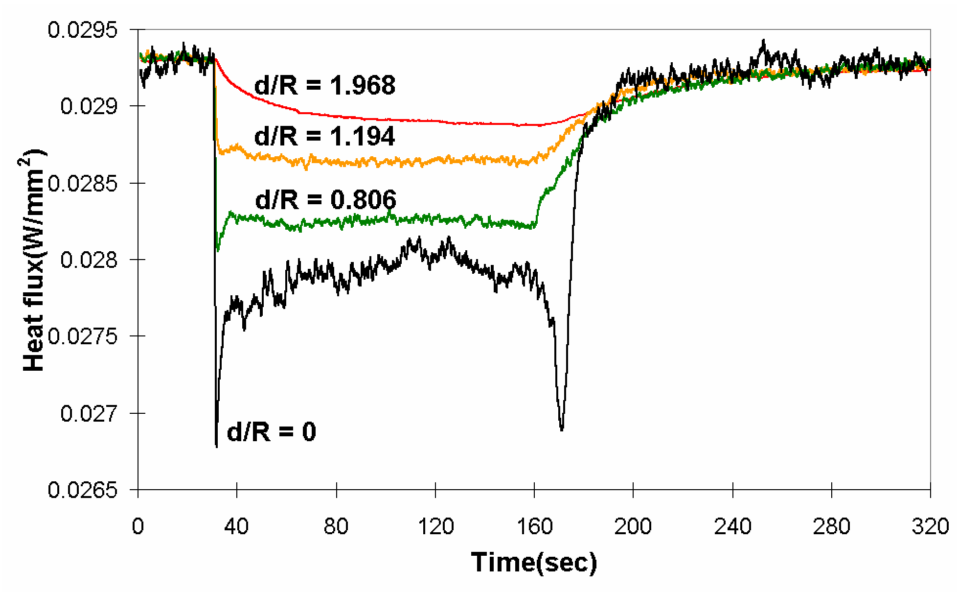

Fig. 3.47 Tomographic temporal heat flux drop profile T_{dry} =80°C, 10μl

3.7 Remarks

Constant voltage droplet evaporation experiment was done on the heated microheater. Temperature and heat flux were measured temporally and spatially with temperature-resistance relation of gold.

CHAPTER IV

CONSTANT TEMPERATURE DROPLET EVAPORATION EXPERIMENT

4.1 Feedback circuit

In Chapter III, droplet evaporation experiments under constant voltage were explained. When the evaporation begins, the heat flux amount is much larger than the microheater's fixed capacity of heat flux. That's why heater temperature drops sharply at the moment the droplet hits the heater surface, as illustrated in the graphs of Chapter III.

As the microheater itself is very small, the heat capacity of the microheater can be negligible compared with a glass substrate. Therefore, when the droplet hits the microheater, we measure the microheater's temperatures, but these temperatures are also as good as the substrate's temperatures just beneath or just to the side of the microheater. Constant voltage of microheater droplet evaporation experiments actually simulate the evaporation of a droplet on a constantly heated surface of a thermally nonconducting material.

Natural heat flux supply does not back up the temperature loss automatically, but if a heated surface has very good thermal conductivity and is very thick, then this heated surface will maintain about the same temperature for small disturbances, like droplet evaporation on top of this surface.

Because it is impossible to use the above conditions in a real experiment, we simulated this constant temperature surface condition with a feedback circuit whose basic operational principle is based on the constant temperature hot wire anemometer [38-40]. For all 32 heaters, we attached a feedback circuit and then respectively supplied enough power to maintain each heater at a constant temperature. Fig. 1 shows the schematic diagram of a feedback circuit, which is composed of Wheatstone bridge and high gain DC amplifier. In this circuit, a 5.1Ω, 1kΩ, a microheater resistance, and a 5kΩ variable resistor make up the Wheatstone bridge, where as a 5.1Ω and 1kΩ are fixed resistors and a 5kΩ range variable resistor is used for setting the working temperature of a heater wire.

Since the Wheatstone bridge and the amplifier are connected, heater working resistance can be found by the following well known bridge balance equation

$$R_{heater} = \frac{R_1 R_4}{R_3} \qquad (4.1)$$

We attached a Bourns® 15 turn, 50 per division dial on the precision 10 turn 2W potentiometer so we could set the potentiometer with the precision of 10 ohm per division. This means we can set the variable resistor with an increment of 0.2% of characteristic resistance, or by using equation (4.1) and (2.1), we can set the temperature of microheater with an accuracy of 1°C.

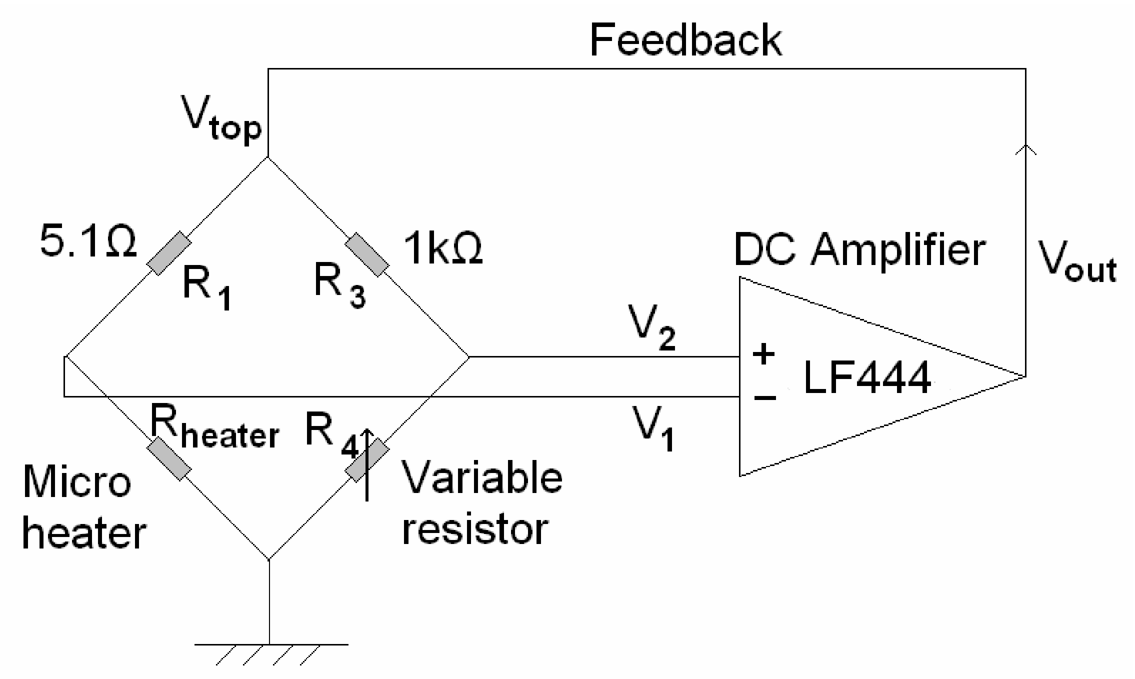

Fig. 4.1 Schematic diagram of a Wheatstone bridge feedback circuit

Equation (4.1) is the condition for a Wheatstone bridge to be in balanced state. From Fig. 1, when the Wheatstone bridge is balanced, $V_1=V_2$, but if the Wheatstone bridge is not balanced, then $V_1 \neq V_2$. The OP amp amplifies this voltage difference, $\Delta V = V_2 - V_1$. The equation for the OP amp is shown at equation (4.2)

$$V_{out} = G(V_2 - V_1) \tag{4.2}$$

where, G means gain of OP amp.

To get the power consumption at the microheater, we need to measure V_{top} and V_1. From these two voltages,

$$V_{top} - V_1 = I_{heater} R_1$$

$$I_{heater} = \frac{V_{top} - V_1}{R_1} \tag{4.3}$$

By using this current information (Eq. 4.3), we can get the power of the heater with a simple calculation.

$$P_{heater} = V_1 I_{heater} = V_1 \frac{V_{top} - V_1}{R_1} \tag{4.4}$$

Heat flux can be obtained by Eq. (4.5)

$$q'' = \frac{P_{heater}}{unit\ area} \qquad (4.5)$$

For our feedback circuit, a National Semiconductor IC OP amp LF444CN is used. The OP amp amplifies the voltage difference of ΔV with the time of G. As seen on Fig. 4.1, voltage difference will be fed back to the Wheatstone bridge. From the balanced Wheatstone bridge state, if the microheater temperature, T_{heater} falls, then the microheater's resistance will fall. Thus, V_1 will fall, and ΔV increases. Then, with equation (4.2), V_{out} is increased. Then, V_{top} is increased, and R_{heater} will be increased. Then, finally T_{heater} will be increased. Without the OP amp, the feedback amount $\Delta V = V_2 - V_1$ is not enough for the constant temperature circuit. It takes too long to back up the original steady state dry heater temperature. The actual feedback circuit is much more complicated than Fig. 4.1. Fig. 4.2 is the picture of our feedback circuit. This circuit could insert into the 14 pin socket so that we could connect all 32 feedback circuits.

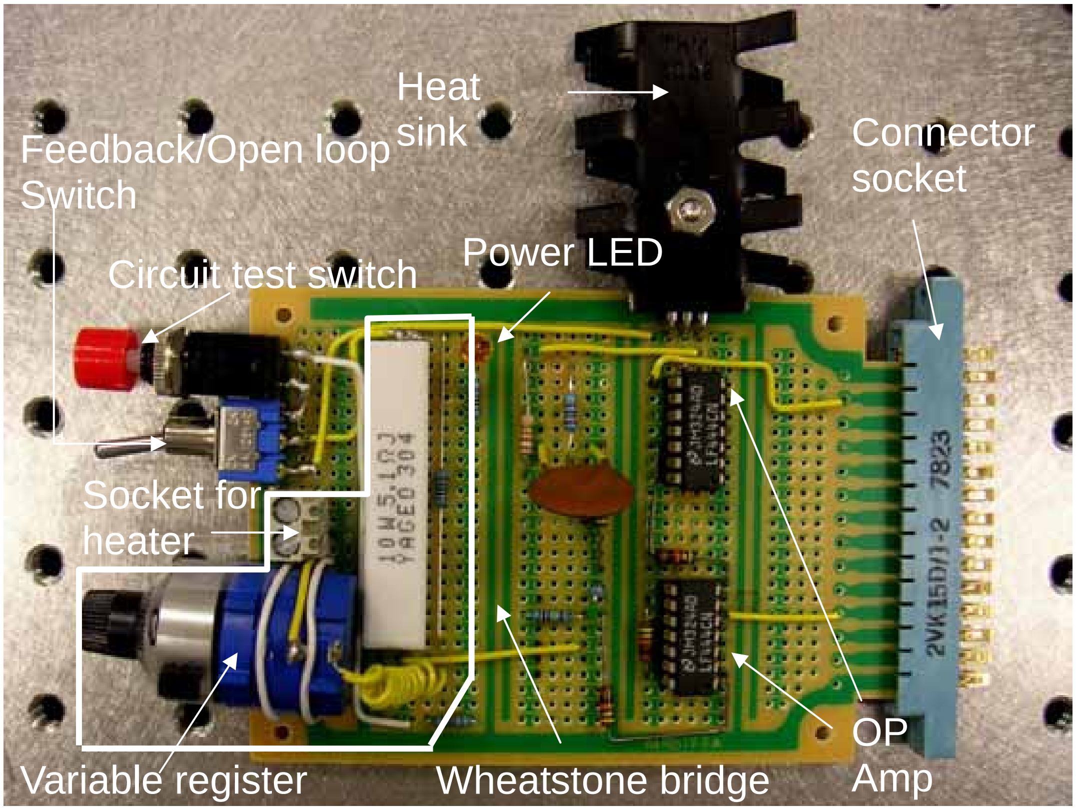

Fig. 4.2 Feedback circuit

4.2 Experimental setup

Data acquisitions were performed with two NI PCI 6013 data acquisition boards and two CB 68-LP connectors. Voltage signals were recorded from two points of the hardware feedback circuit. One is from the bridge top and another is from the point where the heater and 5.1Ω resistor meet, which is indicated as V_1 in Fig. 4.1.

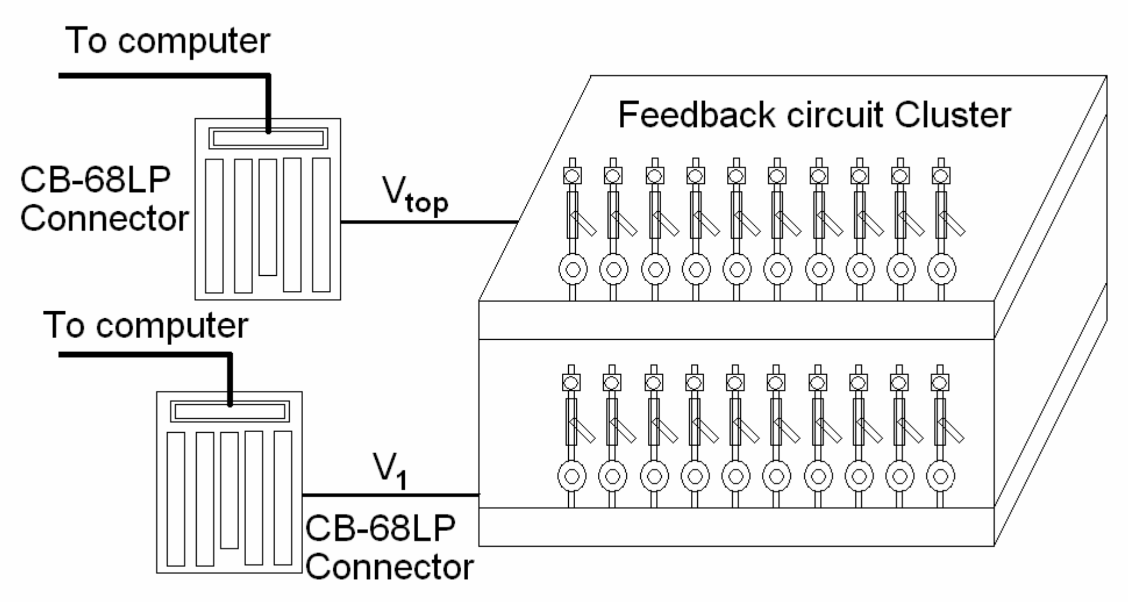

Fig. 4.3 Data acquisition system diagram

All experimental procedures including data acquisition were accomplished automatically by Labview® software. A schematic diagram of the data acquisition system is shown in Fig. 4.3. To minimize the effect of the light, we used the conventional 80W fluorescent light 2 meter above the heater. To capture the images of the droplet evaporation process, a Panasonic GP-KR222 CCD camera and Canon Macrolens FD 50mm were used.

A precision 10-μl syringe is used to apply water droplets at three different volumes of 3μl, 5μl, and 10μl, on the heater array surface. Before each experiment, the microheater surface is thoroughly cleaned with 99.9% isopropyl alcohol and then dried for 30 minutes in a clean environment to ensure a dust-free and stain-free surface.

The droplet contact area varies depending on the amount of the water, from 2.5mm (3μl droplet) to 3.5mm (10μl droplet) in diameter. Droplet shape is very close to spherical at initial contact, and it appears circular when it is viewed from above. When the droplet volume is sufficiently small, surface tension dominates to form its shape upon contact with solid surface because of negligible gravitational deformation. Therefore, we can adopt the spherical cap model [31, 32] for the calculation of the area of droplet surface exposed to air and droplet volume.

Using Eqs. (3.7) and (3.8), the initial contact angles and heights are calculated as 77.6° and 1.005mm for the 3μl droplet, and as 85.5° and 1.618mm for the 10μl droplet assuming perfect sphericity.

Contrary to the heater discussed in Chapter III, the results agree with the generally known fact that constant contact area evaporation is observed when the contact angle is less than 90-degrees [33, 34].

Figs. 4.4 to 4.12 show sequential images of the evaporation progress of the 3μl, 45ºC droplet to the 10μl, 80ºC droplet. At the beginning of evaporation, when $t/\tau = 0$, water contacts the heater surface, and it maintains the same contact area until the evaporation is nearly completed. The diameter of droplet remains the same until about 90% of evaporation has been reached, and then the droplet diameter begins to shrink in a rapid manner. For all tested conditions of three different droplets (3, 5, and 8μl volumes for 45 and 60°C and 3, 5, and 10μl volumes for 80°C), and three different dry temperatures (45, 60, and 80°C), the constant-area evaporation prevails, and their evaporation processes are qualitatively similar.

The dry-out times (Table 4.1) of the tested droplets persistently increase with increasing droplet volume and with decreasing dry-surface temperature. The wetting droplet diameter R is measured as 1.25, 1.50, and 1.75 mm, respectively. The larger droplet increases the contact area between the droplet and the heater surface, and the increased heated surface increases the evaporation rate. While the droplet volume increases more than three times, from 3 μl to 10 μl, the dry-out time increases less than three times because the contact area increases by only 2.1 times, and the evaporation rate is proportional to the contact area.

Table 4.1 Measured dry-out time (τ in seconds) for complete evaporation of droplet for three different droplet volumes and three different dry-surface temperatures

Droplet Volume (μl) → Dry-Surface Temperature (°C)	3 (1.25-mm diameter)	5 (1.5-mm diameter)	8 (1.75-mm diameter)	10 (1.75-mm diameter)
45	107	140	180	
60	63	84	109	
80	35	48		72

(a) $t/\tau = 0$ (Total evaporation time, $\tau = 107.42$) (b) $t/\tau = 0.186$

(c) $t/\tau = 0.372$ (d) $t/\tau = 0.559$

(e) $t/\tau = 0.745$ (f) $t/\tau = 0.959$

Fig. 4.4 Sequential images of slowly evaporating water droplets on the microheater array at T_{dry} = 45°C, 3μl

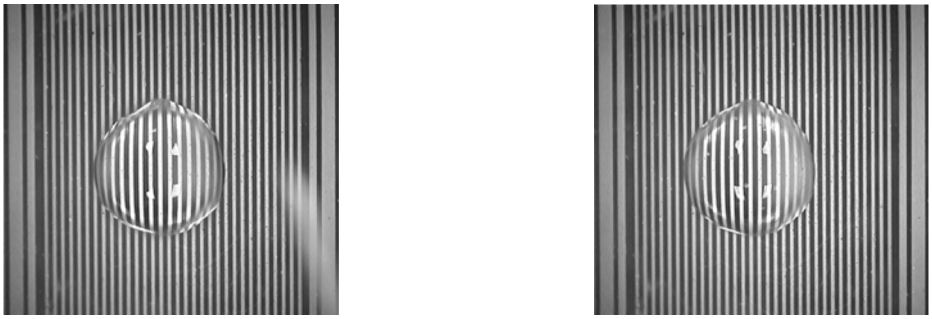

(a) $t/\tau = 0$ (Total evaporation time, $\tau = 139.66$) (b) $t/\tau = 0.186$

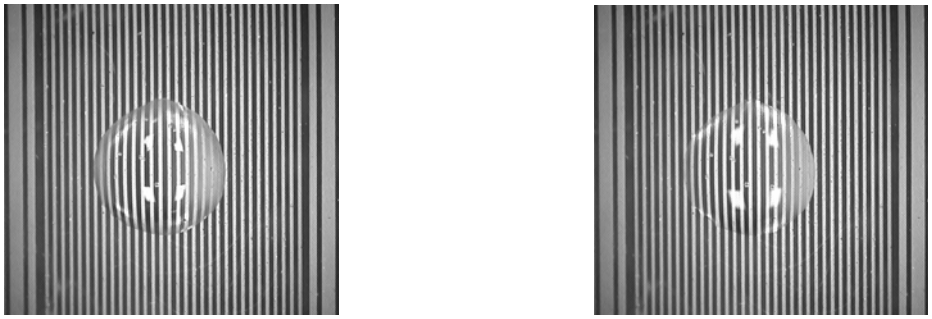

(c) $t/\tau = 0.372$ (d) $t/\tau = 0.559$

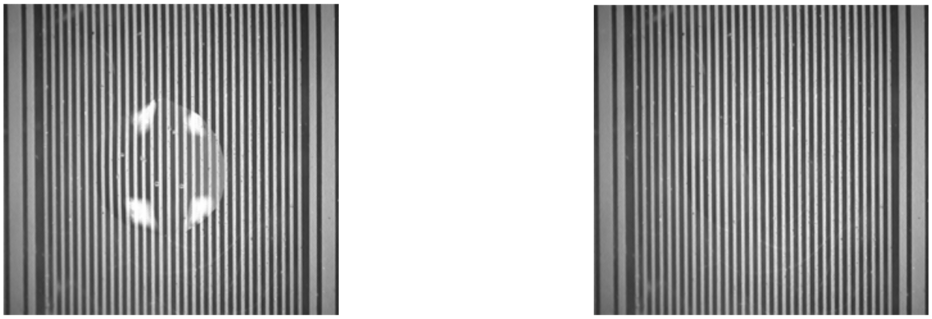

(e) $t/\tau = 0.745$ (f) $t/\tau = 0.995$

Fig. 4.5 Sequential images of slowly evaporating water droplets on the microheater array at T_{dry} = 45°C, 5μl

(a) $t/\tau = 0$ (Total evaporation time, $\tau = 180.09$)   (b) $t/\tau = 0.200$

(c) $t/\tau = 0.400$ (d) $t/\tau = 0.600$

(e) $t/\tau = 0.800$ (f) $t/\tau = 0.988$

Fig. 4.6 Sequential images of slowly evaporating water droplets on the microheater array at T_{dry} = 45°C, 8μl

(a) $t/\tau = 0$ (Total evaporation time, $\tau = 62.50$) (b) $t/\tau = 0.192$

(c) $t/\tau = 0.384$ (d) $t/\tau = 0.576$

(e) $t/\tau = 0.768$ (f) $t/\tau = 0.981$

Fig. 4.7 Sequential images of slowly evaporating water droplets on the microheater array at $T_{\text{dry}} = 60°\text{C}$, 3μl

(a) $t/\tau = 0$ (Total evaporation time, $\tau = 83.67$) (b) $t/\tau = 0.191$

(c) $t/\tau = 0.384$ (d) $t/\tau = 0.574$

(e) $t/\tau = 0.765$ (f) $t/\tau = 0.991$

Fig. 4.8 Sequential images of slowly evaporating water droplets on the microheater array at T_{dry} = 60°C, 5μl

(a) *t/τ* = 0 (Total evaporation time, τ = 108.90) (b) *t/τ* = 0.184

(c) *t/τ* = 0.367 (d) *t/τ* = 0.551

(e) *t/τ* = 0.735 (f) *t/τ* = 0.973

Fig. 4.9 Sequential images of slowly evaporating water droplets on the microheater array at T_{dry} = 60°C, 8μl

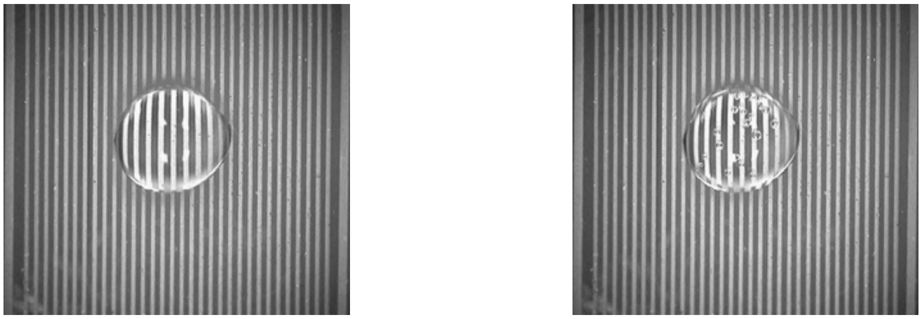

(a) $t/\tau = 0$ (Total evaporation time, $\tau = 35.45$) (b) $t/\tau = 0.198$

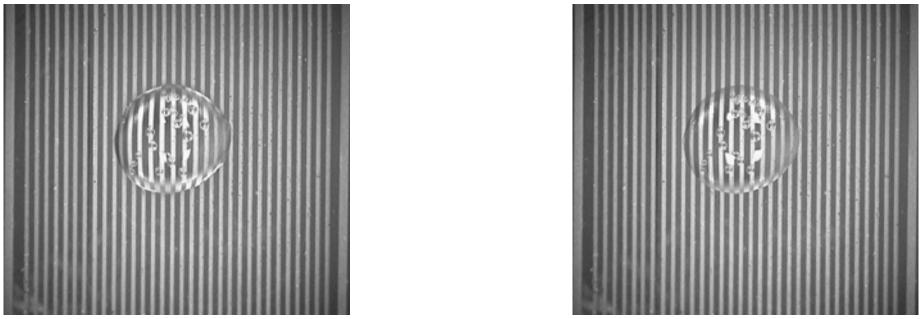

(c) $t/\tau = 0.395$ (d) $t/\tau = 0.592$

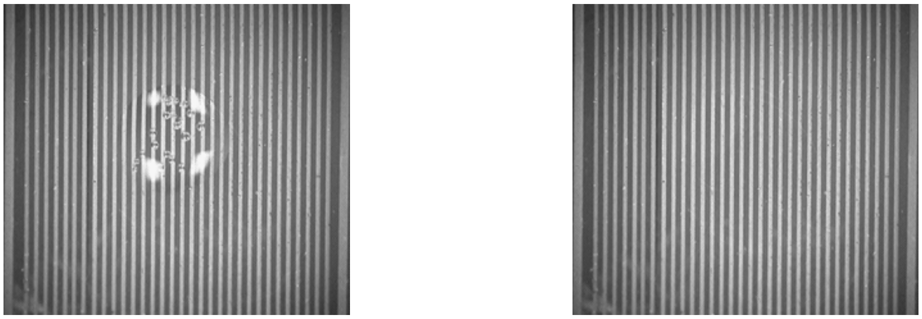

(e) $t/\tau = 0.790$ (f) $t/\tau = 0.987$

Fig. 4.10 Sequential images of slowly evaporating water droplets on the microheater array at T_{dry} = 80°C, 3μl

(a) $t/\tau = 0$ (Total evaporation time, $\tau = 47.69$) (b) $t/\tau = 0.210$

(c) $t/\tau = 0.419$ (d) $t/\tau = 0.629$

(e) $t/\tau = 0.839$ (f) $t/\tau = 0.986$

Fig. 4.11 Sequential images of slowly evaporating water droplets on the microheater array at T_{dry} = 80°C, 5μl

(a) $t/\tau = 0$ (Total evaporation time, $\tau = 71.89$) (b) $t/\tau = 0.209$

(c) $t/\tau = 0.417$ (d) $t/\tau = 0.626$

(e) $t/\tau = 0.833$ (f) $t/\tau = 0.988$

Fig. 4.12 Sequential images of slowly evaporating water droplets on the microheater array at T_{dry} = 80°C, 10μl

4.3 Results and discussion

To set up the working temperature of the heater array, we need to adjust the dial of the potentiometer (variable resistor) in the Wheatstone bridge feedback circuit. By using equation (2), we can set up the heater temperature as 45°C, 60°C, and 80°C. Fig. 4.13 is the empirical relation of heat flux and microheater temperature.

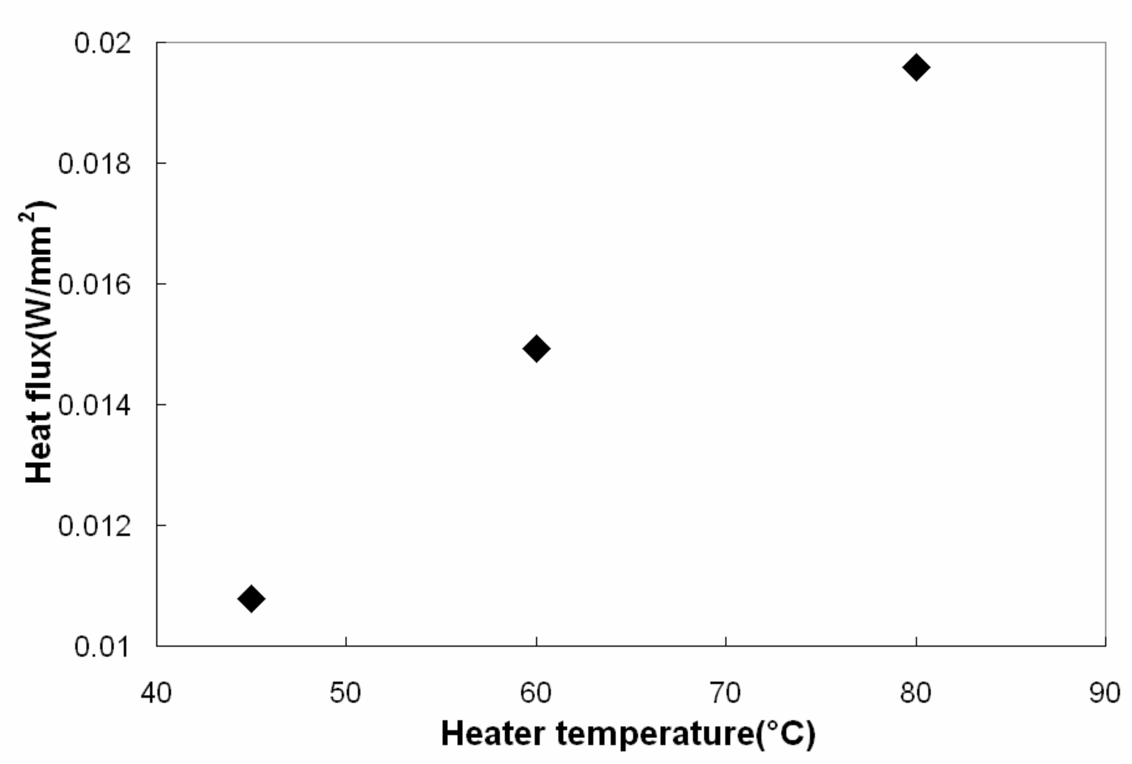

Fig. 4.13 Heater flux of microheater at dry steady state

The tomographic deconvolution technique, which was applied in Chapter III, is applied to this chapter to obtain the heat flux distribution information. The spatial heat flux of the microheater obtained by tomographic deconvolutions is shown in Fig. 4.14 to 4.16. Line-averaged raw heat flux is not shown, as it has been proved to be a low reliable method in representing the exact temperature of the microheater surface.

Figs. 4.14-4.16 show spatial development of tomographically deconvoluted temperature profiles for 3μl, 5μl, and 8μl droplets for the cases of 45°C and 60°C, and for 3μl, 5μl, and 10μl droplets for the case of 80°C dry heater temperature.

When the radial distance is normalized by the wet radius of each droplet, all three profiles for the three droplets rise together showing similar development for practically the entire test period. Upon contact, the largest heat flux is a result of the instantaneous maximum cooling rate (Figs. 4.14-4.16-a). Heat flux remains nearly unchanged during the evaporation in which a latent heat transfer process at a constant heat flux prevails (Figs. 4.14-4.16-b to d). Then heat flux returns to the dry heater state after completion of evaporation (Figs. 4.14-4.16-e), and fully recovers to it in $t = 2.0\tau$ (Figs. 4.14-4.16-f)

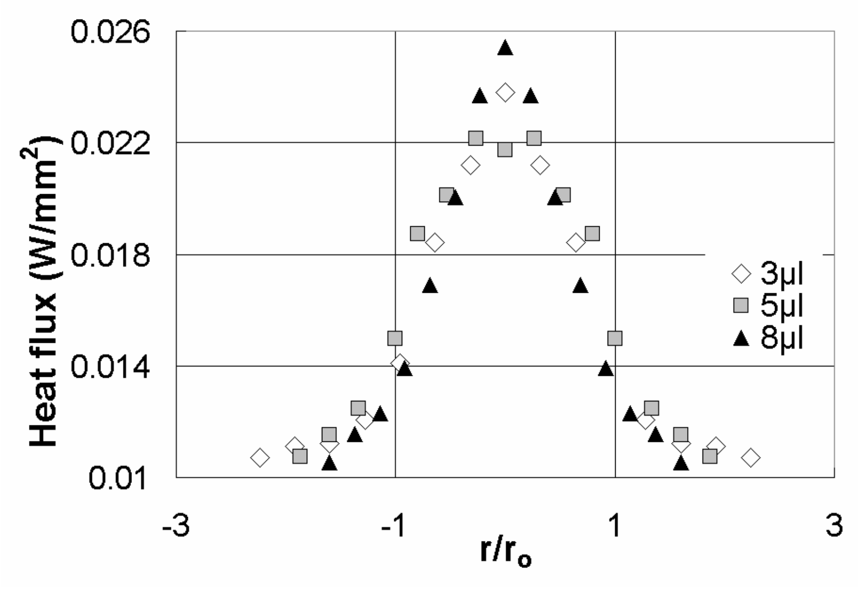

(a) t/τ = 0.01

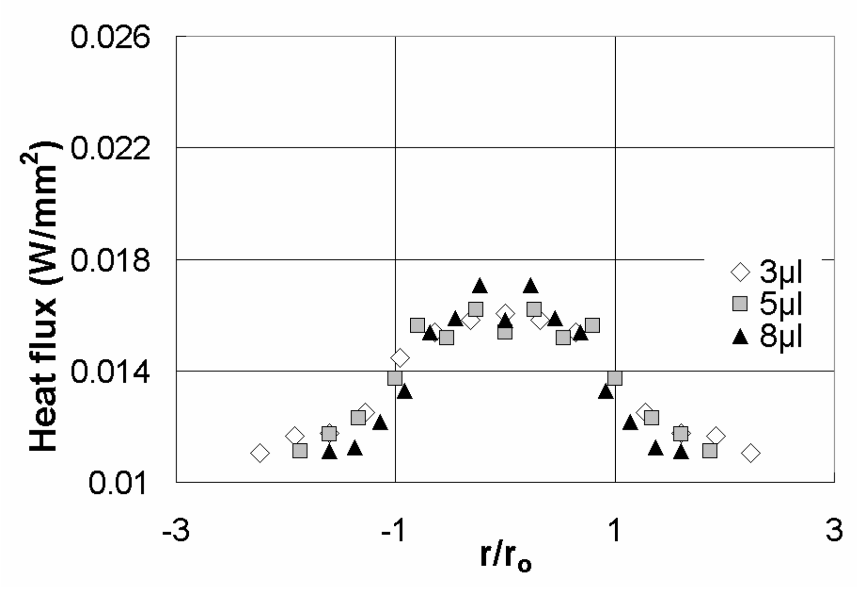

(b) t/τ = 0.1

Fig. 4.14 Tomographic heat flux variation profile at T_{dry} = 45°C

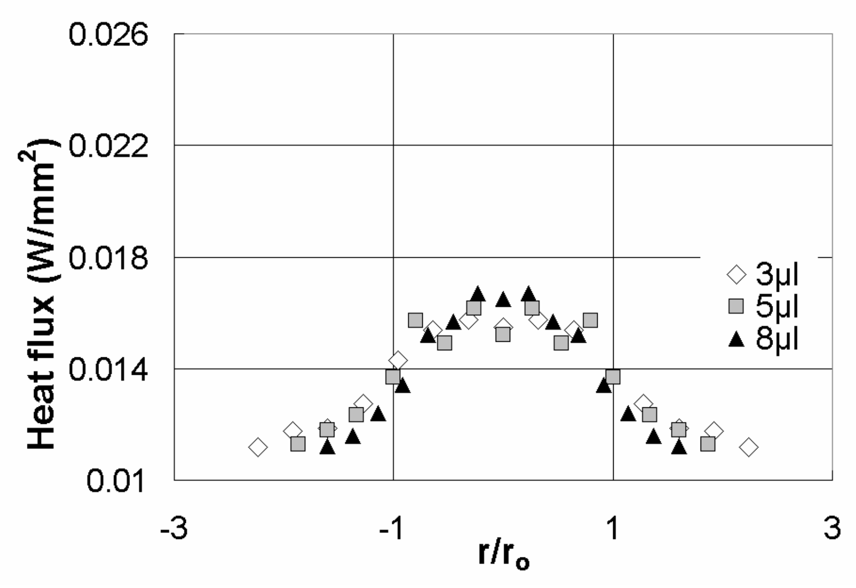

(c) t/τ = 0.5

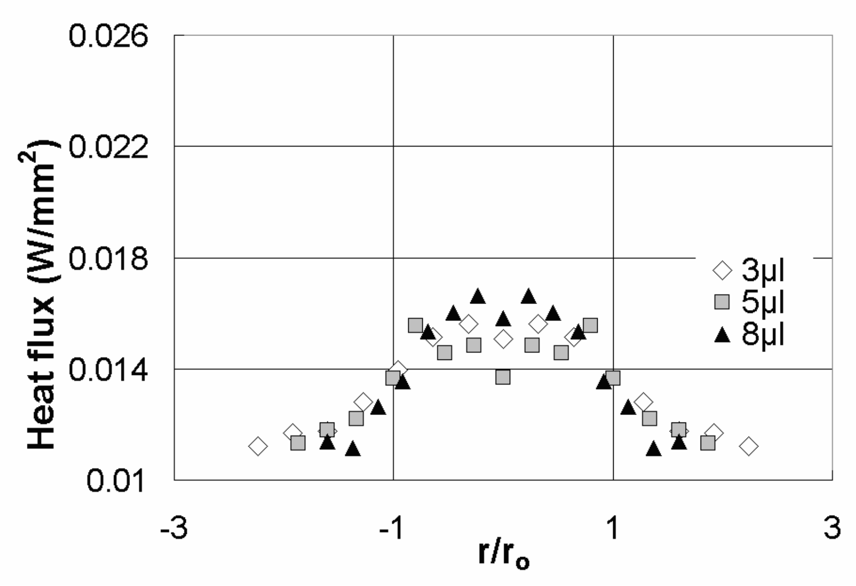

(d) t/τ = 0.9

Fig. 4.14 Continued

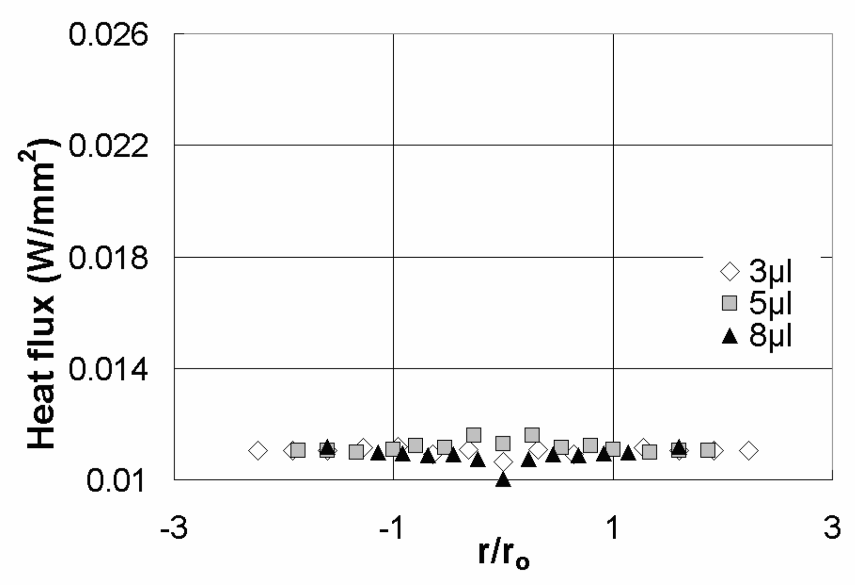

(e) t/τ = 1.1

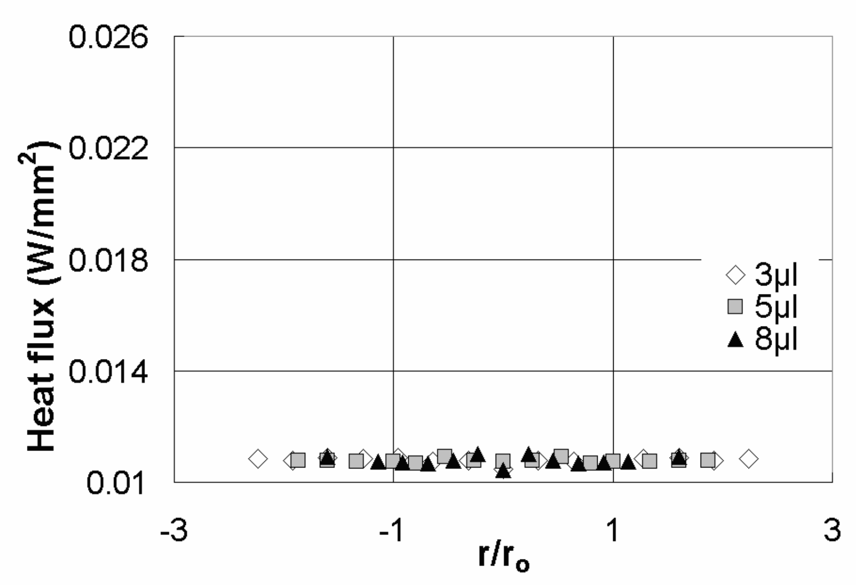

(f) t/τ = 2.0

Fig. 4.14 Continued

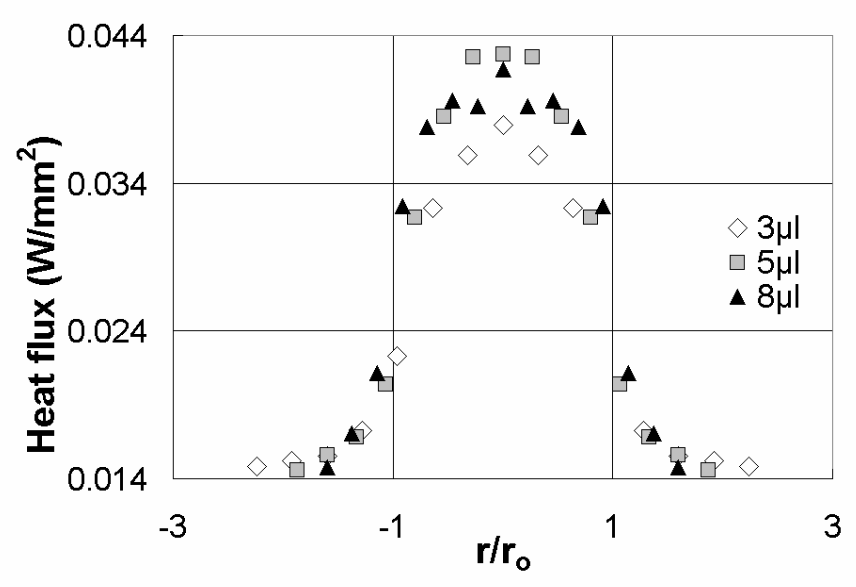

(a) t/τ = 0.01

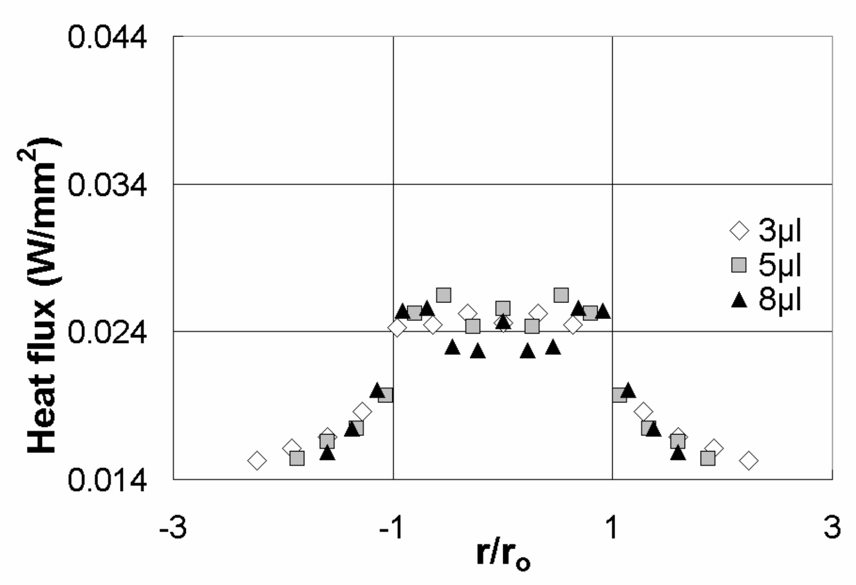

(b) t/τ = 0.1

Fig. 4.15 Tomographic heat flux variation profile at T_{dry} = 60°C

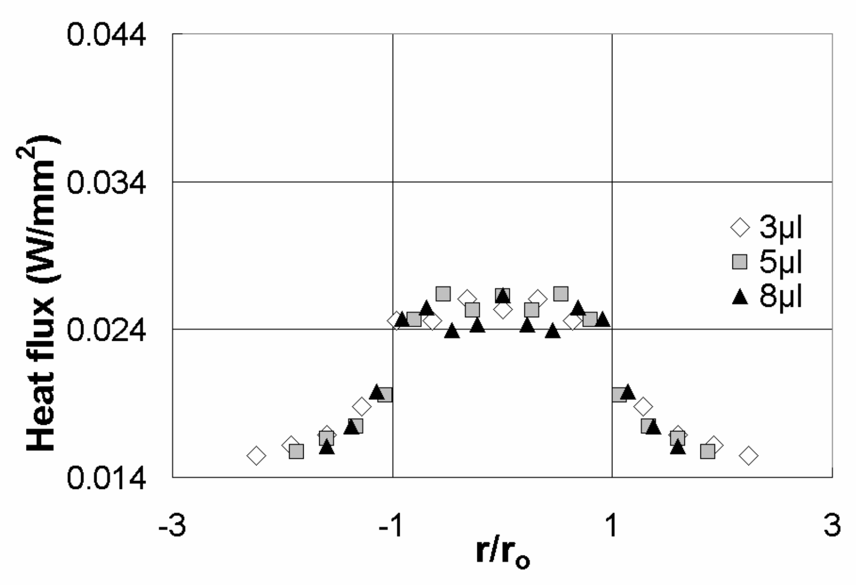

(c) t/τ = 0.5

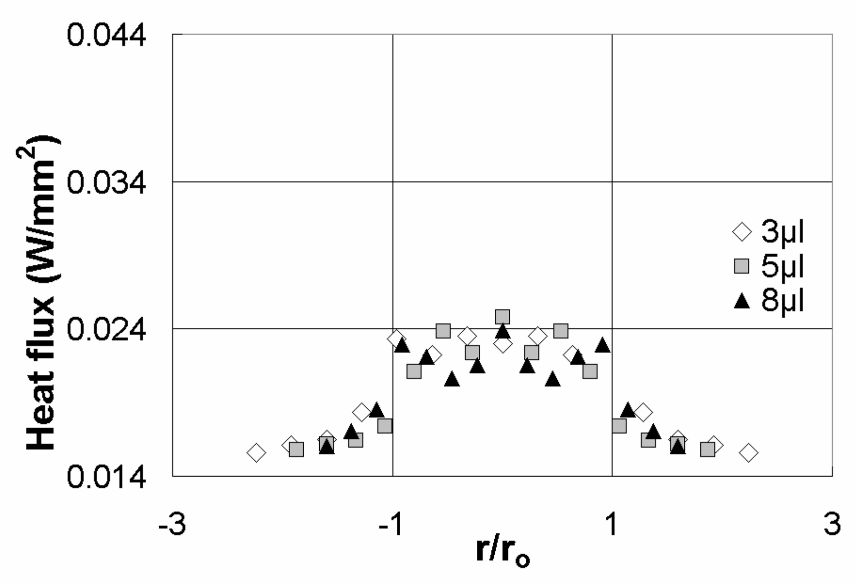

(d) t/τ = 0.9

Fig. 4.15 Continued

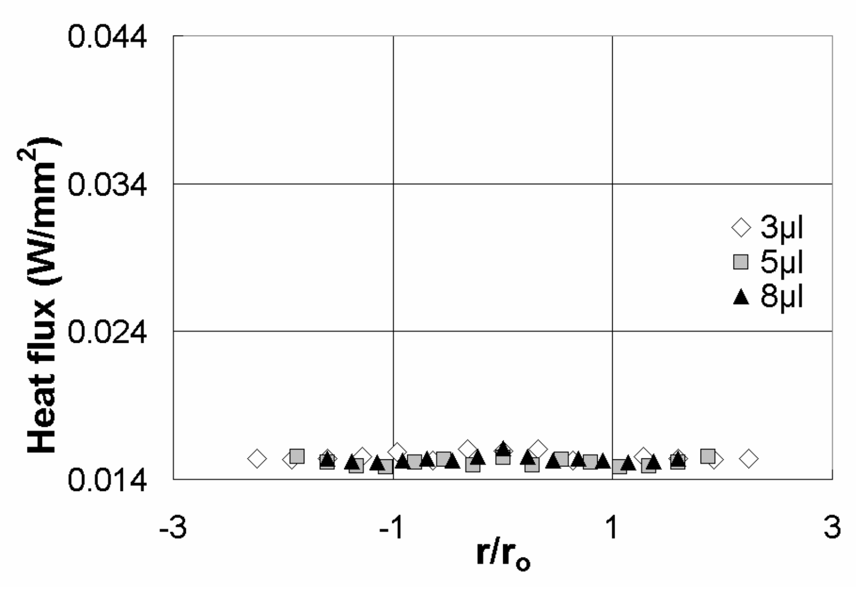

(e) t/τ = 1.1

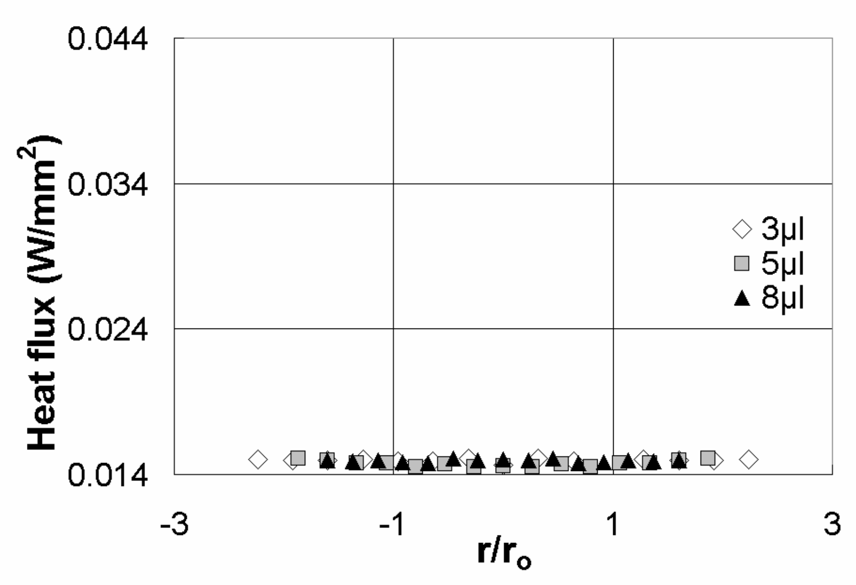

(f) t/τ = 2.0

Fig. 4.15 Continued

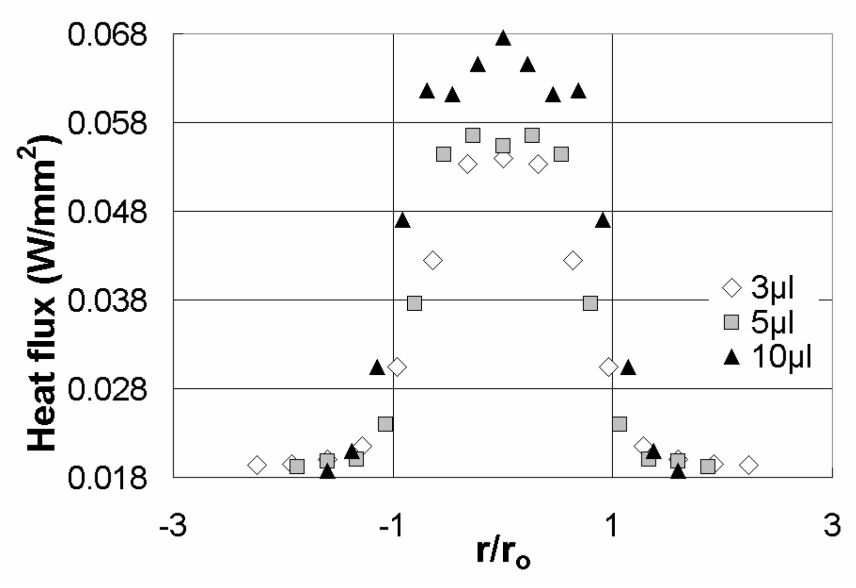

(a) t/τ = 0.01

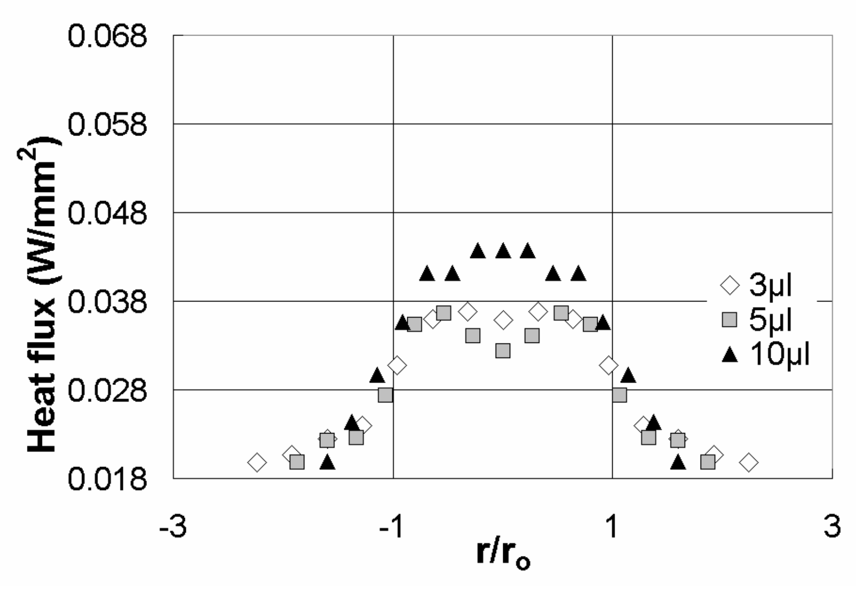

(b) t/τ = 0.1

Fig. 4.16 Tomographic heat flux variation profile at T_{dry} = 80°C

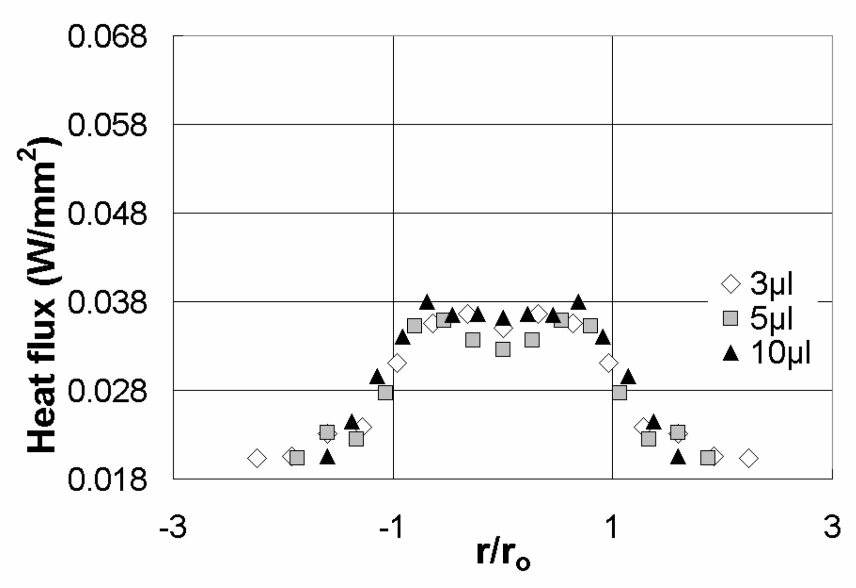

(c) t/τ = 0.5

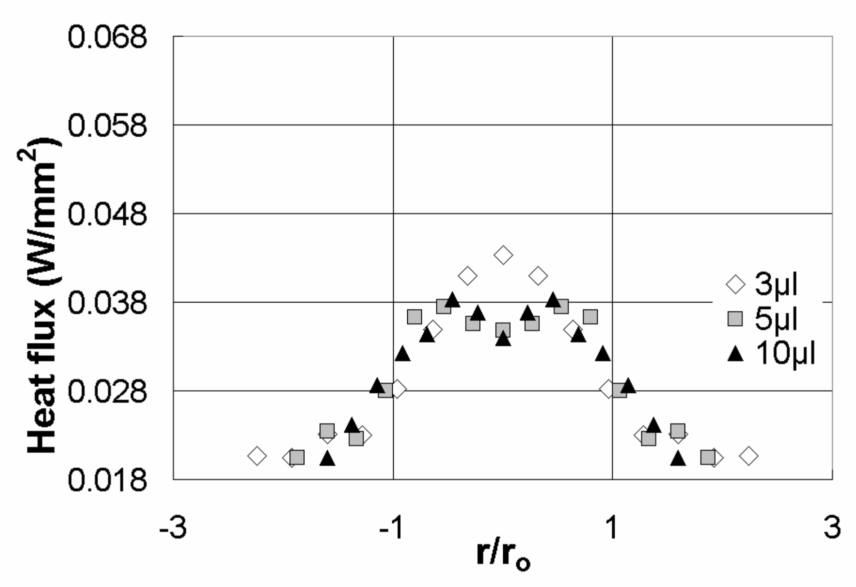

(d) t/τ = 0.9

Fig. 4.16 Continued

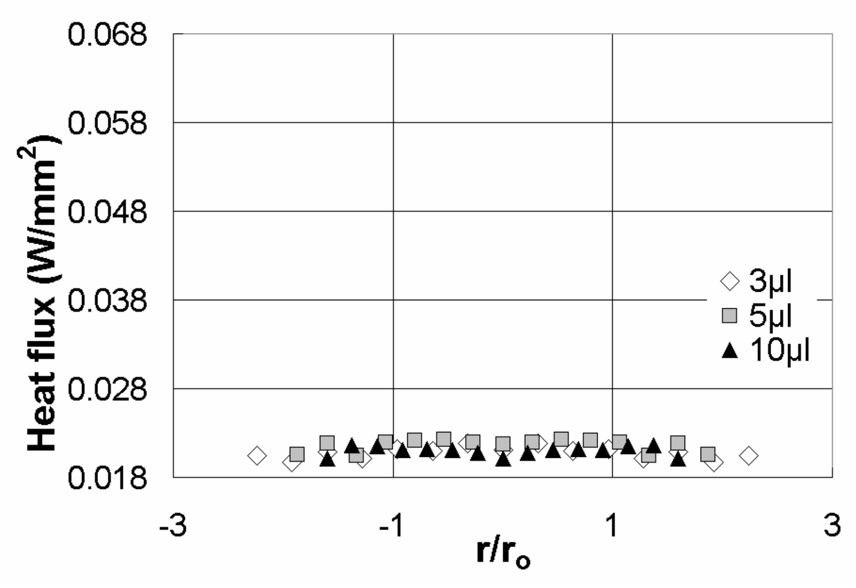

(e) t/τ = 1.1

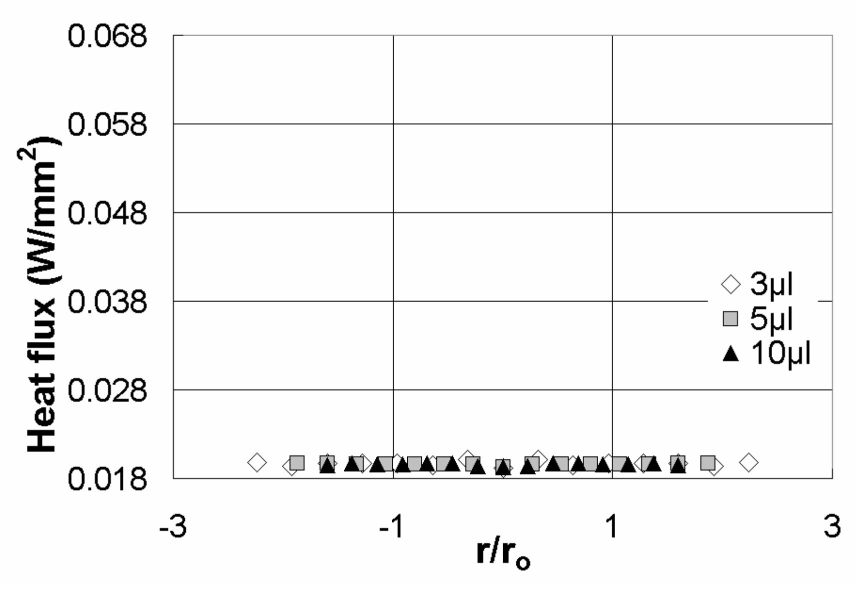

(f) t/τ = 2.0

Fig. 4.16 Continued

Figs. 4.17 to 4.19 show temporal heat flux variations measured at the center of the heater surface for all three dry heater temperatures of 45°C, 60°C, and 80°C, and each of Figs. 4.17 to 4.18, respectively, shows heat flux variations for the cases of 3μl, 5μl, and 8μl droplets. Fig. 4.19 show heat flux variations for the cases of 3μl, 5μl, and 10μl droplets. For each of the nine cases shown in Figs. 4.17 to 4.19, a maximum heat flux peak is experienced at $t = 0$. The amounts of heat flux increase remain unchanged almost for the entire evaporation period before they recover to the dry heater temperature upon completion of evaporation. Heaters recover to the original dry heat flux quickly after evaporation ends.

Note that for the cases of the highest heater temperature (Fig. 4.19), sudden heat flux peaks are apparent at the final stage of evaporation. It is conjectured that this is attributed to a possible contraction of the relatively thin droplet at the later stage because of the thermocapillary action. In other words, the relatively lower air-water interfacial temperature at the droplet center increases the local surface tension so that the surface flow is induced toward the center from the droplet rim at relatively high temperatures and smaller surface tension. Thus, at the final stage of the evaporation, the center region of the water droplet is suddenly thickened based on the droplet contraction so that the increased local mass enhances the cooling and momentarily increases the heat flux.

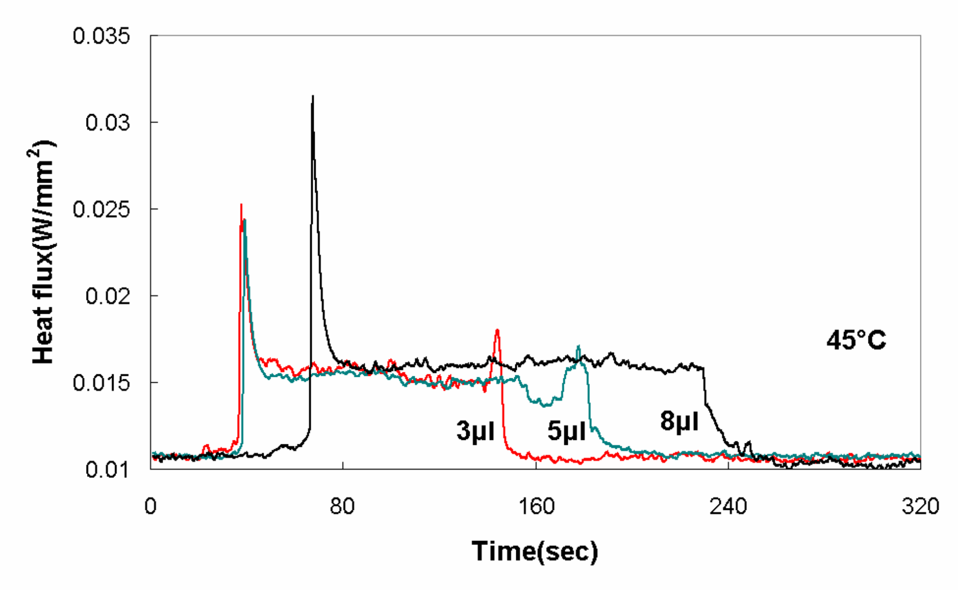

Fig. 4.17 Tomographic temporal heat flux variation profile at T_{dry} = 45°C

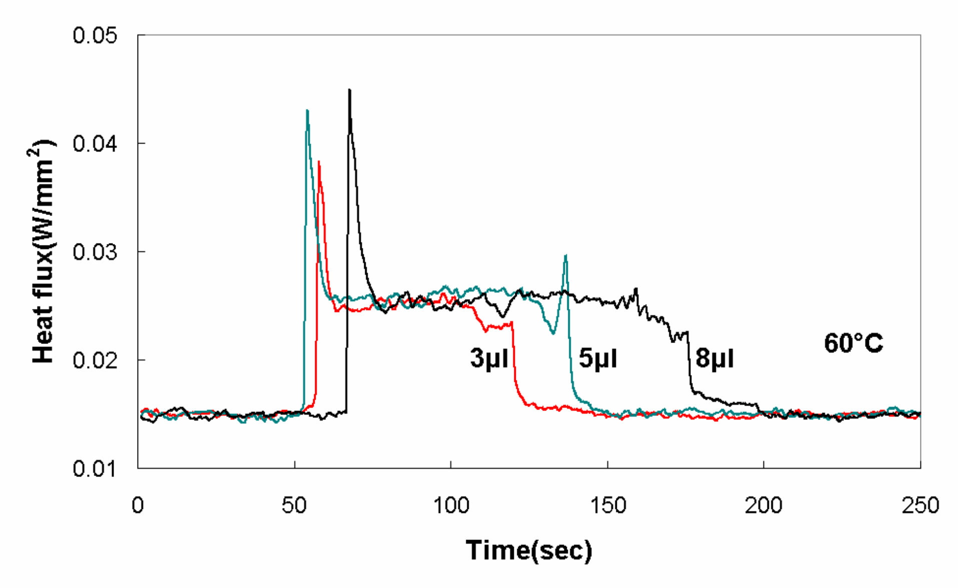

Fig. 4.18 Tomographic temporal heat flux variation profile at T_{dry} = 60°C

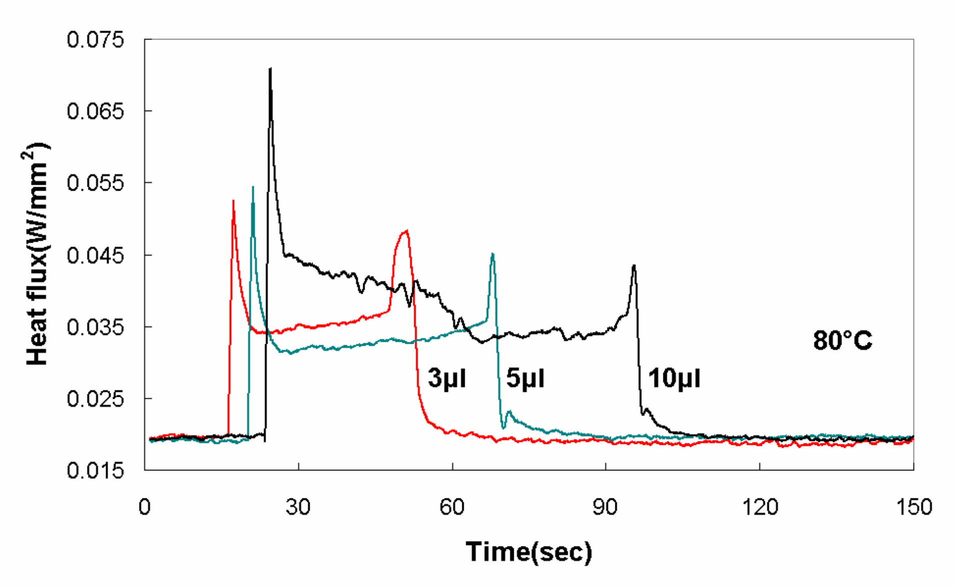

Fig. 4.19 Tomographic temporal heat flux variation profile at T_{dry} = 80°C

Figs. 4.20 to 4.28 show temporal variations of heat flux at four selected radial locations for the cases of 50°C, 60°C, 80°C dry heater temperature with 3μl, 5μl, 8μl droplets evaporating in Figs. 4.20 to 4.25, and 3μl, 5μl, 10μl droplets evaporating in Figs. 4.26 to 4.28. The initial heat flux increase upon droplet impact is most pronounced at the center (r/r_o = 0), and the amount of heat flux is about the same at the inside of the droplet for almost the entire evaporation period. The heat flux peak exists only inside of the droplet while outside the droplet boundary the heater surface heat flux gradually increased. The sudden heat flux peak near the completion of evaporation, as discussed with Figs. 4.17 to 4.19 above, does not exist other than at the droplet center, and this supports the conjecture of sudden thickening of the central region driven by the thermocapillary phoresis.

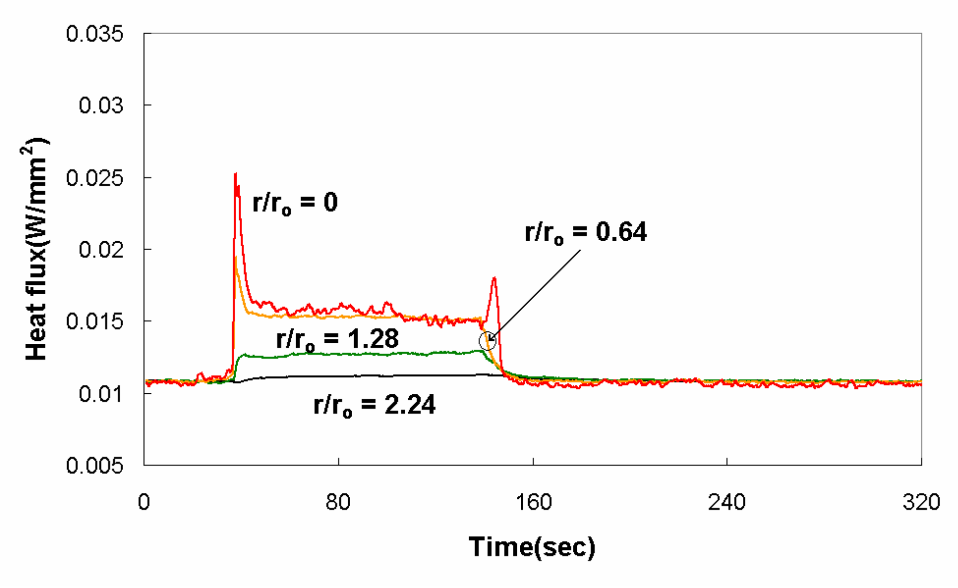

Fig. 4.20 Tomographic temporal temperature variation profile T_{dry} =45°C, 3μl

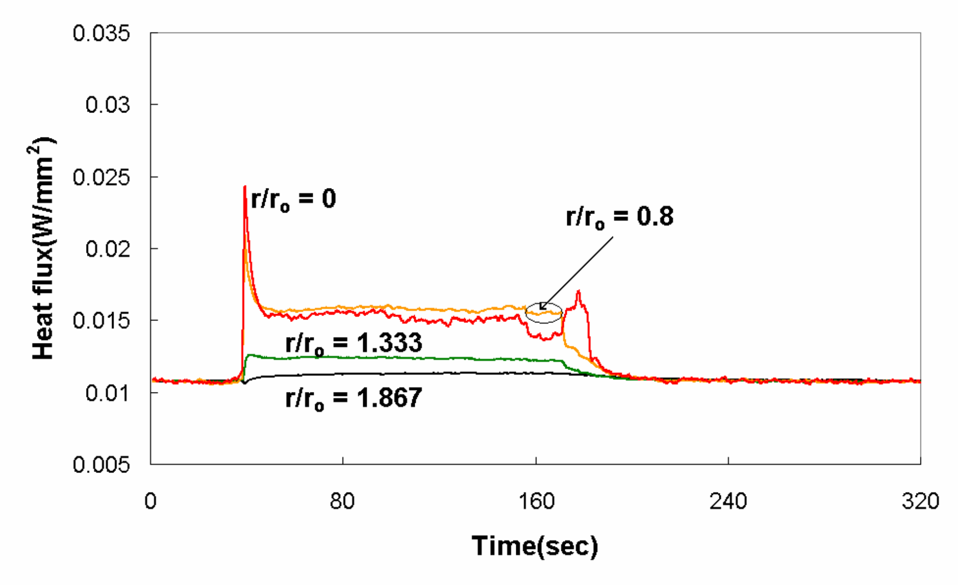

Fig. 4.21 Tomographic temporal temperature variation profile T_{dry} =45°C, 5μl

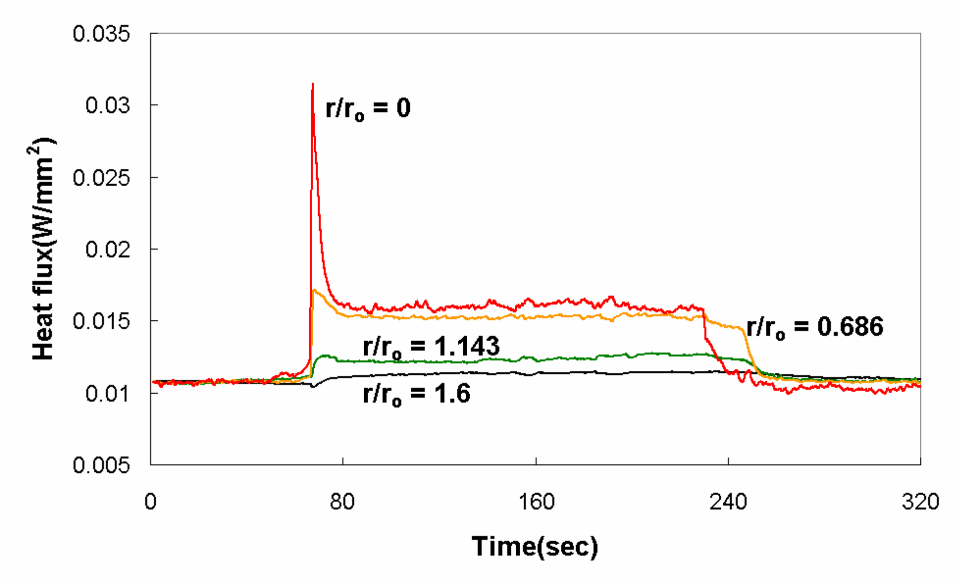

Fig. 4.22 Tomographic temporal temperature variation profile T_{dry} =45°C, 8μl

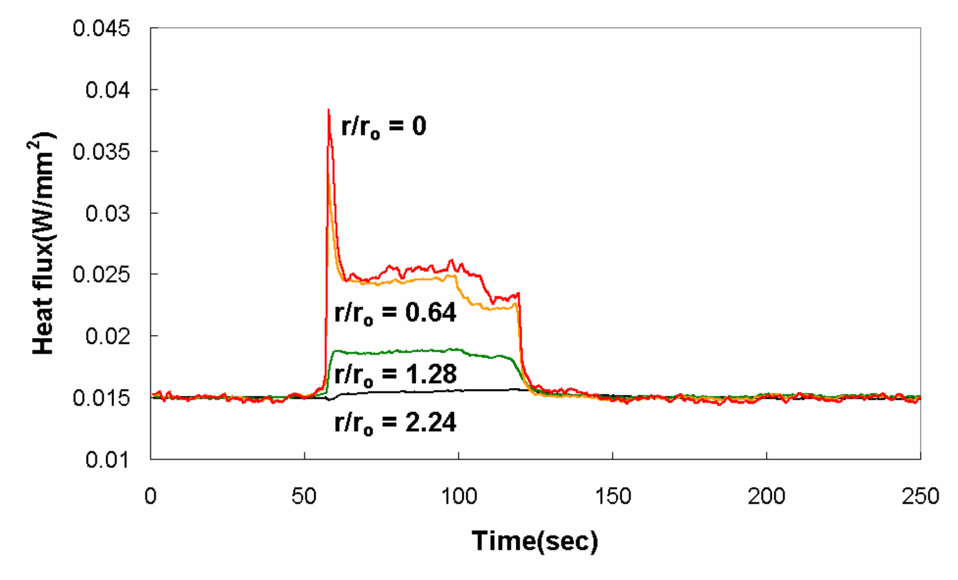

Fig. 4.23 Tomographic temporal temperature variation profile T_{dry} =60°C, 3μl

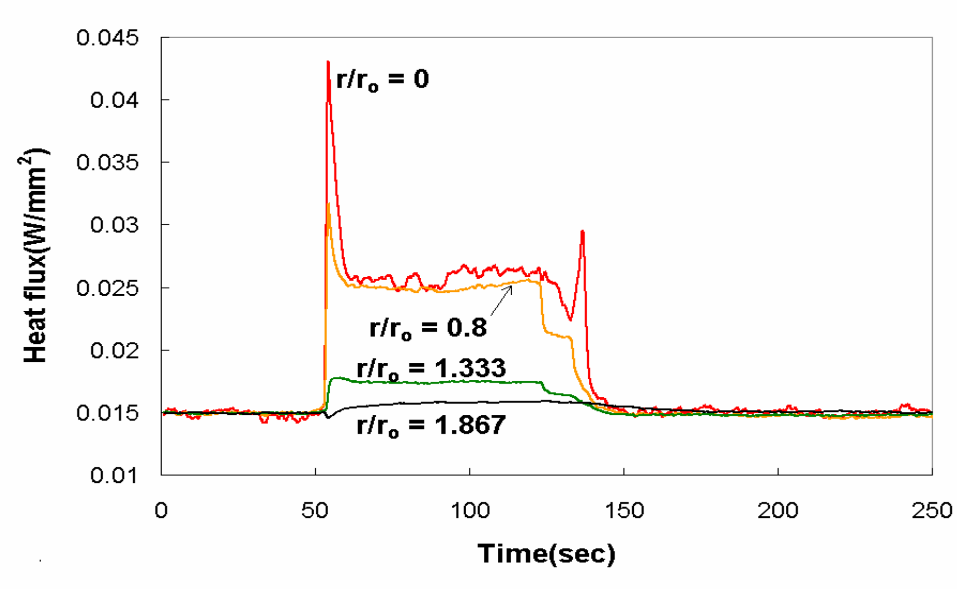

Fig. 4.24 Tomographic temporal temperature variation profile T_{dry} =60°C, 5μl

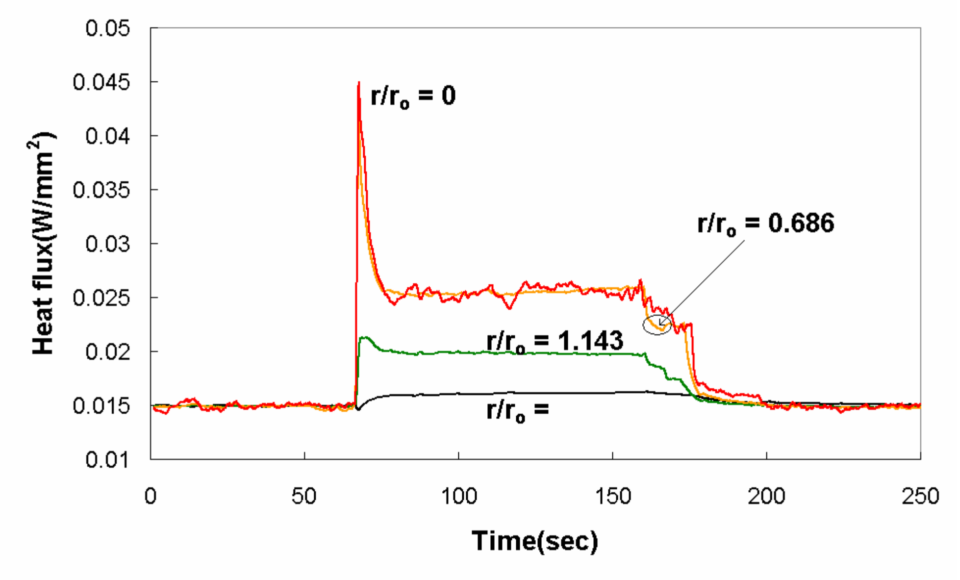

Fig. 4.25 Tomographic temporal temperature variation profile T_{dry} =60°C, 8μl

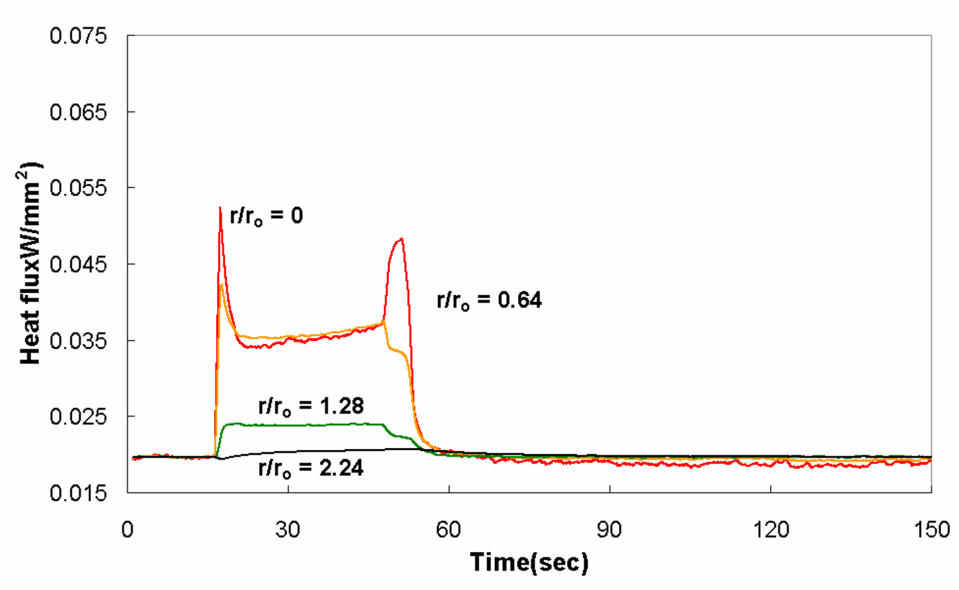

Fig. 4.26 Tomographic temporal temperature variation profile T_{dry} =80°C, 3μl

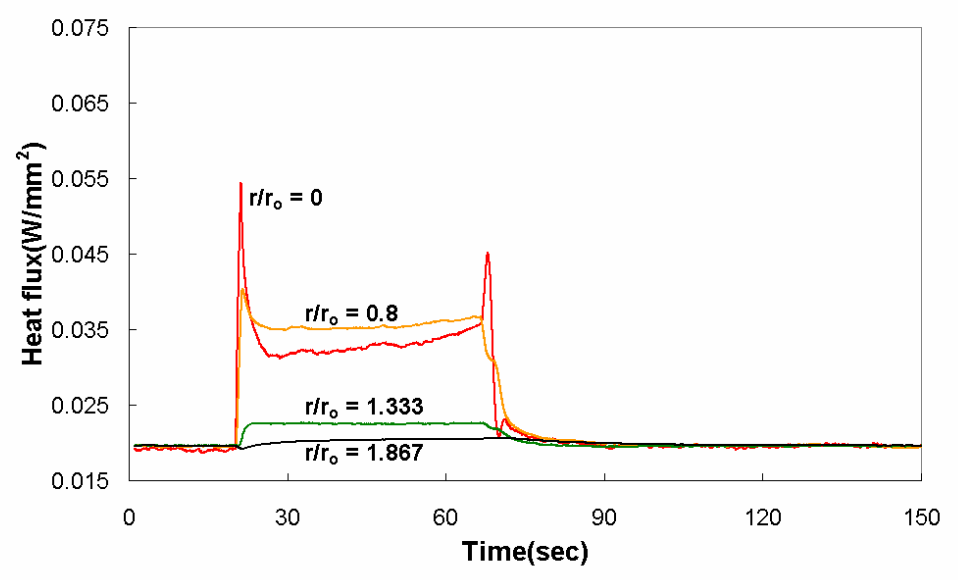

Fig. 4.27 Tomographic temporal temperature variation profile T_{dry} =80°C, 5μl

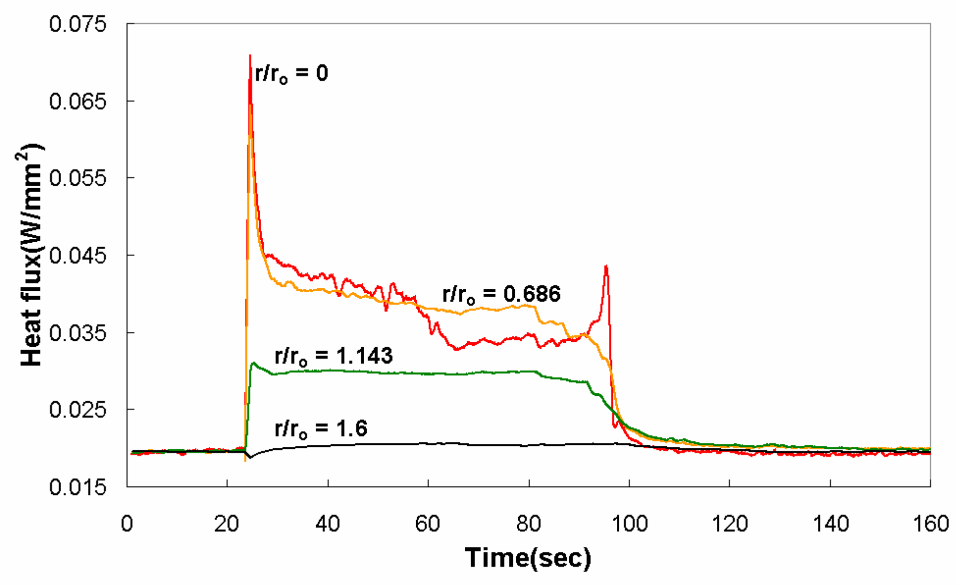

Fig. 4.28 Tomographic temporal temperature variation profile

T_{dry} **=80°C, 10μl**

4.4 Remarks

Constant temperature droplet evaporation experiments were done on the heated microheater. Feedback circuits maintain a constant temperature of the heater surface. Heat flux were measured temporally and spatially.

CHAPTER V

REPEATABILITY AND UNCERTAINTY ANALYSIS

5.1 Repeatability

For repeatability verification, a constant voltage experiment (60°C, 10μl) was picked for data comparison. Other repeated data results are not shown here to avoid redundancy as they exhibit the same tendencies in temperature and heat flux variation. Two independent experiments with the same conditions were compared. The old experiment results are not shown in the previous chapters, while the new experiment results are shown in Chapter III.

Figs. 5.1 to 5.2 show the droplet evaporation of the old and new experiments. As shown, the two droplets have about the same radius (r_o = 1.5mm for old experiment, r_o = 1.55mm for new experiment, 3% in difference) and evaporation time (290.1 sec for old experiment, 292.56 sec for new experiment, 0.8% difference). The unpublished evaporation times could vary up to 1.2% compared with the published results for other temperatures or sizes of the droplet evaporation experiment.

For both old and new droplet evaporations shown in Fig. 5.1 and Fig. 5.2, the droplet maintains the same radius for most of the evaporation time. Evaporation procedures are compared in 6 steps. During these 6 steps, both the old and new droplets maintain almost the same shape.

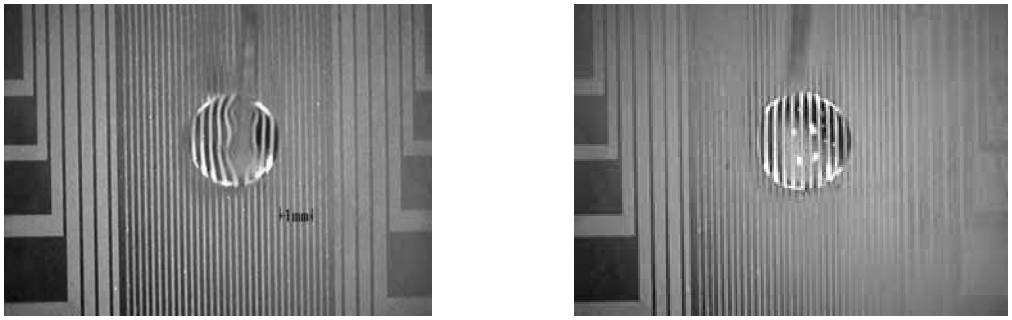

(a) $t/\tau = 0$ (Total evaporation time, $\tau = 290.1$) (b) $t/\tau = 0.207$

(c) $t/\tau = 0.414$ (d) $t/\tau = 0.620$

(c) $t/\tau = 0.965$ (d) $t/\tau = 0.982$

Fig 5.1 Sequential images of slowly evaporating water droplets on the microheater array at T_{dry} = 60°C, 10μl (old experiment)

(a) $t/\tau = 0$ (Total evaporation time, $\tau = 292.56$) (b) $t/\tau = 0.205$

(c) $t/\tau = 0.410$ (d) $t/\tau = 0.615$

(e) $t/\tau = 0.906$ (f) $t/\tau = 0.991$

Fig. 5.2 Sequential images of slowly evaporating water droplets on the microheater array at $T_{\mathrm{dry}} = 60$°C, 10μl (new experiment)

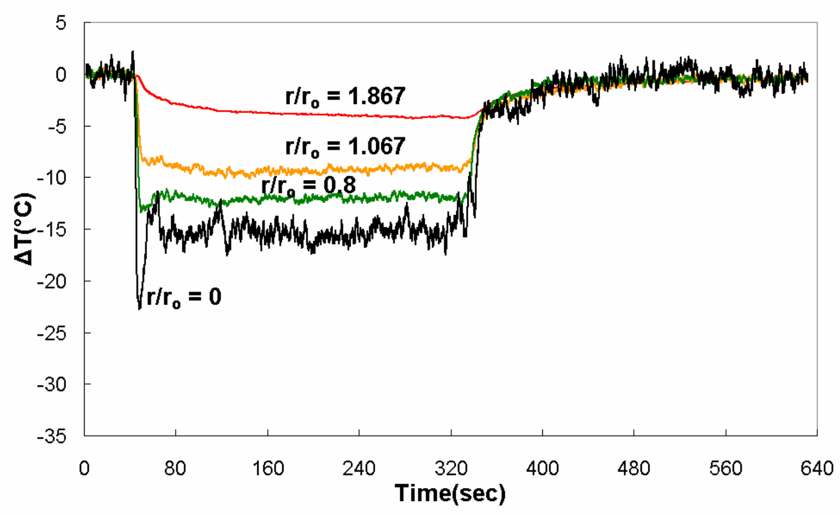

Fig. 5.3 Temperature variation profile of microheater under T_{dry} = 60°C, 10μl, old experiment

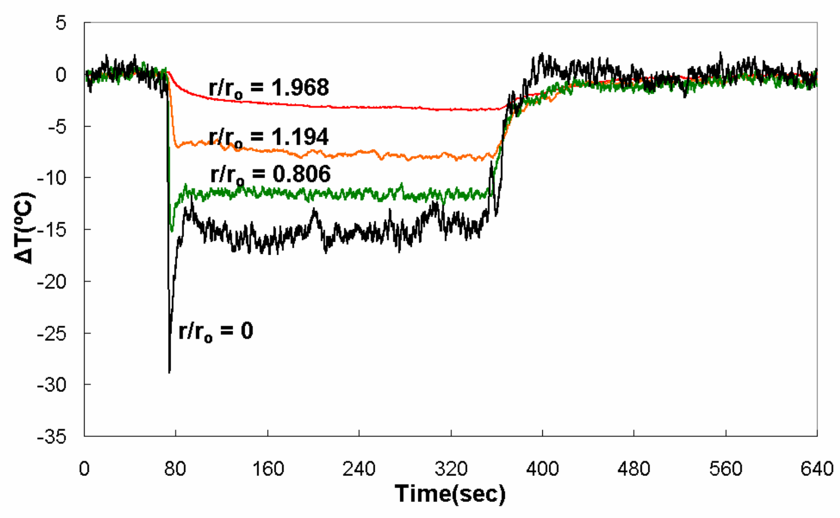

Fig. 5.4 Temperature variation profile of microheater under T_{dry} = 60°C, 10μl, new experiment

Microheater temperature variation by the droplet is compared in Fig. 5.3 and Fig. 5.4. These two graphs show the same temperature variation tendencies. At $r/r_o = 0$, for both cases during most of the evaporation time, they maintain about the same temperature. Also, at $r/r_o \sim 0.8$, for both cases during the most of evaporation time, they maintain about the same temperature.

As shown in Figs. 5.1 to 5.4, all other experimental runs showed the same tendencies when the same dry heater temperature and same amount of water droplet were used. So, for this experiment repeatability is acceptable.

5.2 Uncertainty analysis

Uncertainty always exists for every experiment. For this experiment, the wiring line resistance variation was ignored. In Chapter III, this uncertainty is mentioned and calculated. Uncertainty by ignoring wiring resistance variation is about 0.6%. Uncertainty by linearization of the gold resistance-temperature relation is shown in Table 3.1. The maximum error by linearization is 0.08% at 77°C, which is near the maximum temperature of this experiment. So, in total, this experiment has an uncertainty factor of about 0.68%.

Tomographic deconvolution zones have a fixed radius. The radius of the zones totally depends upon the distances between the heater lines. Droplet sizes do not affect the size of the tomographic deconvolution zones. This means that for any case, the characteristic area ratio of each zone, with respect to the whole heater line area, is fixed. Excluding the outermost area, the characteristic area ratios of the 16 concentric tomographically deconvoluted zones are between 2.7% to 12.74%. The ratio between the above two numbers is 4.7185. Thus, there is no possibility of numerical divergence in temperature or heat flux calculations. The uncertainties in tomographic deconvolution affect the resolution. If we use a finer heater, which allows the use of a higher order tomographic deconvolution, this results in a finer resolved temperature and heat flux distribution. But, as an averaged value, tomographic deconvoluted values are always effective as they have no numerical divergence in calculation or any uncertainties in calculations.

Noises in the voltage signals were averaged to enhance the stability of the data. A 100 point moving average technique was used to reduce this noise. In this technique, data samples 1 through 100 were averaged to obtain the first moving average. The second moving average then comes from data samples 2 through 101. The other moving average data were gathered via the continuation of this procedure.

Uncertainty due to the resistors could be serious. Usually, resistors have 5% or 1% of intrinsic resistance uncertainty. Direct use of these resistors could then result in 1% to 5% temperature errors. This error amount is much larger than the previous two errors combined. In an effort to mitigate these high resistor uncertainties, all resistors were measured using a HP34401A multimeter. For each resistor, three resistance measurements were recorded and then averaged.

CHAPTER VI

CONCLUSION

32 gold microheaters were used for droplet evaporation on the heated surface experiment under a constant voltage mode temperature mode to get the temperature and heat flux distribution. The gold microheater was used as both the heater and temperature sensor. The gold heater line worked well as a temperature sensor with an accuracy of 0.08% at a temperature of 77°C under the constant voltage mode experiment.

For the constant voltage mode experiment, the largest ΔT and heat flux variation occurred upon contact of the droplet with the heater. The ΔT and heat flux remained nearly unchanged during the evaporation due to the latent heat transfer process at a constant temperature. Then temperature and heat flux returned to the dry heater value after completion of evaporation. Heater temperature dropped the most at the center of the droplet and decreased as the distance from the center of the droplet increased. Inside the wetted region ($d/R<1.0$), there existed peaks, both in temperature and heat flux, at the instant of droplet contact, but for the regions outside of the droplet ($d/R>1.0$), there were no peaks in the temperature drop or heat flux. At the final stage of the evaporation, sudden temperature and heat flux drop were observed. The center region of the water droplet suddenly thickened based on droplet contraction, so that the increased local mass enhanced the cooling and momentarily lowered the temperature and heat flux.

For the constant temperature mode experiment, the largest heat flux variation occurred upon contact of the droplet with the heater. The heat flux remained nearly unchanged during the evaporation due to the latent heat transfer process at a constant temperature. Then heat flux returned to the dry heater value after completion of evaporation. Inside of the wetted region (d/R<1.0), there existed peaks in heat flux at the instant of droplet contact, but for the regions outside of the droplet (d/R>1.0), there were no peaks in the heat flux. The wet region maintained almost the same heat flux during most of the evaporation time, regardless of the distance from the center of the droplet, but at the initial evaporation stage, the heat flux peak was larger at the center of the droplet. At the final stage of evaporation, sudden heat flux peaks were observed. As stated in the previous paragraph, the center region of the water droplet is suddenly thickened due to droplet contraction, so that the increased local mass enhances the cooling and momentarily lowers the temperature.

Since the real time signals of voltage drop from each heater wire were directly measured, the resulting resistance and temperature data are very credible. The great benefit of this experimental setup is that it allowed for quantitative monitoring of the heat flux and temperature both inside and outside the water droplet. This is unique, having not been achieved by others.

REFERENCES

[1] Madou, M. J., 2002, *Fundamentals of Microfabrication: The Science of Miniaturization*, 2nd ed., CRC Press, New York, pp. 2-3.

[2] Lee, S., Kim, H., Kuk, K. and Oh, Y., 2002, “A Monolithic Inkjet Print Head: DomeJet,” Sensors and Actuators A: Physical, **95**(2-3), pp. 114-119.

[3] Setti, L., Fraleoni-Morgera, A., Ballarin, B., Filippini, A., Frascaro D. and Piana, C., 2005, “An Amperometric Glucose Biosensor Prototype Fabricated by Thermal Inkjet Printing,” Biosensors and Bioelectronics, **20**(10), pp. 2019-2026.

[4] Chandra, S., di Marzo, M., Qiao, Y. M. and Tartarini, P., 1996, “Effect of Liquid-solid Contact Angle on Droplet Evaporation,” Fire Safety Journal, **27**, pp. 141-158.

[5] Milke, J. A., Tinker, S. C. and di Marzo, M., 1997, “Effect of Dissolved Gases on Spray Evaporative Cooling with Water,” Fire Technology, **33**(2), pp. 99-114.

[6] Pamula, V. K. and Chakrabarty, K., 2003, “Cooling of Integrated Circuits Using Droplet-based Microfluidics,” *Proc. ACM/IEEE Great Lakes Symposium on VLSI*, Washington DC, pp. 84-87.

[7] Bernardin, J. D., Mudawar, I., Walsh, C. B. and Franses, E. I., 1997, "Contact Angle Temperature Dependence for Water Droplets on Practical Aluminum Surfaces," International Journal of Heat and Mass Transfer, **40**(5), pp. 1017-1033.

[8] Tseng, F., Kim, C. and Ho, C., 1998, "A Novel Microinjector with Virtual Chamber Neck," *11th IEEE Workshop on Micro Electro Mechanical Systems Workshop,* Heidelberg, Germany*,* Jan. 25-29, pp. 57-62.

[9] Xiong, T. Y. and Yuen, M. C., 1991, "Evaporation of a Liquid Droplet on a Hot Plate," International Journal of Heat and Mass Transfer, **34**(7), pp. 1881-1894.

[10] Makino, K. and Michiyoshi, I., 1984, "The Behavior of a Water Droplet on Heated Surfaces," International Journal of Heat and Mass Transfer, **27**(5), pp. 781-791.

[11] Crafton, E. F., and Black, W. Z., 2004, "Heat Transfer and Evaporation Rates of Small Liquid Droplets on Heated Horizontal Surfaces," International Journal of Heat and Mass Transfer, **47**, pp. 1187-1200.

[12] Klassen, M., di Marzo M., and Sirkis, J., 1990, "Infrared Thermography of Dropwise Evaporative Cooling," ASME HTD, **141**, pp. 117-121.

[13] di Marzo, M., Tartarini, P., Liao, Y., Evans, D. and H. Baum, 1993, "Evaporative Cooling Due to a Gently Deposited Droplet," International Journal of Heat and Mass Transfer, **36**(17), pp. 4133-4139.

[14] Dawson, H. F. and Di Marzo, M., 1993, "Multi-Droplet Evaporative Cooling: Experimental Result," AIChE Symposium Series. Heat Transfer, **89**(295), pp. 122-131.

[15] Michiyoshi, I. and Makino, K., 1978, "Heat Transfer Characteristics of Evaporation of a Liquid Droplet on Heated Surfaces," International Journal of Heat and Mass Transfer, **21**(5), pp. 605-613.

[16] Tartarini, P., Liao, Y., Kidder, C. and di Marzo, M., 1993, "Transient Cooling of a Hot Surface by Droplets Evaporation. Final Report," *NIST-GCR-93-623,* NIST, Gaithersburg, MD.

[17] Franklin, G. F and Powell, J. D., 1993, Feedback Control of Dynamic System 3rd ed., Prentice Hall, New York, pp. 2-5.

[18] Rule, T. D. and Kim, J., 1999, "Heat Transfer Behavior on Small Horizontal Heaters During Pool Boiling of FC-72," Journal of Heat Transfer, **121**, pp. 386-393.

[19] T. Chen, T. and Chung, J. N., 2002, "Coalescence of Bubbles in Nucleate Boiling on Microheaters," International Journal of Heat and Mass Transfer, **45**, pp. 2329-2341.

[20] Kimura, M. and Toshima, K., 2003, "Thermistor-like pn Junction Temperature-sensor with Variable Sensitivity and It's Combination with a Micro-air-bridge Heater," Sensors and Actuators A, **108**, pp. 239-243.

[21] Chen, T., Klausner, J. F. and Chung, J. N., 2004, “Subcooled Boiling Heat Transfer and Dryout on a Constant Temperature Microheater,” International Journal of Heat Fluid Flow, **25**, pp. 274-287.

[22] Jung, J., Lee, J., Park, H. and Kwak, H., 2003, “Bubble Nucleation on Micro Line Heaters Under Steady or Finite Pulse of Voltage Input,” International Journal of Heat and Mass Transfer, **46**, pp. 3897-3907.

[23] Lee, J., Kim, J. and Kiger, K. T., 2001, “Time and Space Resolved Heat Transfer Characteristics of Single Droplet Cooling Using Microscale Heater Arrays,” International Journal of Heat and Fluid Flow, **22**, pp. 188-200.

[24] Lee, J., Kiger, K. T. and J. Kim, 2002, “Enhancement of Droplet Heat Transfer Using Dissolved Gases,” Paper No. 2002-01-3195, *Proc. SAE Power Systems Conference,* Coral Springs, FL, pp. 736-746.

[25] CRC Handbook of Chemistry and Physics, 84th ed., 2004, Chemical Rubber Pub. Co., Cleveland, OH.

[26] “Electrical Resistivity of Copper, Gold, Palladium and Silver,” 1979, Journal of Physical and Chemical Reference Data, **8**(4), pp. 1147-1298.

[27] Picknett, R. G. and Bexon, R., 1977, “The Evaporation of Sessile or Pendant Drops in Still Air,” Journal of Colloid Interface Science, **77**(2), pp. 336-350.

[28] Meric, R. A. and Erbil, H. Y., 1998, “Evaporation of Sessile Drops on Solid Surfaces: Pseudospherical Cap Geometry,” Langmuir, **14**(7), pp. 1915-1920.

[29] Padday, J. and F. Philos., 1971, “The Profiles of Axially Symmetric Menisci,” Philosophical Transactions of the Royal Society of London. Series A, Mathematical and Physical Sciences, **269**(1197), pp. 265-293.

[30] Erbil, H. Y. and Meric, R. A., 1997, “Evaporation of Sessile Drops on Polymer Surfaces: Ellipsoidal Cap Geometry,” Journal of Physical Chemistry B, **101**(35), pp. 6867-6873.

[31] Bourges, C. and Shanahan, M. E. R., 1995, “Influence of Evaporation on Contact Angle,” Langmuir, **11**, pp. 2820-2829.

[32] Shanahan, M. E. R. and Bourges, C., 1994, “Effects of Evaporation on Contact Angles on Polymer Surfaces,” International Journal of Adhesion and Adhesive, **14**(3), pp. 201-205.

[33] Birdi, K. S., Vu, D. T. and Winter, A. J., 1989, “A Study of the Evaporation Rates of Small Water Drops Placed on a Solid Surfaces,” Journal of Physical Chemistry, **93**, pp. 3702-3703.

[34] Birdi, K. S. and Vu D. T., 1993, “Wettability and the Evaporation Rates of Fluids from Solid Surfaces,” Journal of Adhesion Science and Technology, **7**, pp. 485-493.

[35] Deans, A. R., 1983, *The Radon Transformation and Some of Its Applications*, Wiley: New York.

[36] Kak, A. C. and Slaney, M., 1987, *Principles of Computerized Tomographic Imaging*, IEEE Press, New York, pp. 275-296.

[37] Kihm, K. D., Okamoto, K., and Ko, H. S., 2004, "Robust Algorithms for Tomographic Reconstruction of Line-of-Sight Thermal Flow Field Images," pp. 143-202, Advances in Heat Transfer, **38**, Elsevier-Academic Press, New York.

[38] Bruun, H. H., 1995, *Hot-wire Anemometry*, Oxford University Press: London, pp. 19-70.

[39] Goldstein, R. J., 1983, *Fluid Mechanics Measurements*, Hemisphere Publishing Co.: Washington DC, pp. 99-144.

[40] Lee, S. and Kauh, S. K., 1996, "A New Approach to Enhance the Sensitivity of a Hot-Wire Anemometer and Static Response Analysis of a Variable Temperature Anemometer," Experiments in Fluids, **22**, pp. 212-219.

VITA

SOKWON PAIK

Mechanical Engineering Department

Texas A&M University

College Station, Texas 77843-3123

Phone: (979) 695-0928

E-mail: sokwonnp@yahoo.com

Personal Data

Date of Birth: June 24, 1969
Parents: Tongki Paik, Minja Kim
Permanent Address: 560-020 Kyongwon dong 1-59, Wansan-Gu,
Jeonju Jeonbuk, Korea

Education

Ph.D.,	Mechanical Engineering, Texas A&M University, May, 2005
M.S.,	Astronomy, Yonsei University, Feb. 1996
B.S.,	Astronomy, Yonsei University, Feb. 1994

Professional Experiences

05/98-05/01	Research Assistant in the Department of Aerospace Engineering, Texas A&M University, College Station, Texas
09/03-05/04	Research Assistant in the Department of Mechanical Engineering, Texas A&M University, College Station, Texas